Title	Detection of magnetic fluctuations in chiral helimagnet CrNb3S6 thin films via pure spin current
Author(s)	鈴木, 将太
Citation	大阪大学, 2022, 博士論文
Version Type	VoR
URL	https://doi.org/10.18910/87818
rights	
Note	

Detection of magnetic fluctuations in chiral helimagnet $CrNb_3S_6$ thin films via pure spin current

Shota Suzuki

January 7, 2022

Contents

Preface

Electrons have two degrees of freedom, i.e., charge and spin. Electronics is a research field which deal with control of charge current. It had made a significant contribution to the development of industry and science in the 20th century. In the 21st century, a research field known as "spintronics" has been growing rapidly. In spintronics, the spin as well as the charge have been actively utilized. One of the most important concepts in spintronics is "pure spin current" that is the flow of spin angular momentum without charge flow. Thus, devices based on the pure spin current are expected to contribute to energy efficient. Unlike the charge current, the pure spin current is not a conserved physical quantity but a diffusive flow with a characteristic length of several tens of nanometers. Conversely speaking, the pure spin current is expected to be utilized as a new probe to detect magnetic properties in nanometer-scale (nanoscale) devices.

The spin Hall effect (SHE) and its inverse effect (inverse spin Hall effect, ISHE) enable us to interconvert the charge current and the pure spin current [1–4]. It has been known that the ISHEs in magnetic materials are modulated near the magnetic transition temperatures where spin fluctuations are strong. The result indicates that there is a strong correlation between spin fluctuations of the magnetic moment and the pure spin current. Based on this correlation, the pure spin current can be a sensitive probe to investigate spin dynamics in magnetic systems [5–8]. As mentioned above, the pure spin current decays within several tens of nanometers. In order to implement the pure spin current probe, magnetic systems have to be fabricated into sub-micrometer size.

In recent years, chiral magnetic systems have attracted much attention due to their unique magnetic ordering states. In the chiral helimagnet, the magnetic moments are arranged in a helical form due to the competition between the exchange interaction and the Dzyaloshinskii-Moriya (DM) interaction [9, 10]. When a magnetic field is applied perpendicular to the helical axis, the period of the magnetic spiral increases and becomes infinite at the critical field where the helimagnet is forced to a ferromagnet. This peculiar magnetic state is called the chiral soliton lattice (CSL) and has been investigated in detail since the 1950s, using neutron scattering [11], X-rays diffraction [12], Lorentz transmission electron microscope (LTEM) [13]. However, some fundamental issues, such as spin state at the end of the CSL at the surface (fixed end or free end), remain unsolved.

In this thesis, we have aimed to study magnetic dynamics in a chiral helimagnet with pure spin current. For this purpose, we have chosen $CrNb_3S_6$ that is a typical chiral helimagnet. $CrNb_3S_6$ is a layered chiral helimagnet, which enables us to obtain a thin film with the mechanical exfoliation technique and also to incorporate it into the spin Hall device to inject the pure spin current. Contrary to graphite and transition metal dichalcogenides, we cannot adopt the standard exfoliation for $CrNb_3S_6$ because of a stronger van der Waals interaction via Cr atoms. We first aimed to establish the nanofabrication process to extract a thin film from the bulk single crystal. We then performed spin transport measurements in $CrNb_3S_6$ thin films in order to reveal the relation between the magnetic ordering state in $CrNb_3S_6$ and the pure spin current.

Chapter 1

Physics of chiral magnetic systems

1.1 Helimagnets

Helimagnets are magnetic states where neighboring magnetic moments arrange in a spiral or helical pattern with a characteristic tilt angle between 0 and 180 degrees. In 1959, Yoshimori [14] first suggested that MnO_2 has the helimagnetic structure. At almost the same time, Kaplan [15] and Villain [16] also reported the helical magnetic structure in Mn compounds. Since then, the helimagnetism has been actively studied. The microscopic mechanism of the helimagnetism is classified into two types. One is called Yoshimori-type or symmetric helimagnet where the energies of right-handed and left-handed spirals are degenerate. The other is called Dzyaloshinskii-type or antisymmetric helimagnet where the chirality of spiral magnetic structure (i.e., dextrality or sinistrality) is generated as a result of the antisymmetric exchange interaction, so-called the Dzyaloshinskii-Moriya (DM) interaction. This type was first predicted by Dzyaloshinskii in 1964 [17]. In Dzyaloshinskii-type helimagnets, the period of the magnetic spiral increases with increasing the applied magnetic field perpendicular to the helical axis, while the spiral magnetic structure is preserved. This peculiar magnetic state is called the chiral soliton lattice (CSL). The CSL is stable because of the robustness of the chirality that is protected by the crystal structure. The period of the CSL can be controlled by applying the magnetic field from several tens nanometers to infinity. When the period becomes infinite at a critical field, the helimagnet is forced to a ferromagnet. The CSL has been attracting much attention in the field of spintronics as a new candidate for controlling the spin phase, similar to the skyrmions [18, 19]. In spite of several experimental and theoretical works on the CSL in recent years [20], all the detailed properties of the CSL have not been elucidated yet.

1.2 Concept of chirality

Chirality is a physical property that an object cannot be superimposed onto its mirror image [21]. In early 19th century, Arago and Biot discovered the optical rotation of the linearly polarized light in quartz. It was the first time that the concept of the chirality was brought into scientific research. In 1848, Pasteur successfully separated the sodium ammonium tartrate crystal into two types of structures, and showed that the direction of optical rotation was determined by the crystal structure, i.e., right- or left-handedness. These studies led to the discovery of chiral molecules and crystals at the atomic length scale.

The word "chirality" was first introduced by Lord Kelvin in 1904 and defined as described in the above paragraph [22]. Based on this definition, the appearance of chirality is accompanied by the broken space inversion (parity $\mathcal{P}$). In 1986, Barron redefined the concept of the chirality in order to include dynamical phenomena [23] and classified the chirality into two types: "true chirality" and "false chirality". The former is valid when $\mathcal{P}$ is broken but the combination of rotation $\mathcal{R}$ and time inversion $\mathcal{T}$, i.e., $\mathcal{RT}$, is not broken, while the latter means that $\mathcal{P}$ and $\mathcal{T}$ are separately broken and $\mathcal{PT}$ is invariant. For example, the true chirality is a typhoon and the false chirality is the Faraday effect. Thus, both systems have completely different physical properties.

1.3 Symmetric and antisymmetric helimagnets

As mentioned in Sec. 1.1, there are two types of helimagnetic structures: one is the symmetric helimagnet called Yoshimori-type, and the other is the antisymmetric helimagnet called Dzyaloshinskii-type. They exhibit similar spin structures at first glance, but have different properties from the viewpoint of chiral symmetry. In particular, a clear difference appears when the external magnetic field is applied perpendicular to the helical axes of both helimagnets. As for Yoshimori-type, the helimagnetic structure changes into a fan-structure with a discontinuous transition, and finally becomes a forced ferromagnet, as shown in Fig. 1.1. On the other hand, the magnetic structure of Dzyaloshinskii-type shows a peculiar magnetic state called the chiral soliton lattice (CSL) before it becomes ferromagnetic (Fig. 1.2).

In the following, we introduce the theoretical background of Yoshimori-type and

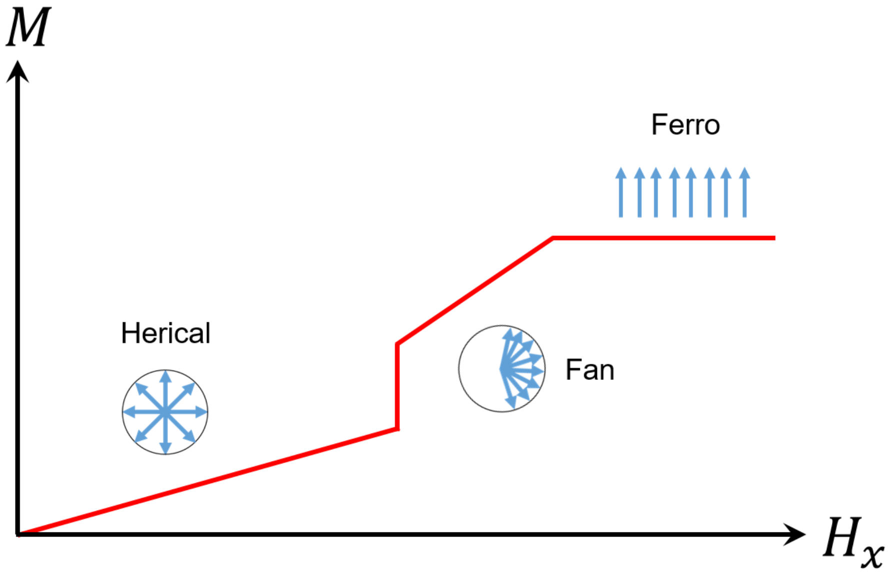

Figure 1.1: Schematic image of $M - H$ curve expected for Yoshimori-type helimagnet. The magnetic field is applied perpendicular to the helical axis.

Dzyaloshinskii-type helimagnets. Figure 1.3 depicts a spin model for Yoshimori-type helimagnet. Spins that can move in the x-y plane are arranged along the z-axis and the magnetic field is applied along the x-axis. We assume a ferromagnetic exchange interaction $J_1 > 0$ for the nearest neighbor spins and an antiferromagnetic exchange interaction $J_2 < 0$ for the next nearest neighbor spins. The Hamiltonian of this system is written as

$$\mathcal{H} = -J_1 \sum_i \boldsymbol{S}_i \cdot \boldsymbol{S}_{i+1} - J_2 \sum_i \boldsymbol{S}_i \cdot \boldsymbol{S}_{i+2}, \tag{1.1}$$

where $\boldsymbol{S}_i$ indicates a spin vector at the i-th site. For simplicity, we consider only three classical spins with the same magnitude of spin angular momentum, i.e., $S = S_1 = S_2 = S_3$. We also define the angle between the x-axis and the direction of spin at the i-th site as θ_i. Equation (1.1) can be rewritten as

$$\mathcal{H} = -2J_1 S^2\{\cos(\theta_2 - \theta_1) + \cos(\theta_3 - \theta_2)\} - 2J_2 S^2 \cos(\theta_3 - \theta_1). \tag{1.2}$$

By putting $\theta = \theta_3 - \theta_2 = \theta_2 - \theta_1$, Eq. (1.2) can be simplified as

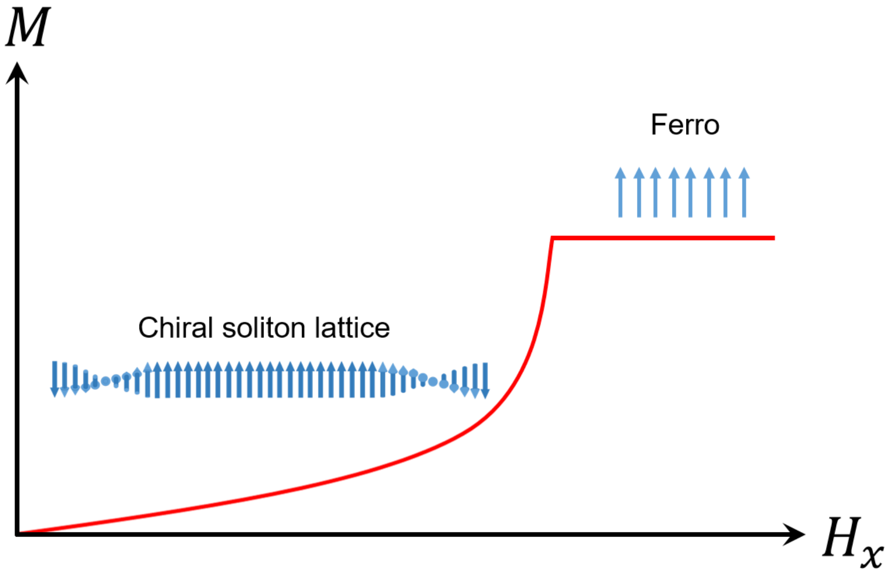

Figure 1.2: Schematic image of $M-H$ curve measured expected for Dzyaloshinskii-type helimagnet. The magnetic field is applied perpendicular to the helical axis.

$$\mathcal{H} = -4J_1S^2\cos\theta - 2J_2S^2\cos 2\theta. \tag{1.3}$$

By differentiating Eq. (1.3) by θ, local minima can be obtained as follows:

$$\frac{d\mathcal{H}}{d\theta} = 4J_1S^2\sin\theta + 4J_2S^2\sin 2\theta = 0, \tag{1.4}$$

$$\theta = 0,\ \pi,\ \pm\cos^{-1}\left(-\frac{J_1}{2J_2}\right). \tag{1.5}$$

Equation (1.5) indicates that this system can be ferromagnetic, antiferromagnetic, and helimagnetic when $\theta = 0$, π, and $\pm\cos^{-1}\left(-\frac{J_1}{2J_2}\right)$, respectively. In the helimagnetic case, θ can take both the positive $\left(+\cos^{-1}\left(-\frac{J_1}{2J_2}\right)\right)$ and negative $\left(-\cos^{-1}\left(-\frac{J_1}{2J_2}\right)\right)$ values. This fact indicates that the two states with positive and negative θ, i.e., right-handed and left-handed helimagnets are degenerate.

On the other hand, the antisymmetric helimagnetic structure originates from the Dzyaloshinskii-Moriya interaction. Dzyaloshinskii predicted the existence of the antisymmetric exchange interaction from the consideration of symmetry in 1958 [9,

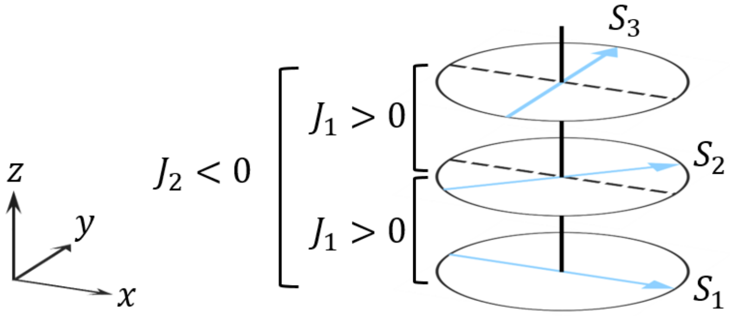

Figure 1.3: Schematic image of the spin model of Yoshimori-type helimagnetic structure.

10]. In 1960, Moriya showed that the antisymmetric exchange interaction is derived from the second-order perturbation mediated by the excited state due to the spin-orbit interaction [24,25]. Based on these theoretical backgrounds, the antisymmetric exchange interaction is called the Dzyaloshinskii-Moriya interaction (DMI). The DMI between two spins at the i-th and j-th sites is written as $\boldsymbol{D}_{ij} \cdot \boldsymbol{S}_i \times \boldsymbol{S}_j$, where $\boldsymbol{D}_{ij}$ is the constant vector called the DM vector. The sign of $\boldsymbol{D}_{ij}$ determines the tilting orientation of one spin relative to the other. The quantity $\boldsymbol{\chi}_{ij} = \boldsymbol{S}_i \times \boldsymbol{S}_j$ is called the spin chirality that breaks $\mathcal{P}$ but preserves $\mathcal{RT}$. That is to say, $\boldsymbol{\chi}_{ij}$ is a true chirality.

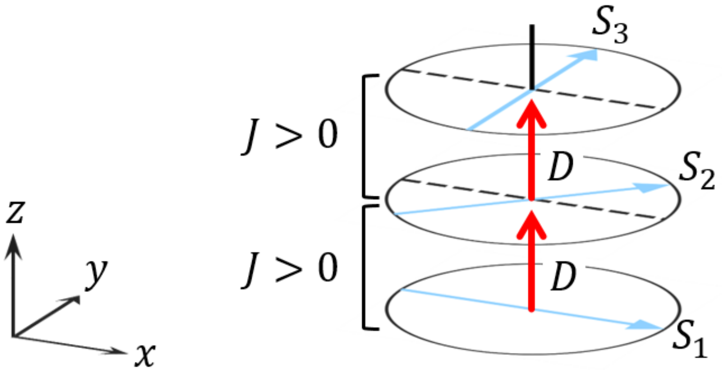

Figure 1.4: Schematic image of the spin model of Dzyaoshinskii-type helimagnetic structure.

When $\boldsymbol{D}_{ij}$ is parallel to a fixed axis throughout the crystal, it is expressed as $\boldsymbol{D}_{ij} = \boldsymbol{D} = D\hat{\boldsymbol{e}}$. Here, D is a constant and $\hat{\boldsymbol{e}}$ is a unit vector along the crystallographic axis. The competition between the DMI and the isotropic ferromagnetic coupling $J > 0$ gives rise to a helical structure. The orientation of $\boldsymbol{D}$ reflects the crystal structure and determines the direction whether the magnetic moments are rotated to right- or left-handed direction along the helical axis.

As shown in Fig. 1.4, in order to model the Dzyaloshinskii-type structure, we assume that (1) spins that can move in the x-y plane are arranged along the z-axis, (2) the exchange interaction J and the DM vector $\boldsymbol{D}$ work between the nearest neighbor spins, and (3) $\boldsymbol{D}$ is parallel to the z-axis, i.e., $\boldsymbol{D} = D\hat{\boldsymbol{e}}_z$. The Hamiltonian of the Dzyaloshinskii-type structure is written as follows:

$$\mathcal{H} = -J\sum_i \boldsymbol{S}_i \cdot \boldsymbol{S}_{i+1} - \boldsymbol{D} \cdot \sum_i \boldsymbol{S}_i \times \boldsymbol{S}_{i+1}. \tag{1.6}$$

As we have done for the Yoshimori-type structure, we consider only three classical spins with the same magnitude of spin angular momentum, i.e., $S = S_1 = S_2 = S_3$. Furthermore, we also define the angle between the x-axis and the direction of spin at the i-th site as θ_i. Equation (1.6) can be rewritten as:

$$\mathcal{H} = -JS^2\left\{\cos(\theta_2 - \theta_1) + \cos(\theta_3 - \theta_2)\right\} - DS^2\left\{\sin(\theta_2 - \theta_1) + \sin(\theta_3 - \theta_2)\right\}. \tag{1.7}$$

By putting $\theta = \theta_3 - \theta_2 = \theta_2 - \theta_1$ and following the same calculation procedure as in the Yoshimori-type, we obtain

$$\theta = \tan^{-1}\left(\frac{D}{J}\right). \tag{1.8}$$

Unlike the case of the Yoshimori-type structure, only a positive or negative θ is allowed in the Dzyaloshinskii-type structure. This feature results in the chirality (right- or left-handedness) in the crystal.

1.4 Chiral soliton lattice

In a Dzyaloshinskii-type helimagnet, the period of the magnetic spiral increases and becomes infinite at a critical field where the helimagnet is forced to a ferromagnet under the magnetic field perpendicular to the helical axis (i.e., x-axis) as shown in Fig. 1.5. This peculiar magnetic state is called the chiral soliton lattice (CSL) [26]. The Hamiltonian of the system can be expressed as:

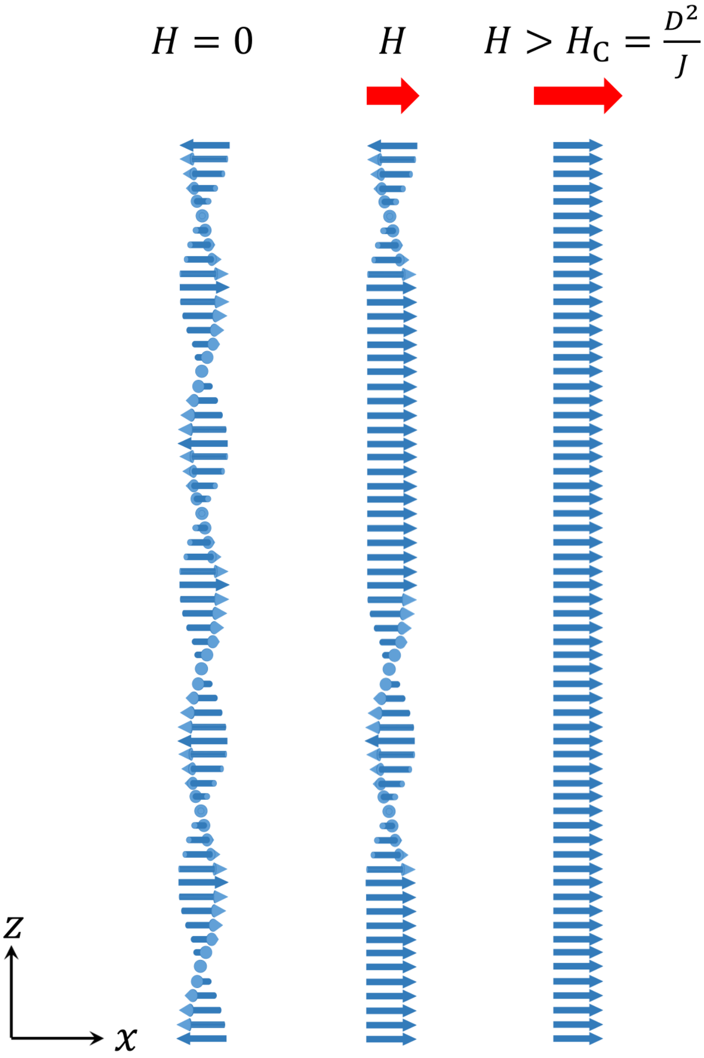

Figure 1.5: Schematic image of the CSL.

$$\mathcal{H} = -J\sum_i \boldsymbol{S}_i \cdot \boldsymbol{S}_{i+1} - \boldsymbol{D}\cdot\sum_i \boldsymbol{S}_i \times \boldsymbol{S}_{i+1} - \boldsymbol{H}\cdot\sum_i \boldsymbol{S}_i, \tag{1.9}$$

where $\boldsymbol{H} = H\hat{\boldsymbol{e}}_x$ is the applied magnetic field perpendicular to the helical axis. As discussed in the previous section, we consider classical spins with the same magnitude of spin angular momentum, i.e., $S = S_i$, and define the relative angle between $\boldsymbol{S}_i$ and the x-axis as θ_i. In this case, Eq. (1.9) can be rewritten as:

$$\mathcal{H} = -JS^2\sum_i \cos(\theta_{i+1} - \theta_i) - DS^2\sum_i \sin(\theta_{i+1}-\theta_i) - HS\sum_i \cos\theta_i. \tag{1.10}$$

When the the period of the magnetic spiral at the zero magnetic field, $L(0)$, is much longer than the lattice constant a_0 ($L_0/a_0 \sim 40$ for CrNb$_3$S$_6$), we can take the continuum limit: $\sum_j \to {a_0}^{-1}\int_0^L dz$, $\theta_i \to \theta(z)$, and $\theta_{i+1} \to \theta(z+a_0) \approx \theta(z) + a_0\dfrac{d\theta}{dz} + \cdots$. Thus, the first and second terms in Eq. (1.10) can be rewritten as

$$\cos(\theta_{i+1}-\theta_i) \to \cos(\theta(z+a_0)-\theta(z)) \approx \cos\left(a_0\frac{d\theta}{dz}\right) \approx 1 - \frac{{a_0}^2}{2}\left(\frac{d\theta}{dz}\right)^2, \tag{1.11}$$

$$\sin(\theta_{i+1}-\theta_i) \to \sin(\theta(z+a_0)-\theta(z)) \approx \sin\left(a_0\frac{d\theta}{dz}\right) \approx a_0\frac{d\theta}{dz}. \tag{1.12}$$

Therefore, Eq. (1.10) is transformed into $\mathcal{H} = {a_0}^{-1}\int_0^L \tilde{\mathcal{H}}dz$, where the Hamiltonian per unit length $\tilde{\mathcal{H}}$ is described as

$$\tilde{\mathcal{H}} = \frac{JS^2{a_0}^2}{2}\left(\frac{d\theta}{dz}\right)^2 - DS^2a_0\frac{d\theta}{dz} - SH\cos\theta, \tag{1.13}$$

$$= JS^2{a_0}^2\left[\frac{1}{2}\left(\frac{d\theta}{dz}\right)^2 - q_0\frac{d\theta}{dz} - m^2\mathrm{cos}\theta\right], \tag{1.14}$$

where q_0 is the wave number of the zero-field helimagnetic structure defined by

$$q_0 \equiv \frac{D}{Ja_0}, \tag{1.15}$$

and m is the coefficient of nonlinear term defined as

$$m^2 \equiv \frac{H}{JS{a_0}^2}. \tag{1.16}$$

Equation (1.14) is called the chiral sine-Gordon Hamiltonian. By using the Jacobi elliptic function, θ is expressed as

$$\theta(z) = 2\mathrm{am}\left(z\frac{m}{\kappa}\right), \tag{1.17}$$

where am is the Jacobi's amplitude function with the elliptic modulus $\dfrac{m}{\kappa} = \dfrac{\pi q_0}{4E}$ $(0 \leq \kappa < 1)$. From these equations, the magnetic field dependence of the phase distribution is obtained. The spatial period of the soliton is given by using the elliptic function,

$$L(H) = 2\frac{\kappa K}{m} = \frac{8KE}{\pi q_0}, \tag{1.18}$$

where $K = K(\kappa)$ and $E = E(\kappa)$ are the complete elliptic integrals of the first kind and the second kind, respectively. For the zero magnetic field, the period is given by

$$L(0) = \frac{2\pi}{q_0}. \tag{1.19}$$

The soliton density

$$\frac{L(0)}{L(H)} = \frac{\pi^2}{4KE} \tag{1.20}$$

works as an order parameter. Increasing H from zero to critical field H_C corresponds to increasing κ from zero to 1. Therefore, the critical field

$$H_C = \left(\frac{\pi q_0 a_0}{4}\right)^2 JS = \left(\frac{\pi}{4}\frac{D}{J}\right)^2 JS \sim \frac{D^2}{J} \tag{1.21}$$

is obtained.

The direct observation of the CSL was first realized by Togawa *et al.* by using the Lorentz transmission electron micrscopy (TEM) in 2012 [13]. Figures 1.6(a), (b), and (c) show the Lorentz TEM images of the Dzyaloshinskii-type helimagnet, $\mathrm{CrNb_3S_6}$ at 110 K under the magnetic fields of 0, 0.208, and 0.224 T, respectively. The helical structures are observed as stripe patterns. The interval between each stripe, i.e., the period of the helical structure, increases with increasing magnetic field. The magnetic field dependence of the interval between the stripes is shown in Figs. 1.6(e) and (f). The interval between the stripes can be well reproduced by the elliptic function as discussed above. From this experiment, the existence of the CSL has been experimentally proved for the first time.

Kishine *et al.* predicted that the magnetization of the CSL takes discrete values as a function of the magnetic field perpendicular to the helical axis because of finite solitons [27]. In this calculation, they postulated the fixed ends of CSL for both sides. Figure 1.7 shows the calculated magnetic field dependence of energy and magnetization with a finite number ($n = 6 \sim 10$) of solitons. With increasing magnetic field, the system energy with n becomes higher than that with $n - 1$, resulting in a reduction of the number of solitions in the system. The crossover from n to $n - 1$ is accompanied by the magnetization jump at the same magnetic field.

Togawa *et al.* demonstrated that magnetoresistance of $\mathrm{CrNb_3S_6}$ showed discrete behavior [28]. They fabricated a micro-meter scale single crystal sample ($\sim 10 \times 10 \times 1\ \mu\mathrm{m}^3$) by using a focused ion-beam technique and applied an electric current along the helical axis ($c-$axis of the crystal) as shown in Fig. 1.8(a). Many steps in the magnetoresistance are observed [see Figs. 1.8(b), (c) and (d)].

The CSL has been actively studied both theoretically and experimentally. However, some fundamental issues, such as spin state at the end of CSL at the surface (fixed end or free end), remain unsolved.

1.5 Basic properties of $\mathrm{CrNb_3S_6}$

$\mathrm{CrNb_3S_6}$ is a typical chiral helimagnet where the DMI plays an important role on the magnetism. Figure 1.9 shows the crystal structure of $\mathrm{CrNb_3S_6}$. Cr atoms are intercalated into the two S layers of $\mathrm{NbS_2}$ which is one of the transition metal dichalcogenides. $\mathrm{CrNb_3S_6}$ belongs to a space group $P6_322$ that does not have the central symmetry. The lattice constants are $a = 5.74$ Å, and $c = 12.10$ Å [30]. The Cr ion is trivalent and has a spin of $S = 3/2$. Magnetization and neutron scattering measurements were performed by Miyadai *et al* [11]. From their experimental results, it was found that the critical temperature is $T_\mathrm{C} = 130$ K and one spiral pitch under the zero magnetic field is $L(0) = 48$ nm.

Because $\mathrm{CrNb_3S_6}$ has a layered crystal structure, it is expected that the crystal can be mechanically exfoliated. Actually, as shown in Fig. 1.10, a clear cleavage plane appears on the surface of the crystal. However, the interaction between the two S layers becomes stronger than standard van der Waals materials because of the

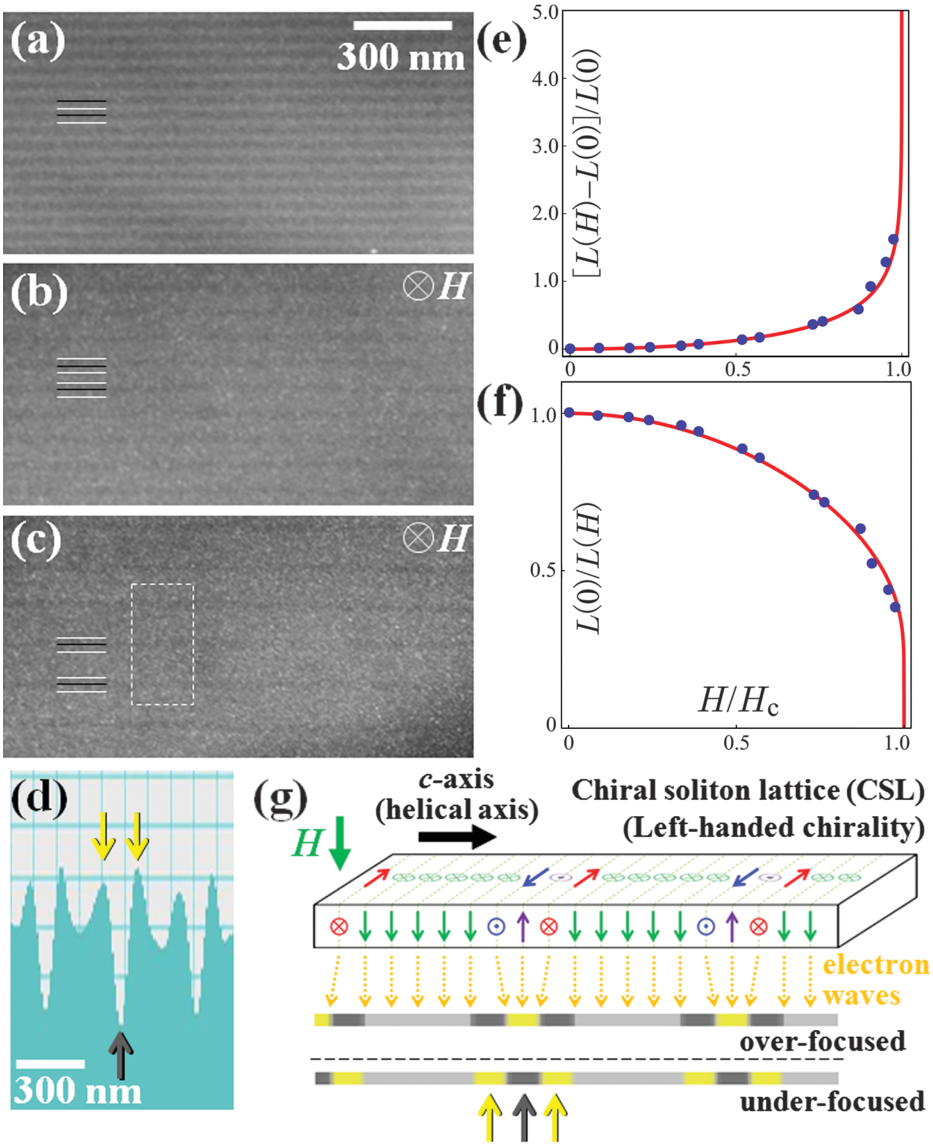

Figure 1.6: (a), (b), (c) Lorentz TEM images of $CrNb_3S_6$ at 110 K under the magnetic field of 0, 0.208, and 0.224 T, respectively [13]. (d) Line profile of the contrast intensity integrated in the dotted square in (c). The periodic pattern is partitioned by three contrast lines, namely, central dark contrast line (black arrow) accompanied with two adjacent bright contrast lines (yellow arrows). (e), (f) $[L(H) - L(0)]/L(0)$ and $L(0)/L(H)$ as a function of the reduced field (H/H_C). (g) Illustration of the relation between the detailed magnetic structure of CSL and the intensity of the Lorentz TEM image.

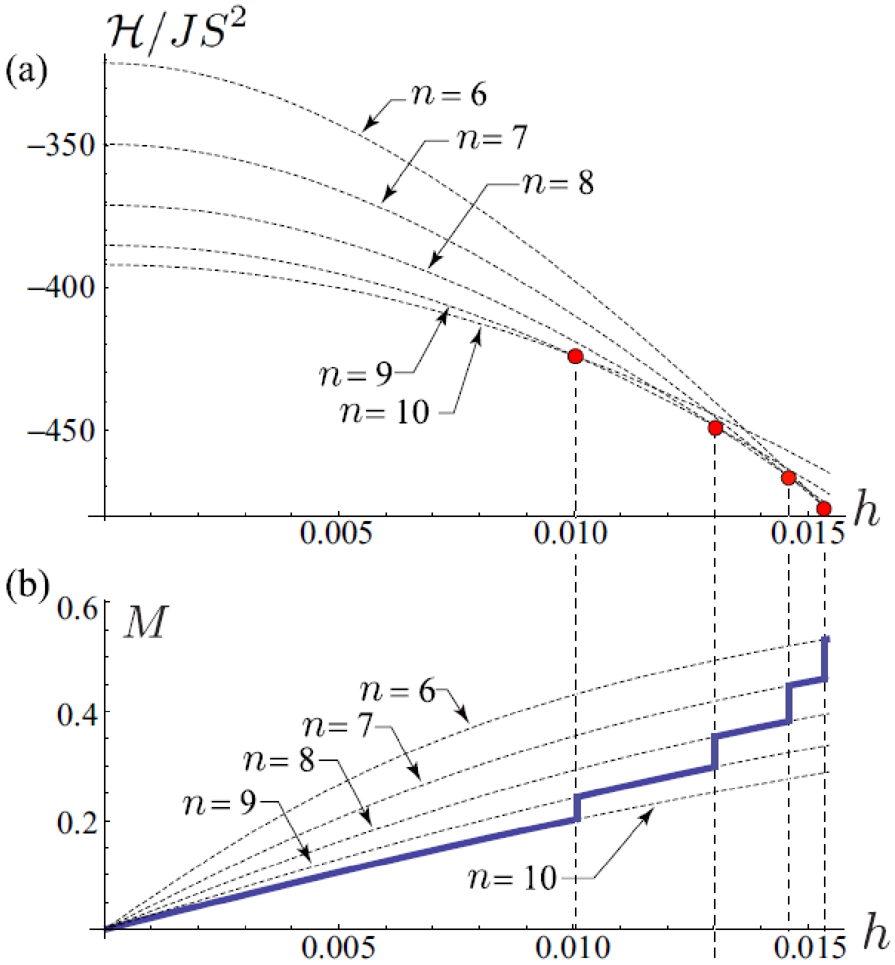

Figure 1.7: (a) Energy as function of the magnetic field [27]. n indicates the number of solitons. The red points show the crossover fields from n to $n-1$. (b) Magnetization curve (blue line) in the CSL with increasing the magnetic field.

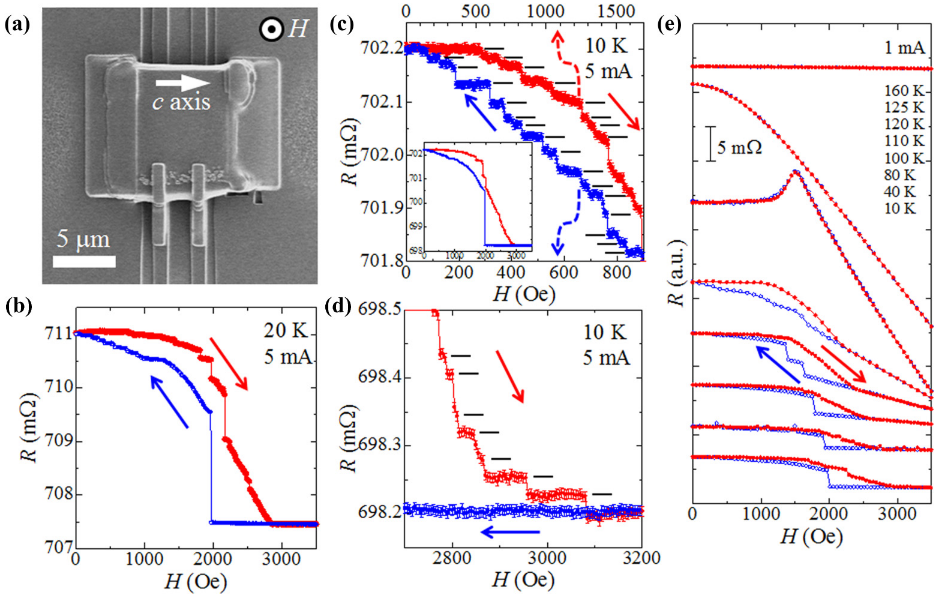

Figure 1.8: (a) Scanning Ion Microscope image of a micrometer-size device of $CrNb_3S_6$ [28]. (b) Magnetoresistance of the $CrNb_3S_6$ device at 20 K. The red and blue curves are obtained when the magnetic field is swept from 0 to 3500 Oe and vice versa, respectively. (c), (d) Magnetoresisatances at 10 K in the low-field and high-field regions, respectively. The red and blue curves are the same meanings as in (b). (e) Magnetoresistances measured at several temperatures.

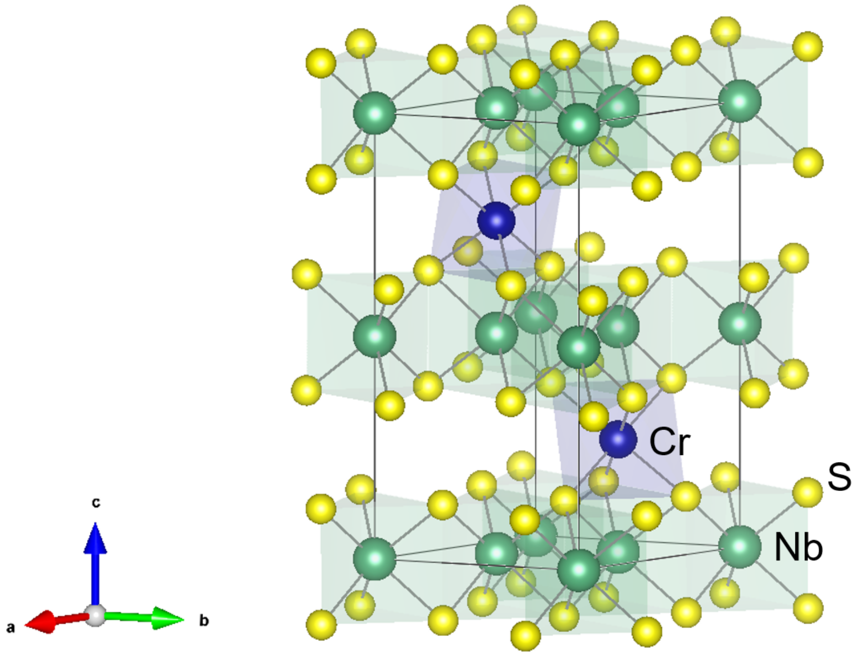

Figure 1.9: The crystal structure of $CrNb_3S_6$. This figure was drawn by using the software VESTA [29].

intercalated Cr atoms. Therefore, atomically thin layers cannot be easily obtained by using the standard exfoliation technique, so-called the scotch tape technique used for graphene or transition metal dichalcogenides.

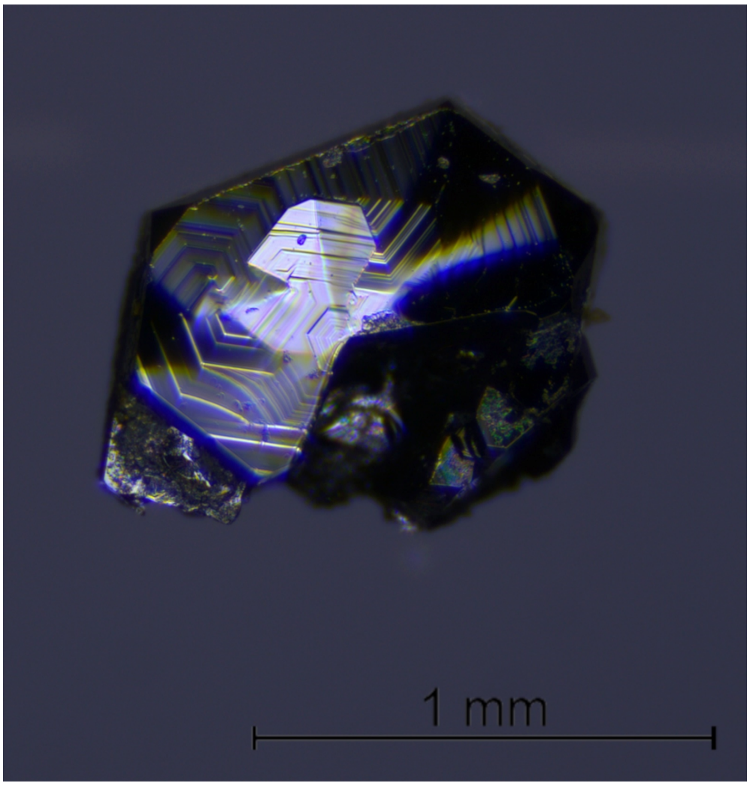

Figure 1.10: Optical microscope image of bulk $CrNb_3S_6$ single crystal.

In 2018, Wang *et al.* performed magnetoresistance measurements of thin-film $CrNb_3S_6$ devices [31]. They fabricated $CrNb_3S_6$ thin film devices with thicknesses from 28 nm to 280 nm by using the scotch tape technique, as shown in Fig. 1.11. Since one spiral pitch at zero magnetic field is 48 nm, the total number of spirals in the $CrNb_3S_6$ thin film can be estimated by measuring the thickness. Figures 1.12(a)-(d) show typical magnetoresitance curves of $CrNb_3S_6$ with four different thicknesses. The number of step in the magnetoresistance corresponds to the number of the helical magnetic structure estimated from the film thicknesses. They also measured the magnetoresistance with a thickness less than 48 nm ($= L(0)$), and confirmed that there is no step in the magnetoresistance.

Although they showed that the scotch tape technique is useful for $CrNb_3S_6$, the fabrication conditions depend on the adhesive strength of the tape and the experimental environment. Therefore, one has to establish the optimum way in each laboratory.

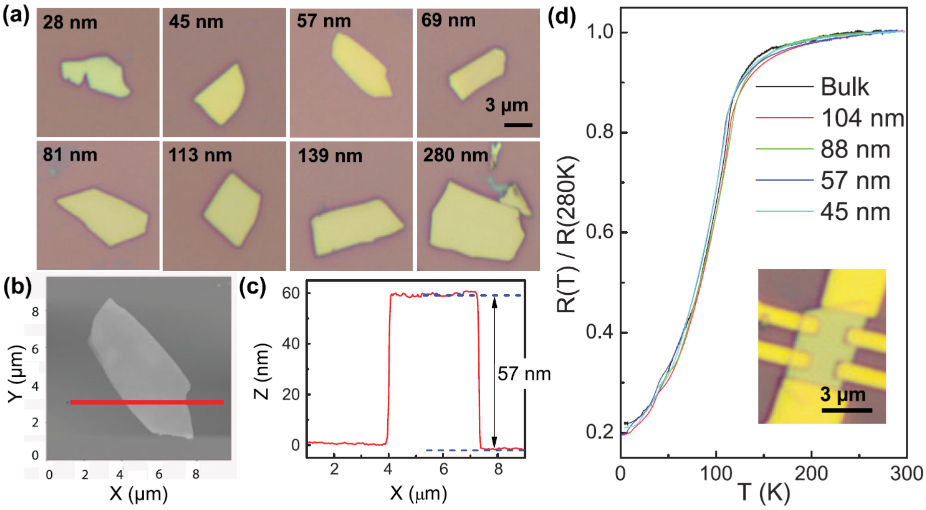

Figure 1.11: (a) Optical microscope images of exfoliated $CrNb_3S_6$ crystals with thicknesses from 28 nm to 280 nm [31]. (b) Atomic force microscope image of the 57 nm thick film. (c) The cross section of the 57 nm thick film shown in (b). (d) Temperature dependence of resistance normalized at $T = 280$ K $[R(T)/R(280\text{ K})]$ for different thicknesses.

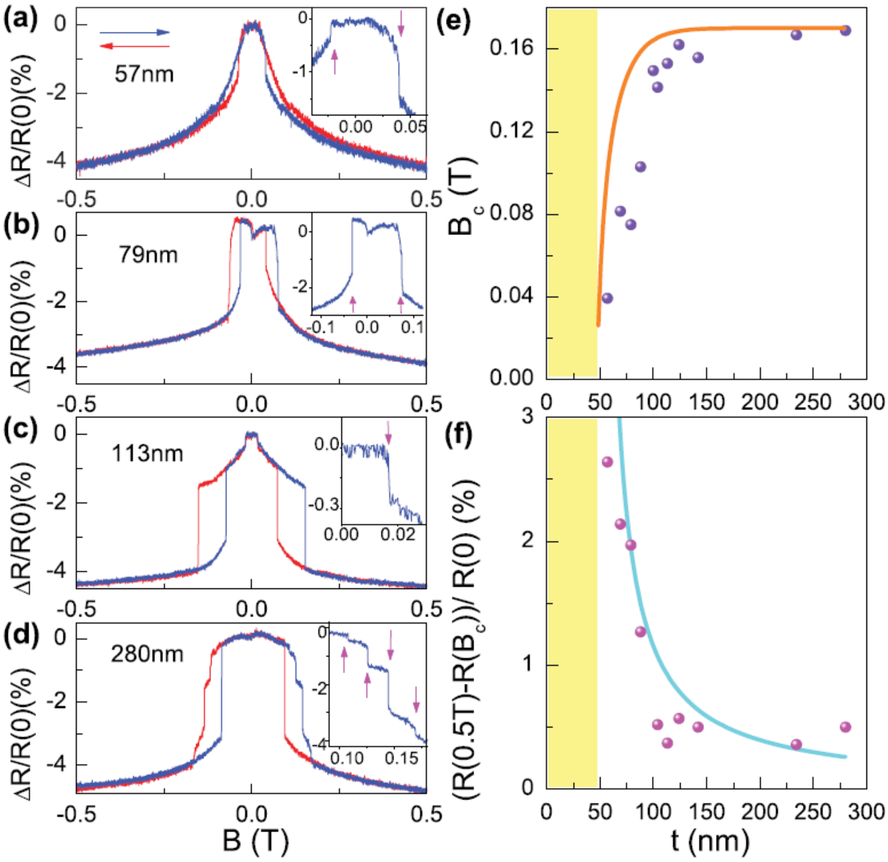

Figure 1.12: (a)-(d) Magnetoresistance curves of exfoliated $CrNb_3S_6$ films with the thicknesses from 28 nm to 280 nm measured at 250 mK [31]. (e) Thickness dependence of the critical field B_C. (f) $[R(0.5\text{ T}) - R(B_C)]/R(0)$ as a function of the film thickness. The result shows the magnetoresistance continuously decreases when $B > B_C$ and with increasing the thickness.

Chapter 2

Spin transport

Spintronics is one of the most active research fields in recent condensed matter physics. The most important achievement in spintronics is the discovery of giant magnetoresistance (GMR). The GMR was first observed in multilayers composed of alternating ferromagnetic and nonmagnetic layers on a substrate [32,33]. This effect triggered the development of magnetic field sensors where magnetic information is superimposed into electric current. While such a spin-polarized current plays an essential role in the GMR devices, modern spintronics relies on pure spin current, that is the flow of spin angular momentum without flow of charge. [34–39]. Since the pure spin current is not accompanied by charge flow, devices based on the pure spin current would contribute to energy saving. On the other hand, those devices can also be used for detecting spin-related phenomena in nanoscale magnets [5–8]. In this chapter, we first describe the concept of pure spin current. The ISHE is a powerful tool which can detect the pure spin current not only in nonmagnetic materials with strong spin-orbit interactions but also in magnetic materials. We introduce the SHE and the ISHE in Sec. 2.2, followed by the detailed theoretical expressions in Sec. 2.3. Sections 2.4 and 2.5 are devoted to explain two examples of ISHE in magnetic systems.

2.1 Pure spin current

An electron has two degrees of freedom, i.e., charge and spin. Flow of the spin is called the spin current, analogous to the charge current. The spin current is classified into two categories: spin polarized current and pure spin current. The former is simply realized by flowing an electric current in magnetic materials. On the other hand, the latter means only a flow of spin angular momentum with no net flow of charge, and is not so easily realized compared to the former. The schematic image of the pure spin current is shown in Fig. 2.1. Electrons with up-spin and down-spin move in opposite directions. Consequently, this situation can be regarded as two up-spins moving with no charge flow. In the following, we introduce two methods to generate and detect the pure spin current.

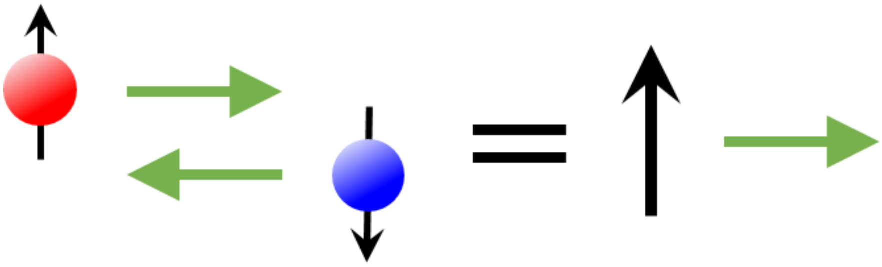

Figure 2.1: Schematic image of the pure spin current. When an up-spin electron flows from left to right and a down-spin electron flows from right to left, an electric charge is canceled out but only the spin angular momentum flows from left to right.

2.2 Spin Hall effect

One of the methods to generate pure spin current is to use the SHE [1–4]. Figure 2.2 shows the schematic images of the SHE and its inverse effect (ISHE). When a charge current flows in a nonmagnetic material with strong spin-orbit interaction, electrons with up-spin and down-spin are scattered in opposite directions. As a result, a pure spin current is generated in the orthogonal direction to the charge current and the quantization axis of the spin. In the same way, a charge current is generated when a pure spin current is injected into a strong spin-orbit material. The charge current I_C, the pure spin current I_S and the quantization axis of the spin $\boldsymbol{s}$ hold the following relations:

$$\boldsymbol{I}_\mathrm{S} \propto \boldsymbol{I}_\mathrm{C} \times \boldsymbol{s}, \tag{2.1}$$

$$\boldsymbol{I}_\mathrm{C} \propto \boldsymbol{I}_\mathrm{S} \times \boldsymbol{s}. \tag{2.2}$$

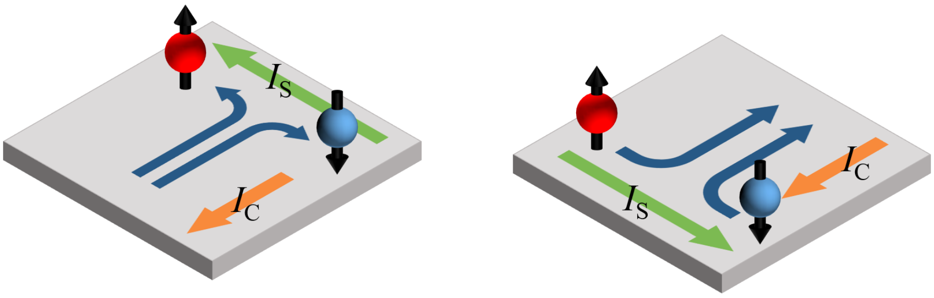

Figure 2.2: Schematic images of (a) the SHE and (b) the ISHE. I_C and I_S indicate the charge current and the pure spin current, respectively.

The magnitudes of the pure spin current density j_S and the charge current density j_C are expressed as:

$$j_S = \alpha_H^{SHE} j_C, \tag{2.3}$$

$$j_C = \alpha_H^{ISHE} j_S, \tag{2.4}$$

where α_H^{SHE} and α_H^{ISHE} are conversion efficiencies, called the spin Hall angles. α_H^{SHE} is generally equal to α_H^{ISHE} based on the Onsager reciprocal relation, i.e.,

$$\alpha_H^{SHE} = \alpha_H^{ISHE} \equiv \alpha_H. \tag{2.5}$$

The SHE was originally predicted by D'yakonov and Perel' in 1971 [2]. However, it had not attracted much attention because there was no experimental way to detect the pure spin current. About 30 years later, in 1999, Hirsch shed light on the SHE again [3]. In 2003, Kato *et al.* observed spin accumulation at both edges of a semiconductor GaAs thin wire using the optical Kerr effect [4]. It was the first direct observation of the SHE.

The ISHE was first measured in a NiFe/Pt bilayer film by Saitoh *et al* [40]. By applying a microwave to the film, a ferromagnetic resonance occurs in the NiFe layer and a pure spin current is injected into the Pt layer. The generated pure spin current is converted into a charge current due to the ISHE, resulting in charge accumulation. In the same year, Valenzuela and Tinkham measured the ISHE in Al by using the nonlocal spin injection method [41], as detailed in the next section.

2.3 Nonlocal spin injection method

There is another way to generate the pure spin current, that is nonlocal spin injection in the lateral spin valve structure. This method was first tested by Johnson and Silsbee in 1985 [34]. They obtained spin accumulation signal of the order of pV in Al/NiFe micrometer-scale structure. This was revisited by Fedema *et al.* in 2002 using sub-micrometer lateral spin valve devices. They obtained more than 1000 times larger spin accumulation signals, compared to Johnson and Silsbee. The spin accumulation in the lateral spin valve structure was then formulated by Takahashi and Maekawa [42, 43]. In the following subsection, we will explain some theoretical expressions based on the one-dimensional (1D) spin diffusion model proposed by Takahashi and Maekawa.

2.3.1 Nonlocal spin valve

The nonlocal spin valve (NLSV) structure consists of two ferromagnetic wires and one nonmagnetic wire as shown in Fig. 2.3. A ferromagnetic injector F1 is aligned parallel to another ferromagnetic detector F2. They are connected with a nonmagnetic wire N. The magnetization direction of F1 and F2 is parallel or antiparallel along the wire due to the magnetic anisotropy. We define the origin at the junction between F1 and N, and take the x- and y-axes along the N and F1 wires, respectively. The z-axis is perpendicular to the x-y plane. The dimension (thickness t_{F} and width w_{F}) of F1 and F2 is the same and the distance between F1 and F2 is L. When a charge current is injected from F1 to N, spin accumulation is generated at the interface between F1 and N. This spin accumulation results in a pure spin current only at the right side of the N wire. Figure 2.4 shows the electrochemical potential in the N channel. In the N channel for $0 < x < L$, up-spin and down-spin currents flow along the $+x$ and $-x$ directions, respectively. The current density for spin σ, $\boldsymbol{j}_{\sigma}$, can be described by the standard Ohm's law and an additional term, drift current $eD_{\sigma}\boldsymbol{\nabla}\delta n_{\sigma}$, as follows:

$$\boldsymbol{j}_{\sigma} = \sigma_{\sigma}\boldsymbol{E} + eD_{\sigma}\boldsymbol{\nabla}\delta n_{\sigma}, \tag{2.6}$$

where σ_{σ} is the electrical conductivity for spin σ, $\boldsymbol{E}$ is the electric field, $\boldsymbol{\nabla} n_{\sigma}$ is a deviation from the equilibrium state of charge density, and D_{σ} is the diffusion constant.

Here we introduce an electrochemical potential $\mu_{\sigma} = -e\phi + \dfrac{\delta n_{\sigma}}{N_{\sigma}}$. N_{σ} is the density of state for spin σ. σ_{σ} can be written as $\sigma_{\sigma} = e^2 N_{\sigma} D_{\sigma}$ using the Einstein

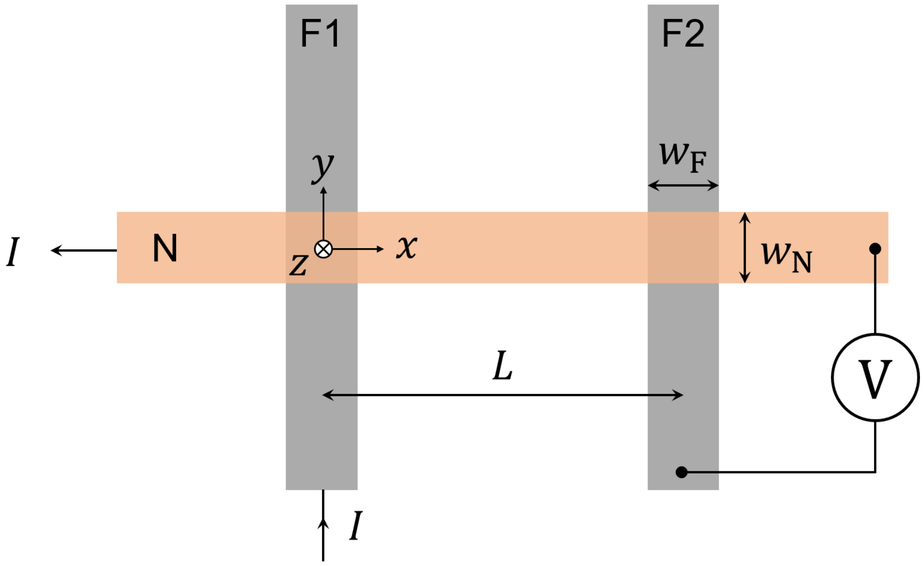

Figure 2.3: Schematic image of the top view of the NLSV device.

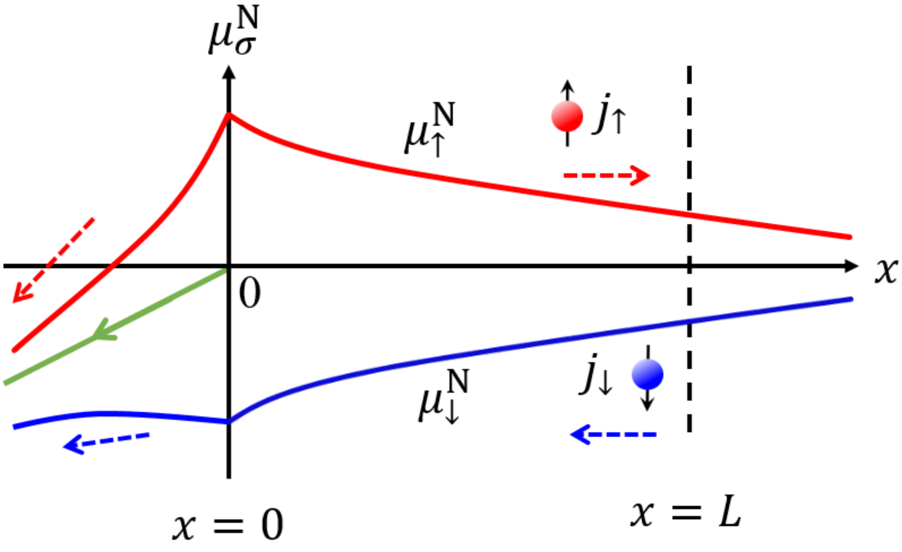

Figure 2.4: Electrochemical potential distribution in the N channel.

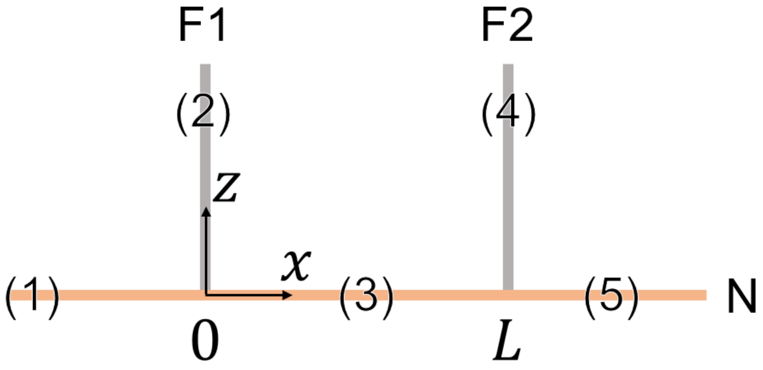

Figure 2.5: Five different segments to calculate the electrochemical potential using the 1D spin diffusion model.

relation. Thus, Eq. (2.6) can be rewritten as

$$\boldsymbol{j}_\sigma = -\frac{\sigma}{e}\nabla\mu_\sigma. \tag{2.7}$$

The charge current density $\boldsymbol{j}_\mathrm{C}$ and spin current density $\boldsymbol{j}_\mathrm{S}$ can be described as

$$\begin{aligned} \boldsymbol{j}_\mathrm{C} &= \boldsymbol{j}_\uparrow + \boldsymbol{j}_\downarrow, && (2.8) \\ \boldsymbol{j}_\mathrm{S} &= \boldsymbol{j}_\uparrow - \boldsymbol{j}_\downarrow. && (2.9) \end{aligned}$$

By using Eq. (2.7), the continuous equations for charge and spin currents in a steady state can be expressed as

$$\begin{aligned} \nabla\cdot(\boldsymbol{j}_\uparrow + \boldsymbol{j}_\downarrow) &= 0, && (2.10) \\ \nabla\cdot(\boldsymbol{j}_\uparrow - \boldsymbol{j}_\downarrow) &= -\frac{e\delta_{n\uparrow}}{\tau_{\uparrow\downarrow}} + \frac{e\delta_{n\downarrow}}{\tau_{\downarrow\uparrow}}. && (2.11) \end{aligned}$$

Here $\tau_{\sigma\sigma'}$ is the spin scattering time from σ to σ'. By using Eq. (2.7), Eqs. (2.10) and (2.11) can be rewritten as

$$\nabla^2(\sigma_\uparrow\mu_\uparrow + \sigma_\downarrow\mu_\downarrow) = 0, \tag{2.12}$$

$$\begin{aligned}\nabla^2\left(\mu_\uparrow-\mu_\downarrow\right) &= -\frac{e^2}{\sigma_\uparrow}\left(-\frac{\delta n_\uparrow}{\tau_{\uparrow\downarrow}}+\frac{\delta n_\downarrow}{\tau_{\downarrow\uparrow}}\right)+\frac{e^2}{\sigma_\downarrow}\left(\frac{\delta n_\uparrow}{\tau_{\uparrow\downarrow}}-\frac{\delta n_\downarrow}{\tau_{\downarrow\uparrow}}\right)\\ &= \frac{1}{N_\uparrow D_\uparrow}\left(\frac{\delta n_\uparrow}{\tau_{\uparrow\downarrow}}-\frac{\delta n_\downarrow}{\tau_{\downarrow\uparrow}}\right)+\frac{1}{N_\downarrow D_\downarrow}\left(\frac{\delta n_\uparrow}{\tau_{\uparrow\downarrow}}-\frac{\delta n_\downarrow}{\tau_{\downarrow\uparrow}}\right).\end{aligned} \tag{2.13}$$

Using detailed balancing $\frac{N_\uparrow}{\tau_{\uparrow\downarrow}}=\frac{N_\downarrow}{\tau_{\downarrow\uparrow}}$, one obtains the following expression:

$$\nabla^2\left(\mu_\uparrow-\mu_\downarrow\right)=\frac{1}{D\tau_{\mathrm{sf}}}\left(\mu_\uparrow-\mu_\downarrow\right), \tag{2.14}$$

with the definitions

$$\frac{1}{D} \equiv \frac{N_\uparrow {D_\downarrow}^{-1}+N_\downarrow {D_\uparrow}^{-1}}{N_\uparrow+N_\downarrow}, \tag{2.15}$$

$$\frac{1}{\tau_{\mathrm{sf}}} \equiv \frac{1}{2}\left(\frac{1}{\tau_{\uparrow\downarrow}}+\frac{1}{\tau_{\downarrow\uparrow}}\right). \tag{2.16}$$

Because the spin diffusion length λ is derived from

$$\lambda=\sqrt{D\tau_{\mathrm{sf}}}, \tag{2.17}$$

Eq. (2.14) is rewritten as

$$\nabla^2(\mu_\uparrow-\mu_\downarrow)=\lambda^{-2}(\mu_\uparrow-\mu_\downarrow). \tag{2.18}$$

To calculate the electrochemical potentials and the current densities for up-spin and down-spin using Eqs. (2.10) and (2.18), we divide the nonlocal spin valve device into 5 parts as shown in Fig. 2.5. By considering the boundary conditions at all the junctions, the spin accumulation between F2 and N can be obtained. The detailed discussion is desicribed below.

(1) $x<0$ (N part)
The electrochemical potential for up-spin in this part is

$$\mu_\uparrow=\frac{eI}{\sigma_{\mathrm{N}}A_{\mathrm{N}}}x+a_1e^{\frac{x}{\lambda_{\mathrm{N}}}}, \tag{2.19}$$

and that for down-spin is

$$\mu_\downarrow = \frac{eI}{\sigma_{\mathrm{N}} A_{\mathrm{N}}} x - a_1 e^{\frac{x}{\lambda_{\mathrm{N}}}}, \tag{2.20}$$

where $A_{\mathrm{N}} = w_{\mathrm{N}} t_{\mathrm{N}}$ (w_{N}: width of N wire and t_{N}: thickness of N wire) is the cross-section area of the N wire. By using Eqs. (2.19), (2.20), and (2.7), the current densities for up-spin and down-spin are obtained:

$$j_\uparrow = -\frac{\sigma_{\mathrm{N}}^\uparrow}{e} \left(\frac{eI}{\sigma_{\mathrm{N}} A_{\mathrm{N}}} + \frac{a_1}{\lambda_{\mathrm{N}}} a_1 e^{\frac{x}{\lambda_{\mathrm{N}}}} \right), \tag{2.21}$$

$$j_\downarrow = -\frac{\sigma_{\mathrm{N}}^\downarrow}{e} \left(\frac{eI}{\sigma_{\mathrm{N}} A_{\mathrm{N}}} - \frac{a_1}{\lambda_{\mathrm{N}}} a_1 e^{\frac{x}{\lambda_{\mathrm{N}}}} \right). \tag{2.22}$$

For example, the charge current I_{C} is

$$I_{\mathrm{C}} = (j_\uparrow + j_\downarrow) A_{\mathrm{N}} = -I, \tag{2.23}$$

and the spin current I_{S} is

$$I_{\mathrm{S}} = (j_\uparrow - j_\downarrow) A_{\mathrm{N}} = -\frac{A_{\mathrm{N}} \sigma_{\mathrm{N}}}{e \lambda_{\mathrm{N}}} a_1 e^{\frac{x}{\lambda_{\mathrm{N}}}} = -\frac{a_1}{e R_{\mathrm{N}}} e^{\frac{x}{\lambda_{\mathrm{N}}}}, \tag{2.24}$$

where $R_{\mathrm{N}} = \dfrac{\lambda_{\mathrm{N}}}{\sigma_{\mathrm{N}} A_{\mathrm{N}}}$ is the spin resistance in the N wire. Thus, from the boundary conditions at $x = 0$, three equations

$$\begin{aligned} I_{\mathrm{S}}(x=0) &= -\frac{a_1}{e R_{\mathrm{N}}}, & (2.25)\\ \mu_\uparrow(x=0) &= a_1, & (2.26)\\ \mu_\downarrow(x=0) &= -a_1, & (2.27) \end{aligned}$$

are obtained.

(2) $x = 0, z > 0$ (F1 part)
The electrochemical potential for up-spin in this part is

$$\mu_\uparrow = eV_1 + \frac{eI}{\sigma_{\mathrm{F}} A_{\mathrm{F}}} z + \frac{\sigma_{\mathrm{F}}}{\sigma_{\mathrm{F}}^\uparrow} b_1 e^{-\frac{z}{\lambda_{\mathrm{F}}}}, \tag{2.28}$$

and that for down-spin is

$$\mu_\downarrow = eV_1 + \frac{eI}{\sigma_\mathrm{F} A_\mathrm{F}} z - \frac{\sigma_\mathrm{F}}{\sigma_\mathrm{F}^\downarrow} b_1 e^{-\frac{z}{\lambda_\mathrm{F}}}, \tag{2.29}$$

where $A_\mathrm{F} = w_\mathrm{F} w_\mathrm{N}$ is the area of the junction of the F wire and the N wire. By using Eqs. (2.28), (2.29), and (2.7), the current densities for up-spin and down-spin are expressed as

$$j_\uparrow = -\frac{\sigma_\mathrm{F}^\uparrow}{e}\left(\frac{eI}{\sigma_\mathrm{F} A_\mathrm{F}} - \frac{b_1}{\lambda_\mathrm{F}}\frac{\sigma_\mathrm{F}}{\sigma_\mathrm{F}^\uparrow} e^{-\frac{z}{\lambda_\mathrm{F}}}\right), \tag{2.30}$$

$$j_\downarrow = -\frac{\sigma_\mathrm{F}^\downarrow}{e}\left(\frac{eI}{\sigma_\mathrm{F} A_\mathrm{F}} + \frac{b_1}{\lambda_\mathrm{F}}\frac{\sigma_\mathrm{F}}{\sigma_\mathrm{F}^\downarrow} e^{-\frac{z}{\lambda_\mathrm{F}}}\right). \tag{2.31}$$

Thus, the charge current I_C is

$$I_\mathrm{C} = (j_\uparrow + j_\downarrow) A_\mathrm{F} = -\frac{\sigma_\mathrm{F}^\uparrow + \sigma_\mathrm{F}^\downarrow}{\sigma_\mathrm{F}} I = -I, \tag{2.32}$$

and the spin current I_S is

$$\begin{aligned} I_\mathrm{S} = (j_\uparrow - j_\downarrow) A_\mathrm{F} &= -\frac{\sigma_\mathrm{F}^\uparrow - \sigma_\mathrm{F}^\downarrow}{I} + \frac{2A_\mathrm{F}\sigma_\mathrm{F}}{e\lambda_\mathrm{F}} b_1 e^{-\frac{z}{\lambda_\mathrm{F}}} \\ &= -p_\mathrm{F} I + \frac{2b_1}{eR_\mathrm{F}(1-{p_\mathrm{F}}^2)} e^{-\frac{z}{\lambda_\mathrm{F}}}, \end{aligned} \tag{2.33}$$

where $R_\mathrm{F} = \dfrac{\lambda_\mathrm{F}}{(1-{p_\mathrm{F}}^2)\sigma_\mathrm{F} A_\mathrm{F}}$ is the spin resistance in the F wire, and $p_\mathrm{F} = \dfrac{\sigma_\mathrm{F}^\uparrow - \sigma_\mathrm{F}^\downarrow}{\sigma_\mathrm{F}^\uparrow + \sigma_\mathrm{F}^\downarrow}$ is the spin polarization. From the boundary conditions at $z = 0$, three equations

$$I_\mathrm{S} = -p_\mathrm{F} I + \frac{2b_1}{eR_\mathrm{F}(1-{p_\mathrm{F}}^2)}, \tag{2.34}$$

$$\mu_\uparrow(z=0) = eV_1 + \frac{\sigma_\mathrm{F}}{\sigma_\mathrm{F}^\uparrow} b_1, \tag{2.35}$$

$$\mu_\downarrow = eV_1 - \frac{\sigma_\mathrm{F}}{\sigma_\mathrm{F}^\downarrow}, \tag{2.36}$$

are obtained.

(3) $0 < x < L$ (N part)
The electrochemical potential for up-spin in this part is

$$\mu_\uparrow = a_2 e^{-\frac{x}{\lambda_\mathrm{N}}} + a_3 e^{\frac{x}{\lambda_\mathrm{N}}}, \tag{2.37}$$

and that for down-spin is

$$\mu_\downarrow = -a_2 e^{-\frac{x}{\lambda_\mathrm{N}}} - a_3 e^{\frac{x}{\lambda_\mathrm{N}}}. \tag{2.38}$$

By using Eqs. (2.37), (2.38), and (2.7), the current densities for up-spin and down-spin are

$$\begin{aligned} j_\uparrow &= -\frac{\sigma_\mathrm{N}^\uparrow}{e}\left(-\frac{a_2}{\lambda_\mathrm{N}} e^{-\frac{x}{\lambda_\mathrm{N}}} + \frac{a_3}{\lambda_\mathrm{N}} e^{\frac{x}{\lambda_\mathrm{N}}}\right), &(2.39)\\ j_\downarrow &= -\frac{\sigma_\mathrm{N}^\downarrow}{e}\left(\frac{a_2}{\lambda_\mathrm{N}} e^{-\frac{x}{\lambda_\mathrm{N}}} - \frac{a_3}{\lambda_\mathrm{N}} e^{\frac{x}{\lambda_\mathrm{N}}}\right). &(2.40)\end{aligned}$$

Thus, the charge current I_C is

$$I_\mathrm{C} = (j_\uparrow + j_\downarrow) A_\mathrm{N} = 0, \tag{2.41}$$

and the spin current I_S is

$$I_\mathrm{S} = \frac{\sigma_\mathrm{N} A_\mathrm{N}}{e\lambda_\mathrm{N}} (a_2 e^{-\frac{x}{\lambda_\mathrm{N}}} - a_3 e^{\frac{x}{\lambda_\mathrm{N}}}). \tag{2.42}$$

From the boundary conditions at $x = 0$, three equations

$$\begin{aligned} I_s(x=0) &= \frac{1}{eR_\mathrm{N}}(a_2 - a_3), &(2.43)\\ \mu_\uparrow(x=0) &= a_2 + a_3, &(2.44)\\ \mu_\downarrow(x=0) &= -a_2 - a_3, &(2.45)\end{aligned}$$

are obtained. Similarly, from the boundary conditions at $x = L$, three equations

$$\begin{aligned} I_s(x=L) &= \frac{1}{eR_\mathrm{N}}\left(a_2 e^{\frac{-L}{\lambda_\mathrm{N}}} - a_3 e^{\frac{L}{\lambda_\mathrm{N}}}\right), &(2.46)\\ \mu_\uparrow(x=L) &= a_2 e^{\frac{-L}{\lambda_\mathrm{N}}} + a_3 e^{\frac{L}{\lambda_\mathrm{N}}}, &(2.47)\\ \mu_\downarrow(x=L) &= -a_2 e^{\frac{-L}{\lambda_\mathrm{N}}} - a_3 e^{\frac{L}{\lambda_\mathrm{N}}}, &(2.48)\end{aligned}$$

are also derived.

(4) $x = L, z > 0$ (F2 part)
The electrochemical potential for up-spin in this part is

$$\mu_\uparrow = eV_2 + \frac{\sigma_\mathrm{F}}{\sigma_\mathrm{F}^\uparrow} b_2 e^{-\frac{z}{\lambda_\mathrm{N}}}, \tag{2.49}$$

and that for down-spin is

$$\mu_\downarrow = eV_2 - \frac{\sigma_\mathrm{F}}{\sigma_\mathrm{F}^\downarrow} b_2 e^{-\frac{z}{\lambda_\mathrm{N}}}. \tag{2.50}$$

By using Eqs. (2.49), (2.50), and (2.7), the current densities for up-spin and down-spin are

$$j_\uparrow = -\frac{\sigma_\mathrm{F}^\uparrow}{e}\left(-\frac{\sigma_\mathrm{F}}{\lambda_\mathrm{F}\sigma_\mathrm{F}^\uparrow}\right) b_2 e^{-\frac{z}{\lambda_\mathrm{F}}}, \tag{2.51}$$

$$j_\downarrow = -\frac{\sigma_\mathrm{F}^\downarrow}{e}\left(-\frac{\sigma_\mathrm{F}}{\lambda_\mathrm{F}\sigma_\mathrm{F}^\downarrow}\right) b_2 e^{-\frac{z}{\lambda_\mathrm{F}}}. \tag{2.52}$$

Thus, the charge current I_C is

$$I_\mathrm{C} = (j_\uparrow + j_\downarrow) A_\mathrm{F} = 0, \tag{2.53}$$

and the spin current I_S is

$$I_\mathrm{S} = \frac{2\sigma_\mathrm{F} A_\mathrm{F} b_2}{e\lambda_\mathrm{F}} e^{-\frac{z}{\lambda_\mathrm{F}}} = \frac{2b_2}{eR_\mathrm{F}(1 - p_\mathrm{F}{}^2)} e^{-\frac{z}{\lambda_\mathrm{F}}}. \tag{2.54}$$

From the boundary conditions at $z = 0$, three equations

$$I_\mathrm{S}(z = 0) = \frac{2b_2}{eR_\mathrm{F}(1 - p_\mathrm{F}{}^2)}, \tag{2.55}$$

$$\mu_\uparrow(z = 0) = eV_2 + \frac{\sigma_\mathrm{F}}{\sigma_\mathrm{F}^\uparrow} b_2, \tag{2.56}$$

$$\mu_\downarrow(z = 0) = eV_2 - \frac{\sigma_\mathrm{F}}{\sigma_\mathrm{F}^\downarrow} b_2, \tag{2.57}$$

are obtained.

(5) $x > L$ (N part)
The electrochemical potential for up-spin in this part is

$$\mu_{\uparrow} = a_4 e^{-\frac{x}{\lambda_{\mathrm{N}}}}, \tag{2.58}$$

and that for down-spin is

$$\mu_{\downarrow} = -a_4 e^{-\frac{x}{\lambda_{\mathrm{N}}}}. \tag{2.59}$$

By using (2.58), (2.59), and (2.7), the current densities for up-spin and down-spin are

$$j_{\uparrow} = \frac{\sigma_{\mathrm{N}}^{\uparrow} a_4}{e\lambda_{\mathrm{N}}} e^{-\frac{x}{\lambda_{\mathrm{N}}}}, \tag{2.60}$$

$$j_{\downarrow} = -\frac{\sigma_{\mathrm{N}}^{\downarrow} a_4}{e\lambda_{\mathrm{N}}} e^{-\frac{x}{\lambda_{\mathrm{N}}}}. \tag{2.61}$$

Thus, the charge current I_{C} is

$$I_{\mathrm{C}} = (j_{\uparrow} + j_{\downarrow}) A_{\mathrm{N}} = 0. \tag{2.62}$$

and the spin current I_{S} is

$$I_{\mathrm{S}} = (j_{\uparrow} + j_{\downarrow}) A_{\mathrm{N}} = -\frac{\sigma_{\mathrm{N}} A_{\mathrm{N}} a_4}{e\lambda_{\mathrm{N}}} e^{-\frac{x}{\lambda_{\mathrm{N}}}}. \tag{2.63}$$

From the boundary conditions at $x = L$, three equations

$$\begin{array}{rcl} I_{\mathrm{S}}(x=L) & = & \dfrac{a_4}{eR_{\mathrm{N}}} e^{-\frac{L}{\lambda_{\mathrm{N}}}}, \qquad (2.64) \\ \mu_{\uparrow}(x=L) & = & a_4 e^{-\frac{L}{\lambda_{\mathrm{N}}}}, \qquad (2.65) \\ \mu_{\downarrow}(x=L) & = & -a_4 e^{-\frac{L}{\lambda_{\mathrm{N}}}}, \qquad (2.66) \end{array}$$

are obtained.

By solving the simultaneous equations Eqs. (2.25) - (2.66) for V_2, the spin accumulation at $x = L$

$$\mathcal{R}_{\mathrm{S}} \equiv \frac{V_2}{I} = \frac{2{p_{\mathrm{F}}}^2 R_{\mathrm{N}} e^{-\frac{L}{\lambda_{\mathrm{N}}}}}{\left(\frac{R_{\mathrm{N}}}{R_{\mathrm{F}}} + 2\right)^2 - \left(\frac{R_{\mathrm{N}}}{R_{\mathrm{F}}}\right)^2 e^{-\frac{2L}{\lambda_{\mathrm{N}}}}}, \tag{2.67}$$

can be obtained. In an actual device, we measure the spin signal, that is $\Delta R_{\mathrm{S}} \equiv \dfrac{2V_2}{I}$ as shown in Fig. 2.6.

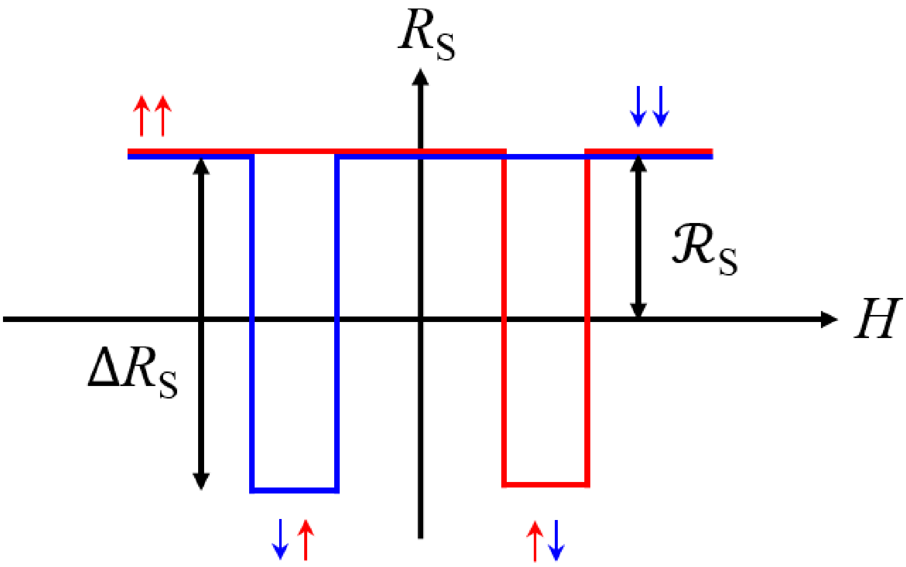

Figure 2.6: Spin signal ΔR_{S} expected in the NLSV device. The arrows in the figure indicate the magnetization directions of F1 and F2.

2.3.2 Nonlocal spin valve with a middle wire

As mentioned in the previous subsection, a pure spin current can be generated and detected by using the NLSV device. Now we consider the situation that a middle (M) wire with strong spin-orbit interaction is placed just in between the F1 and F2 wires, as shown in Fig. 2.7. In such a case, a part of the pure spin current is absorbed perpendicularly to the M wire before reaching the F2 wire because of the stronger spin-orbit interaction. By comparing NLSV signals with and without the M wire, we can estimate how much of the pure spin current generated at the F1/N interface is absorbed into the M wire.

By following the same calculation procedure as in the previous subsection, the spin signal with the M wire is given by

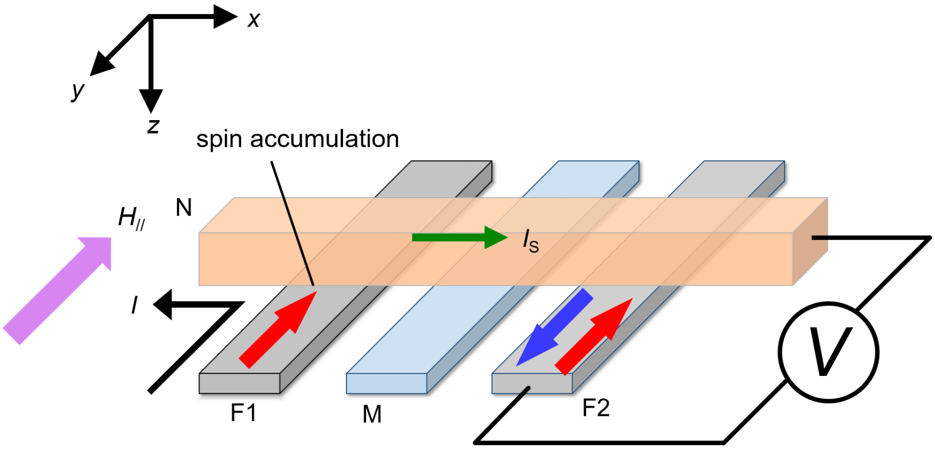

Figure 2.7: Schematic image of NLSV device with a middle wire.

$$\Delta R_{\mathrm{S}}{}^{\mathrm{with}} = \frac{4 p_{\mathrm{F}}{}^{2} Q_{\mathrm{F}}{}^{2} Q_{\mathrm{M}} R_{\mathrm{N}}}{\cosh\left(\frac{L}{\lambda_{\mathrm{N}}}\right) - 1 + 2Q_{\mathrm{M}} \sinh\left(\frac{L}{\lambda_{\mathrm{N}}}\right) + 2Q_{\mathrm{F}} \left\{ e^{\frac{L}{\lambda_{\mathrm{N}}}} (1 + Q_{\mathrm{F}})(1 + 2Q_{\mathrm{M}}) - 1 \right\}}, \tag{2.68}$$

where $Q_{\mathrm{X}} = \dfrac{R_{\mathrm{X}}}{R_{\mathrm{N}}}$ $(\mathrm{X} = \mathrm{M}, \mathrm{F})$. Thus, the reduction rate of spin signal $\eta \equiv \dfrac{\Delta R_{\mathrm{S}}{}^{\mathrm{with}}}{\Delta R_{\mathrm{S}}{}^{\mathrm{without}}}$ is given by

$$\begin{aligned} \eta &\equiv \frac{\Delta R_{\mathrm{S}}{}^{\mathrm{with}}}{\Delta R_{\mathrm{S}}{}^{\mathrm{without}}} \\ &= \frac{2Q_{\mathrm{M}} \left\{ \sinh\left(\frac{L}{\lambda_{\mathrm{N}}}\right) + 2Q_{\mathrm{F}} e^{\frac{L}{\lambda_{\mathrm{N}}}} + 2Q_{\mathrm{F}}{}^{2} e^{\frac{L}{\lambda_{\mathrm{N}}}} \right\}}{\cosh\left(\frac{L}{\lambda_{\mathrm{N}}}\right) - 1 + 2Q_{\mathrm{M}} \sinh\left(\frac{L}{\lambda_{\mathrm{N}}}\right) + 2Q_{\mathrm{F}} \left\{ e^{\frac{L}{\lambda_{\mathrm{N}}}} \left(1 + Q_{\mathrm{F}}\right) \left(1 + 2Q_{\mathrm{M}}\right) - 1 \right\}}. \end{aligned} \tag{2.69}$$

It should be noted that the spin diffusion length of M (λ_{M}) in Q_{M} is only the fitting parameter in Eq. (2.69). Therefore, λ_{M} can be estimated by measuring $\Delta R_{\mathrm{S}}{}^{\mathrm{with}}$ and $\Delta R_{\mathrm{S}}{}^{\mathrm{without}}$.

2.3.3 Nonlocal spin valve consisting of two different ferromagnetic wires

In order to estimate spin polarization of an unknown ferromagnetic material, we discuss NSLV consisting of two different F materials. The device structure is the same as in Fig. 2.3. We define spin polarizations of F1 and F2 as p_{F1} and p_{F2}, respectively ($p_{\mathrm{F1}} \neq p_{\mathrm{F2}}$). We also assume that p_{F1} and p_{F2} are known and unknown parameters, respectively. By following the same calculation procedure as in Sec. 2.3.1, the spin polarization p_{F2} and spin resistance R_{F2} is given by

$$\Delta R_{\mathrm{S}} = \frac{4R_{\mathrm{N}}R_{\mathrm{F1}}R_{\mathrm{F2}}p_{\mathrm{F1}}p_{\mathrm{F2}}}{(R_{\mathrm{N}}+2R_{\mathrm{F1}})(R_{\mathrm{N}}+2R_{\mathrm{F2}})e^{\frac{L}{\lambda_{\mathrm{N}}}} - {R_{\mathrm{N}}}^{2}e^{-\frac{L}{\lambda_{\mathrm{N}}}}}. \tag{2.70}$$

Since p_{F2} is only the unknown parameter in Eq. (2.70), it can be experimentally evaluated by measuring ΔR_{S}.

2.3.4 Spin Hall effect in nonlocal spin valve configuration

In case of the ordinary Hall effect, the Hall angle α_{H} is determined by Ohm's law:

$$\boldsymbol{E} = \rho\boldsymbol{j} = \begin{pmatrix} \rho_{xx} & -\rho_{yx} \\ \rho_{yx} & \rho_{yy} \end{pmatrix} \begin{pmatrix} j_x \\ j_y \end{pmatrix} = \begin{pmatrix} E_x \\ E_y \end{pmatrix}. \tag{2.71}$$

Since there is no charge current density along the y-direction (i.e., $j_y = 0$), α_{H} is defined as

$$\alpha_{\mathrm{H}} \equiv \frac{E_y}{E_x} = \frac{\rho_{yx}j_x}{\rho_{xx}j_x} = \frac{\rho_{yx}}{\rho_{xx}}. \tag{2.72}$$

In the same way, one can define the spin Hall angle. In the case of the ISHE, the pure spin current is injected into an M wire. In this case, a generated transverse electrical field is expresses as $E_{\mathrm{ISHE}} = \rho_{\mathrm{ISHE}}j_s = \alpha_{\mathrm{H}}^{\mathrm{ISHE}}\rho_{\mathrm{M}}j_s$ where ρ_{M} is the longitudinal resistivity of the M wire. This situation is illustrated in Fig. 2.8. The device consists of an F wire and an M wire bridged by an N wire. When the magnetic field is applied to along the N wire, the pure spin current is generated at the interface between F and N. It decays within λ_{N}, but if the M wire is placed within λ_{N}, it is perpendicularly absorbed into the M wire because of the stronger spin-orbit interaction. In the M wire, the absorbed pure spin current is converted to the charge current due to the ISHE. Here we note that the pure spin current must be treated as an average value along the thickness direction of the M wire because j_s exponentially decays. Thus,

j_s has to be replaced by the averaged spin current density $\bar{j}_s$ which is given by $\bar{j}_s = \frac{1}{t_\mathrm{M}} \int_0^{t_\mathrm{M}} j_s(z) dz$.

By using the relations $V_\mathrm{ISHE} = w_\mathrm{N} E_\mathrm{ISHE} = w_\mathrm{N} \alpha_\mathrm{H}^\mathrm{ISHE} \rho_\mathrm{M} \bar{j}_s$, the spin Hall angle $\alpha_\mathrm{H}^\mathrm{ISHE}$ is written as

$$\alpha_\mathrm{H}^\mathrm{ISHE} = \frac{w_\mathrm{M}}{x\rho_\mathrm{M}} \frac{V_\mathrm{ISHE}}{\bar{I}_s}, \tag{2.73}$$

where x is a factor to correct the shunting effect at the interface of N and M wires (see following discussion). The averaged spin current $\bar{I}_s$ is obtained by multiplying $\bar{j}_s$ by the sample dimension as follows:

$$\bar{j}_s = \frac{\bar{I}_s}{w_\mathrm{M} w_\mathrm{N}} = \frac{\int_0^{t_\mathrm{M}} j_s(z) dz}{t_\mathrm{M}} = \frac{\lambda_\mathrm{M}}{t_\mathrm{M}} \frac{\left(1 - e^{-\frac{t_\mathrm{M}}{\lambda_\mathrm{M}}}\right)^2}{1 - e^{-\frac{2t_\mathrm{M}}{\lambda_\mathrm{M}}}} \times I_s(z = 0). \tag{2.74}$$

In the actual device, it is necessary to correct the shunting effect when N is connected to the surface of the M wire. It is an essential issue because this value is not negligible and also depends on the resistivities of N and M. For example, this correction factor x was found to be $x \approx 0.36$ for $t_\mathrm{M} = 20$ nm at the interface between Cu and Pt [44]. This shunting factor x can be obtained by the three-dimensional simulation based on the finite element treatment.

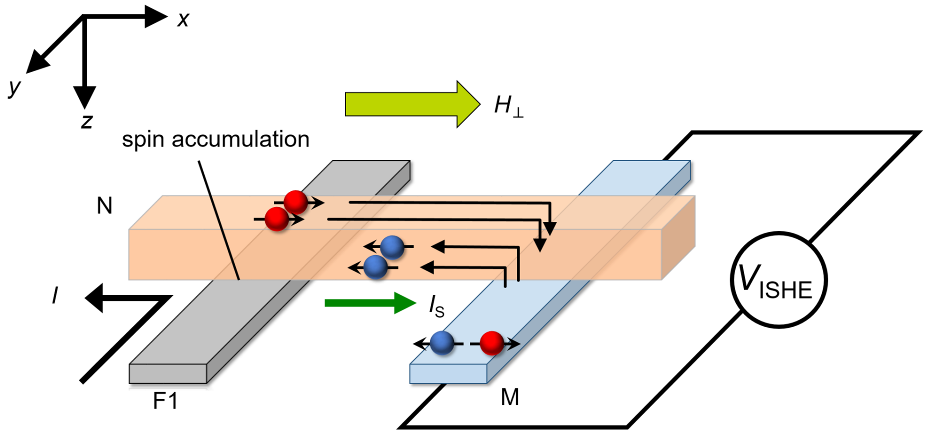

Figure 2.8: Schematic image of the ISHE measurement in the lateral spin valve structure.

2.4 Spin Hall effect in weak ferromagnet

It had been believed that the SHE is generated in nonmagnetic materials with strong spin-orbit interactions and in ferromagnetic materials the anomalous Hall effect (AHE) is measured. In fact, however, the SHE can also be measured in ferromagnetic materials. Wei *et al.* first reported the SHE in a weak ferromagnet PdNi measured by the spin absorption method [5]. They prepared $\mathrm{Pd}_{100-x}\mathrm{Ni}_x$ ($x = 7, 8, 9$) in order to investigate the SHE in the vicinity of T_C. T_C of PdNi varies from 16 to 32 K depending on the Ni concentration. Far above and below T_C, a standard ISHE signal was detected. However, an anomaly in the ISHE signal appeared only in the vicinity of T_C. The ISHE signal was suppressed and enhanced below and above T_C respectively, as shown in Fig. 2.9(a).

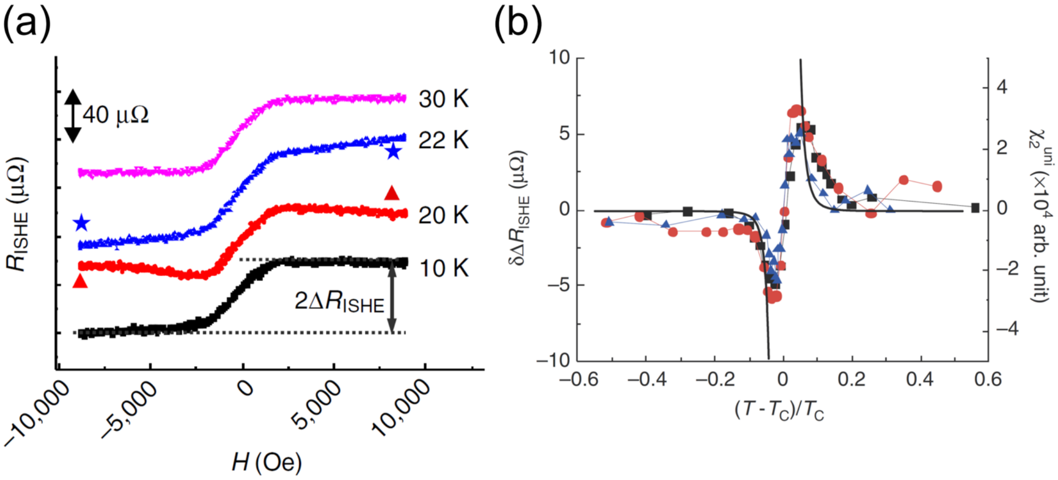

Figure 2.9: (a) The ISHE signals of $\mathrm{Pd}_{92}\mathrm{Ni}_8$ measured at T = 10, 20, 22, 30 K. (b) The anomalous component $\delta\Delta R_\mathrm{ISHE}$ for $\mathrm{Pd}_{100-x}\mathrm{Ni}_x$ as a function of the reduced temperature $(T - T_\mathrm{C})/T_\mathrm{C}$. The black, red and blue marks indicate the $\delta\Delta R_\mathrm{ISHE}$ for x = 7, 8, and 9, respectively. The solid line shows the second-order nonlinear susceptibility χ_2 for Ni moments.

To investigate the detail of the anomaly in the vicinity of T_C, they subtracted the normal ISHE component and plotted only the anomaly part $\delta\Delta R_\mathrm{ISHE}$ as a function of the reduced temperature $(T - T_\mathrm{C})/T_\mathrm{C}$ as shown in Fig. 2.9(b). The anomalous component of ΔR_ISHE is independent of the Ni concentration. This behavior can be explained qualitatively by higher-order magnetic susceptibility. In 1962, Kondo calculated the AHE in a ferromagnet including the second perturbation of the *s*-*d* Hamiltonian and revealed that the Hall resistance ρ_{H} is proportional to the first-order magnetic susceptibility χ_1 [45]. In the case of the ISHE, on the other hand, both up-spin and down-spin are accumulated to one side. As a result, the ISHE signal becomes proportional to the second-order magnetic susceptibility χ_2. Wei *et al.* has demonstrated that $\delta\Delta R_{\mathrm{ISHE}}$ near T_{C} is qualitatively consistent with the temperature dependence of χ_2 [46].

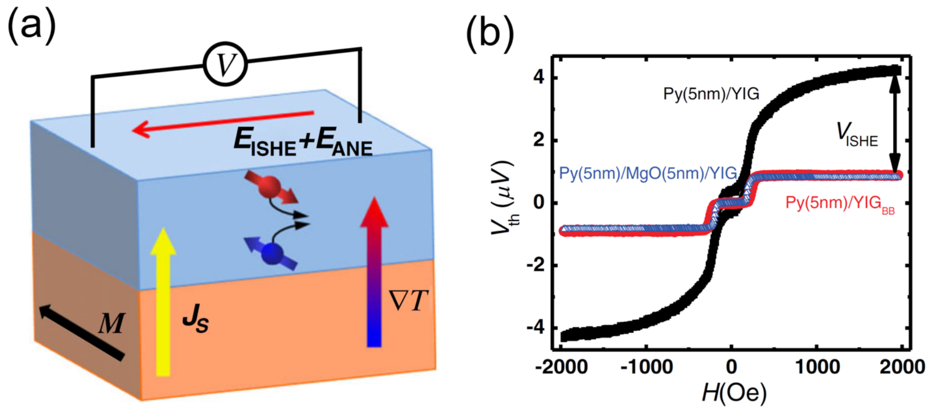

Figure 2.10: The ISHE in Py reported by Miao et al. [47]. (a) Schematic image of the Py/YIG device. (b) The spin Seebeck effect of Py/YIG device, Py/MgO/YIG and Py/surface-etched YIG, respectively.

In 2013, Miao *et al.* showed the ISHE in NiFe alloy (permalloy, heterafter Py) by using the spin Seebeck effect [47]. The spin Seebeck effect is one of the ways to generate pure spin current [48]. When a thermal gradient is applied to a paramagnetic/ferromagnetic junction, the magnetization in the ferromagnet precesses and thus a pure spin current is generated. They fabricated three spin Seebeck devices, i.e., Py/$Y_3Fe_5O_{12}$ (YIG), Py/MgO/YIG, and Py/YIG bombarded by ion-beam (YIG$_{\mathrm{BB}}$) as shown in Fig. 2.10(a). The ion-bombarded YIG surface or the insertion of MgO layer can terminate the flow of pure spin current. In this situation, the ISHE can be separated from the anomalous Nernst effect. They applied a thermal gradient perpendicular to the YIG substrate and detected the transverse voltage at the two ends of the Py film. The magnetic field dependence of the voltage is shown in Fig. 2.10(b). A clear ISHE signal was observed in the Py/YIG device, while smaller voltage signals were detected both in Py/MgO/YIG and Py/YIG$_{\mathrm{BB}}$

devices. The latter originates from the anomalous Nernst effect. Therefore, by subtracting the anomalous Nernst voltage signal from the transverse voltage measured in the Py/YIG device, not only V_{ISHE} but also the spin Hall angle α_{H} of Py can be evaluated. This was estimated to be about ~ 0.5 %. Miao *et al.* demonstrated that ferromagnetic metals can also be used as superior pure spin current detectors.

Recently, the ISHE has been observed in various magnetic materials, such as CoFeB [49], Co [50], FeGd/CoFeB bilayers [51], and even triangular antiferromagnet Mn_3Sn [52].

2.5 Spin Hall effect in spin glass

The detection of magnetic fluctuations via pure spin current was performed in spin glass systems. Spin glasses [53, 54] are typical magnetic frustrated systems where magnetic impurities are randomly distributed in nonmagnetic host metals (Fig. 2.11). It has been commonly believed that the magnetic moments start to freeze in random directions at a certain temperature, so-called spin freezing temperature T_{f} where the magnetic susceptibility shows a cusp structure [53, 54].

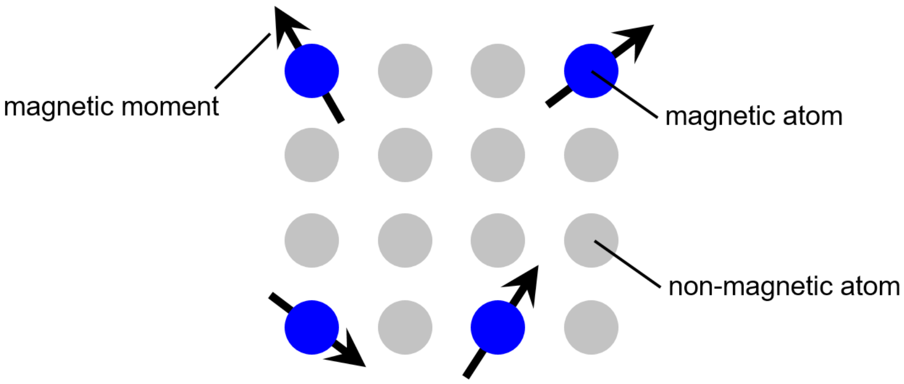

Figure 2.11: Schematic image of spin glass.

However, Niimi *et al.* proposed a new picture about spin glasses from spin transport measurements in 2015 [7]. They measured the SHE in ternary spin glass alloys: $Cu_{99.5-x}Mn_xBi_{0.5}$ (x = 0.5, 1.0, and 1.5) by using the NLSV structure (see Sec. 2.3.4). Figure 2.12 shows the temperature dependence of the SHE and ISHE resis-

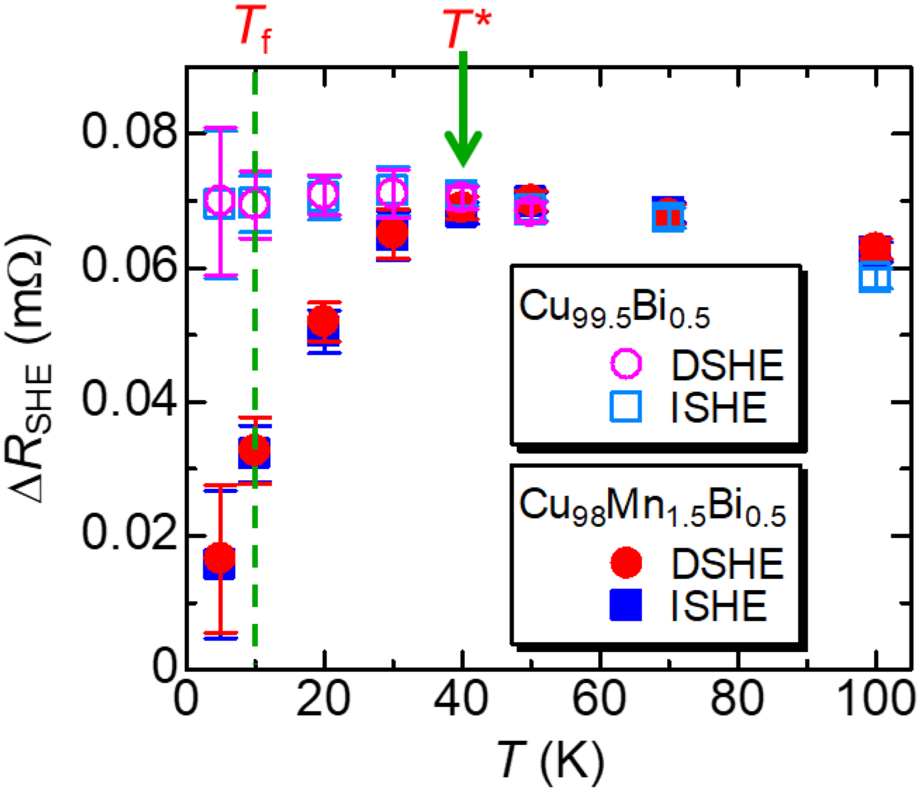

Figure 2.12: Temperature dependence of the SHE and ISHE resistances in $Cu_{98}Mn_{1.5}Bi_{0.5}$ [7].

tances in $\mathrm{Cu_{98}Mn_{1.5}Bi_{0.5}}$ nanowires. T_f shown in Fig. 2.12 is the spin freezing temperature estimated from the magnetization measurement of the thin film. According to the previous result on the SHE in PdNi [see Fig. 2.9(b)], an anomaly in the SHE near T_f had been expected since χ_2 should diverge at T_f. However, the expected anomaly was not observed at T_f. Instead, the SHE resistance in $\mathrm{Cu_{98}Mn_{1.5}Bi_{0.5}}$ starts to decrease at about 4 times higher temperature (T^*) than T_f and keeps decreasing even below T_f. The generated current I_C via the SHE can be expressed as Eq. (2.2). Therefore, the decrease of ISHE indicates the reduction of either $\boldsymbol{I}_\mathrm{S}$ or $\boldsymbol{s}$. By measuring the NLSV signal with and without the spin glass nanowire, the absorbed spin current $|I_\mathrm{S}|$ can be estimated. They found that $|I_\mathrm{S}|$ does not strongly depend on temperature. Thus, they concluded that the reduction of SHE was originated from the reduction of the spin polarization $\boldsymbol{s}$. However, the relation between T_f and T^* at which the SHE starts to decrease had not been elucidated.

Taniguchi *et al.* performed more detailed SHE measurements in $\mathrm{Cu_{99.5-\mathit{x}}Mn_\mathit{x}Bi_{0.5}}$ in 2020 [8]. Figure 2.13 shows the spin Hall angle of $\mathrm{Cu_{99.5-\mathit{x}}Mn_\mathit{x}Bi_{0.5}}$ ($x = 4.2$ and 10.6), normalized by that of $\mathrm{Cu_{99.5}Bi_{0.5}}$, as function of temperature. The reduction of the spin Hall angle below T^* was reproduced, as in the previous work [7]. In addition, they found that the spin Hall angle becomes zero at a lower temperature. This temperature is lower than T_f estimated from magnetization measurements in the $\mathrm{Cu_{99.5-\mathit{x}}Mn_\mathit{x}Bi_{0.5}}$ film.

In Fig. 2.14, the relation between the orientation of conduction electron (up- and down-) spins and magnetic fluctuations at the Mn sites is classified into three regions [(i), (ii), and (iii)] depending on temperature.

(i) $T > T^*$: In this temperature region, thermal fluctuations of Mn spins are so fast. Thus, the conduction electron spins do not feel such fluctuations and are simply scattered at the Bi site, as in the case of the ISHE in CuBi [see Fig. 2.14(a)]. As a result, the spin Hall angle takes the same value as CuBi.

(ii) $T_\mathrm{f} < T < T^*$: With decreasing temperature below T^*, the thermal fluctuations of Mn spins become slow so that the conduction electron spins can interact with the localized magnetic moments in the Mn sites [see Fig. 2.14(b)]. In this case, the conduction electron spins can feel the magnetic fluctuations at the Mn sites, and are randomized by the Mn spins. Therefore, the effective polarization of conduction electron spins becomes smaller, resulting in a reduction of the spin Hall angle. Note that this temperature region cannot be detected by conventional magnetization measurements.

(iii) $T < T_\mathrm{f}$: When the Mn spins start to freeze, the conduction electron spins are completely randomized at the Mn sites. In this case, the effective spin polarization vanishes, resulting in $\alpha_\mathrm{H} = 0$. It has been established that T_f of spin glass films

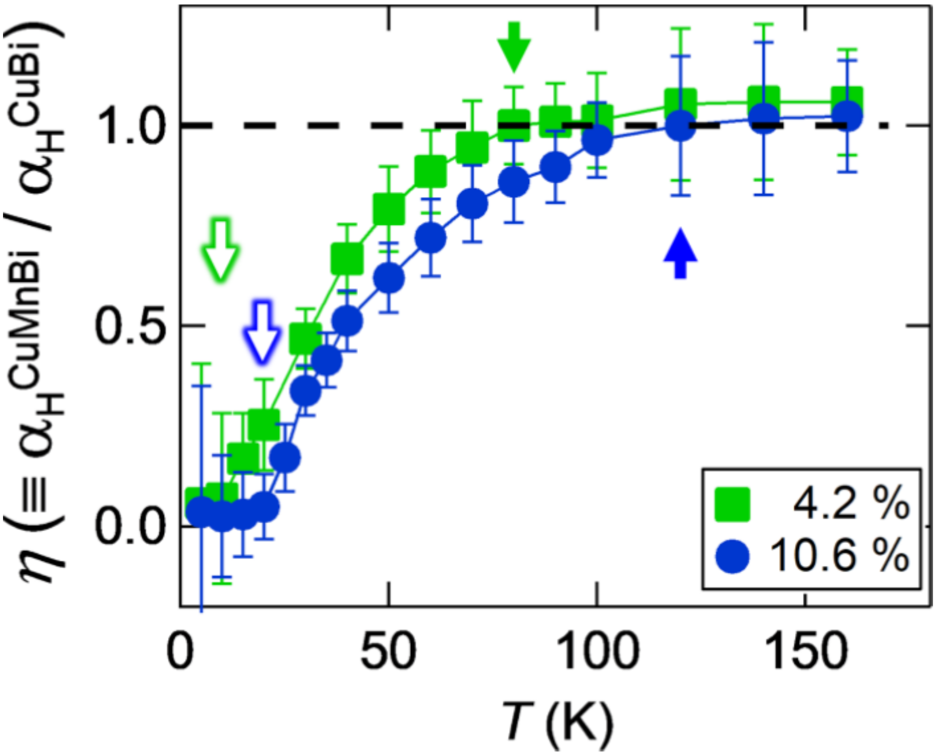

Figure 2.13: Temperature dependence of η, the spin Hall angle of $Cu_{99.5-x}Mn_xBi_{0.5}$ (x = 4.2 and 10.6) normalized by that of $Cu_{99.5}Bi_{0.5}$. The solid and open arrows indicate T^* and T_f, respectively [8].

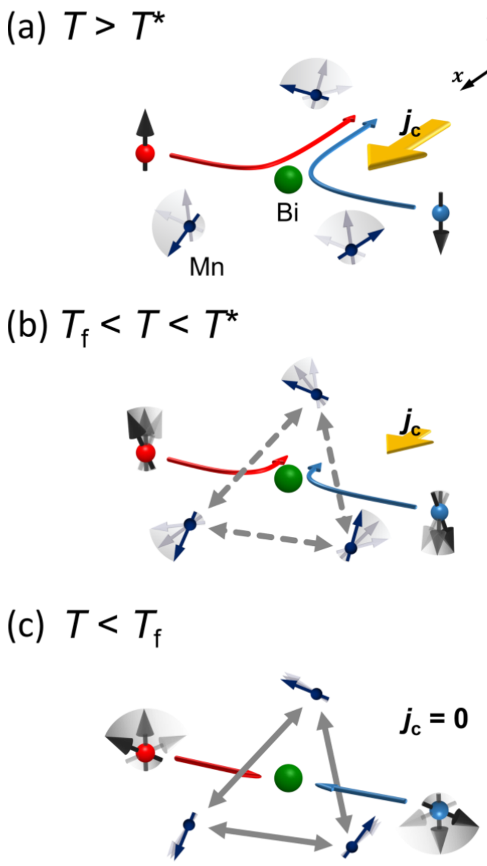

Figure 2.14: Schematic images of ISHE in $Cu_{99.5-x}Mn_xBi_{0.5}$ in three different temperature regions: (a) $T > T^*$ (paramagnetic region), (b) $T_\mathrm{f} < T < T^*$ (spin treacle region), and (c)$T < T_\mathrm{f}$ (spin glass region) [8].

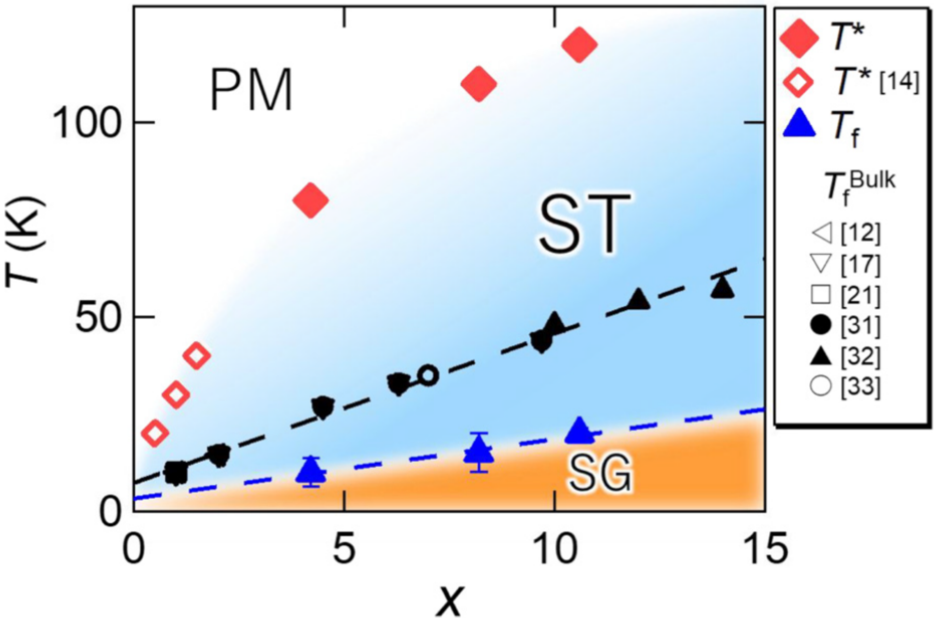

Figure 2.15: Phase diagram of $Cu_{99.5-x}Mn_xBi_{0.5}$ proposed by Taniguchi *et al.* [8]. PM, ST and SG are abbreviated expressions of paramagnetic, spin treacle and spin glass, respectively.

becomes smaller with decreasing the thickness [55, 56]. Taking these facts together, the temperature at which α_{H} becomes zero is the spin freezing temperature T_{f} of the $\mathrm{Cu}_{99.5-x}\mathrm{Mn}_x\mathrm{Bi}_{0.5}$ nanowire.

Figure 2.15 shows the phase diagram of CuMn spin glass systems. The reduction of T_{f} in nanowire is consistent with the size effect of T_{f} for thin spin glass films. From the phase diagram in Fig. 2.15, the authors concluded that there is an intermediate region, named "spin treacle" in between spin glass and paramagnetic phase. These results suggest that the pure spin current can be a powerful probe to detect magnetic fluctuations in nanoscale samples.

2.6 Mechanisms of spin relaxation

There are two kinds of mechanisms for spin relaxation induced by spin-orbit interaction, i.e., the Elliot-Yafet (EY) mechanism [57–59] and the D'yakonov-Perel' (DP) [2, 59] mechanism. In this section, we briefly review these two mechanisms.

The EY mechanism is based on ordinary momentum scatterings by phonons or impurities. In a conductor with spin-orbit interaction, electrons hit impurities or grain boundaries several times. During this process, electron spins flip, resulting in decoherence of spins [Fig. 2.16(a)]. In this case, the spin relaxation time or spin flip time τ_{sf} is simply proportional to the number of impurities or grain boundaries, i.e., the momentum relaxation time τ_p. Because τ_p is written as $1/\tau_p \sim \rho$, τ_{sf} is also proportional to $1/\rho$, where ρ is the resistivity of a conductor. In a dirty (metallic) system, the EY mechanism is usually dominant.

Unlike the EY mechanism, the DP mechanism originates from modulation of precession motion of conduction electron spins due to the impurity scatterings. The conduction electron spin precesses around the effective magnetic field generated by spin-orbit interaction at a frequency of $\Omega(\boldsymbol{k})$. During this precession motion, the electron hits some impurities in a conductor, resulting in modulation of the direction of spin (i.e., phase) by $\delta\phi = \Omega(\boldsymbol{k})\tau_p$ [Fig. 2.16(b)]. Since the electron motion in a conductor is diffusive, the phase modulation due to the random walk during the time t is given by $\phi(t) = \sqrt{\frac{t}{\tau_p}}\Omega_{\mathrm{av}}\tau_p$ where Ω_{av} is the averaged value of $\Omega(\boldsymbol{k})$. When $\phi(t)$ is about 1, the time t corresponds to the spin relaxation time τ_{sf}, leading to $\frac{1}{\tau_{\mathrm{sf}}} = \Omega_{\mathrm{av}}^2\tau_p$. In other words, τ_{sf} is inversely proportional to τ_p, which is opposite to that in the EY mechanism. It is known that in III-V semiconductors such as GaAs, the DP mechanism is dominant.

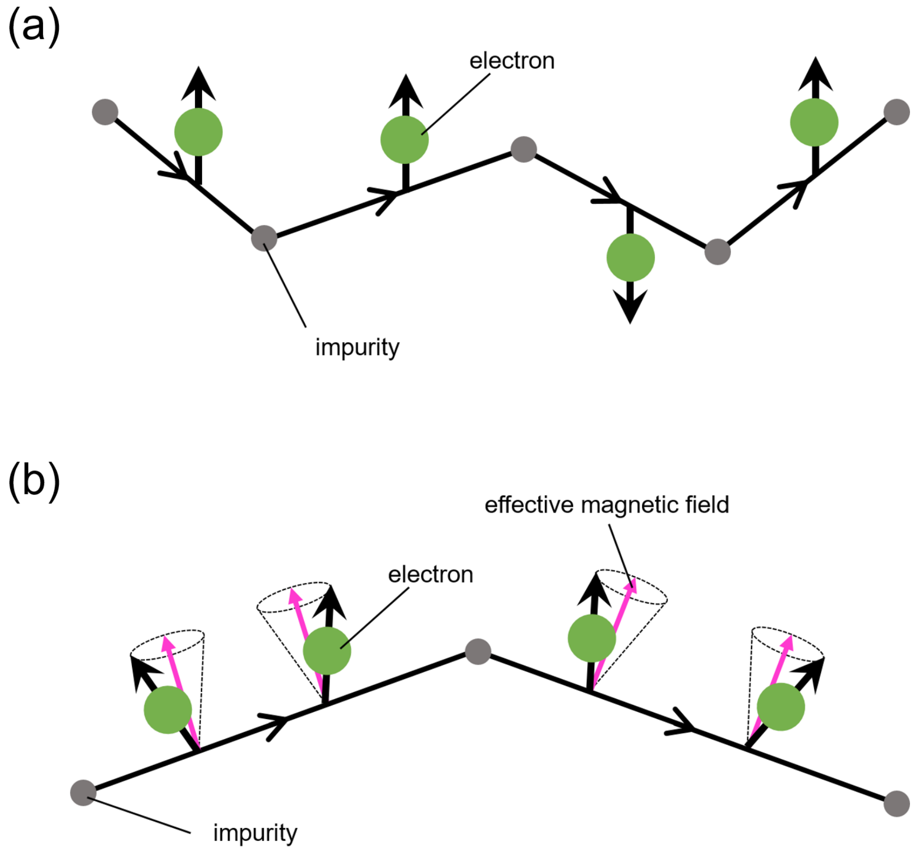

Figure 2.16: Schematic images of (a) the EY mechanism and (b) the DP mechanism.

Chapter 3

Experimental details

In this chapter, we explain nanofabrication process of $CrNb_3S_6$ thin films and also that of NLSV devices where a $CrNb_3S_6$ nanowire is included as an M wire. In order to obtain the NLSV devices, there are several points to be aware of when performing the nanofabrication processes. Those are detailed in Sec. 3.1. Section 3.2 is devoted to the measurement setup to perform spin transport with the NLSV devices.

3.1 Nanofabrication processes

3.1.1 Mechanical exfoliation technique

The mechanical exfoliation method, so-called “scotch tape technique”, is one of the ways to obtain an atomically thin film of a layered material. When the interaction between the layers is weaker than the adhesive strength of scotch tape, the layered material can be mechanically exfoliated with a scotch tape. The method has attracted much attention as an easy technique to obtain a clean two-dimensional system, since Novoselov *et al.* succeeded in making a monolayer of graphite (graphene) with the scotch tape technique for the first time [60–62]. The atomically thin films made by this method have few lattice defects because these films are extracted from the bulk single crystals. Therefore, the scotch tape technique is one of the most suitable ways to obtain nanoscale devices with high crystallinity. The scotch tape technique has been applied to various van der Waals (vdW) materials: transition metal dichalcogenides such as MoS_2 [63, 64] and $NbSe_2$ [65–68], hexagonal boron nitride (h-BN) [69–72], cuprate superconductors [73–76], magnetic materials [77–80], and so on.

NbS_2 is one of the transition metal dichalcogenides and a typical vdW material. A chiral helimagent $CrNb_3S_6$ is based on the crystal structure of NbS_2, but Cr atoms are intercalated into the two adjacent S layers. Because of this intercalation, the interlayer interaction is stronger than usual vdW materials. Therefore, we first needed to establish the method to extract thin films of $CrNb_3S_6$ from the bulk single crystal. We found the way to obtain several tens-nanometer-thick films as detailed below. Figure 3.1 also shows the procedure of the mechanical exfoliation technique.

1. A $CrNb_3S_6$ single crystal is shaved by a craft knife in order to obtain many flakes of $CrNb_3S_6$ with the fresh surface. Those are then placed on Nitto No. 31 tape (hereafter transparent tape).

2. In order to spread the $CrNb_3S_6$ flakes over the wide area of transparent tapes, one transparent tape with $CrNb_3S_6$ flakes is rubbed into another transparent tape 50 - 100 times.

3. One of the transparent tapes is then rubbed into Nitto SPV363 tape (blue tape) and the same procedure as 2 is repeated for the blue tape. The adhesive strength of the blue tape is weaker than that of the transparent tape.

4. The blue tape is pasted on a SiO_2/Si substrate and rubbed by a cotton swab in order to transfer the $CrNb_3S_6$ thin films onto the substrate.

5. The substrate is dipped in acetone and kept at 60 °C for several ten minutes to remove the adhesive ingredients.

These processes were performed inside a glove box filled with Ar gas of purity 99.9999 % to prevent $CrNb_3S_6$ thin films from being oxidized. An optical microscope image of a typical thin film obtained by this method is shown in Fig. 3.2(a). We also measure the cross section of the thin film using a commercially available atomic force microscope (AFM) as shown in Fig. 3.2(b).

3.1.2 Fabrication of nanostructures

In order to perform transport measurements for exfoliated $CrNb_3S_6$ thin films, we need to attach sub-micrometer electrodes to the films. For this purpose, we have used electron-beam (EB) lithography and subsequent lift-off method. We first prepare a desired nanoscale mask with a polymer membrane, i.e., resist. The resist appropriate for EB lithography is uniformly put on an insulating substrate and is

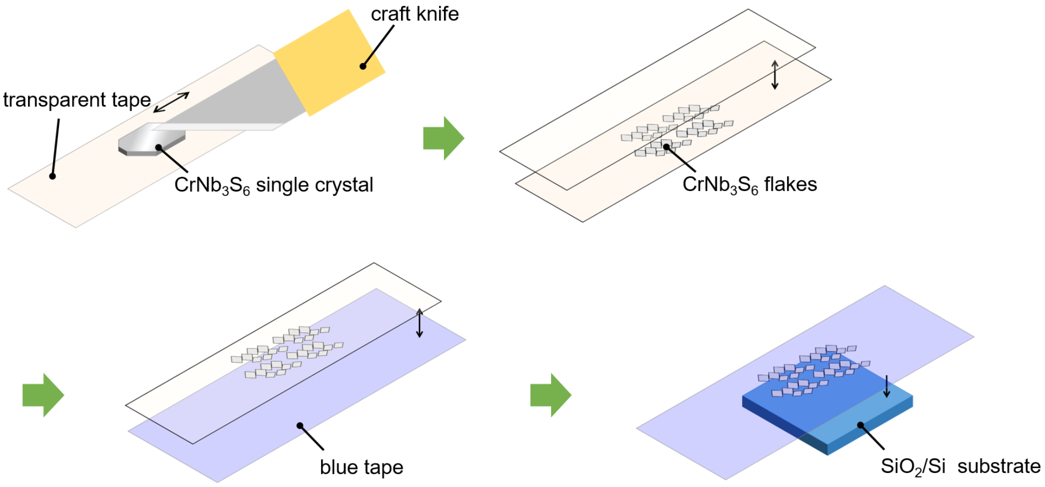

Figure 3.1: Schematic image of the mechanical exfoliation technique.

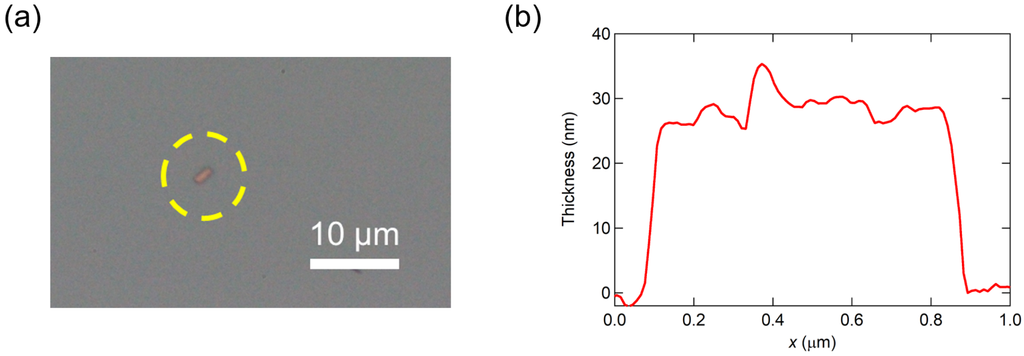

Figure 3.2: (a) Optical microscope image of an exfoliated $CrNb_3S_6$ thin film. (b) Cross section of the $CrNb_3S_6$ thin film measured with an atomic force microscope. The thickness of the film is about 30 nm.

exposed to a necessary quantity of electrons (or current). The resolution of the EB lithography is about 10 nm. In this thesis, we used polymethyl-methacrylate (PMMA, molecular weight 950(A4), Microchem Co. Ltd.) resist for the EB lithography. The thickness of the resist is about 180 nm. In order to attach electrodes to relatively thick $CrNb_3S_6$ films (more than 100 nm), the bilayer resist is needed for the lift-off method. The typical parameters for the EB lithography are listed in Table 3.1. Note that while treating the resist, we have to pay attention to the humidity of the environment because the resist is easily degraded by the humidity. Therefore, we kept the humidity in the laboratory less than 50 % by using a dehumidifier.

A pattern with nanostructures is drawn with EB lithography. To obtain a nanoscale mask, the resist is denatured by dipping the substrate into an appropriate solvent (developer). Then, a metal film is deposited onto the substrate. The desired nanostructures are finally obtained by rinsing away unnecessary parts with acetone. The procedure of the lift-off method is illustrated in Fig. 3.3.

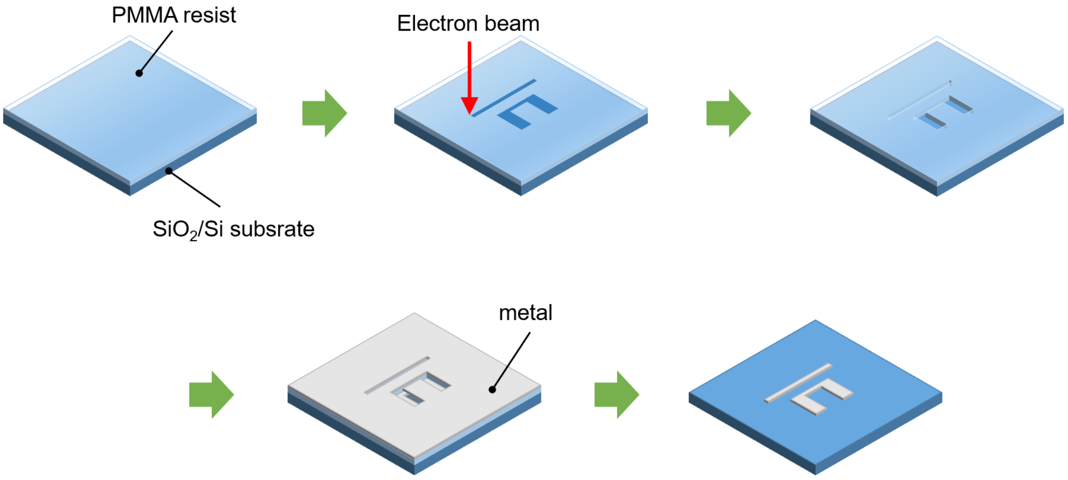

Figure 3.3: Schematic of the lift-off method.

3.1.3 Vapor deposition method

In order to deposit a metal film onto the PMMA mask, we used the vapor deposition method. Several grains of metals are heated and evaporated in a vacuum chamber. The evaporated particles are deposited on the mask placed above the target metal.

Number of layers	Rotational speed (rpm)	Thickness of PMMA resist (nm)	Dose for EB lithography (μC/cm^2)
single	5000	180	840
single	3000	240	860
double	3000	480	1200

Table 3.1: Some parameters for EB lithography using PMMA 950(A4) resist.

In this subsection, we introduce two different evaporation methods, depending on the situation.

Joule heating evaporation

The Joule heating evaporation is one of the easiest methods to evaporate a metal which has a low melting temperature [Fig. 3.4(a)]. A metal boat which has a high melting temperature such as tungsten or molybdenum is heated up by applying a large current. When the melting temperature of the target metal is much lower than that of the boat, the target metal melts and evaporates in a vacuum chamber. There is an advantage that any contaminations from the boat to the target are avoided. Therefore, we used this method for low melting metals such as Au and Cu. On the other hand, it is difficult to handle several kinds of metals with high melting temperatures such as Pt, Ta, and W. Most of magnetic materials cannot be deposited by this method since those make alloys with the boat. In addition, alloys are also not suitable to use this method because the melting temperatures of constituent elements are sometimes quite different and thus it is difficult to keep the same composition ratio as the original target.

Electron-beam evaporation

The EB evaporation is a method to heat a target placed in a crucible by irradiating thermoelectrons to the target [Fig. 3.4(b)]. To heat the target locally, EB is focused on a small part of the target by applying a high voltage and a magnetic field, while the crucible is always kept cool by flowing water from the outside of the vacuum chamber. Contrary to the Joule heating evaporation, magnetic materials and also high melting temperature materials can be deposited by this method. As a crucible, we used a copper hearth liner. We adopted this method for deposition of Ti and Py in this thesis.

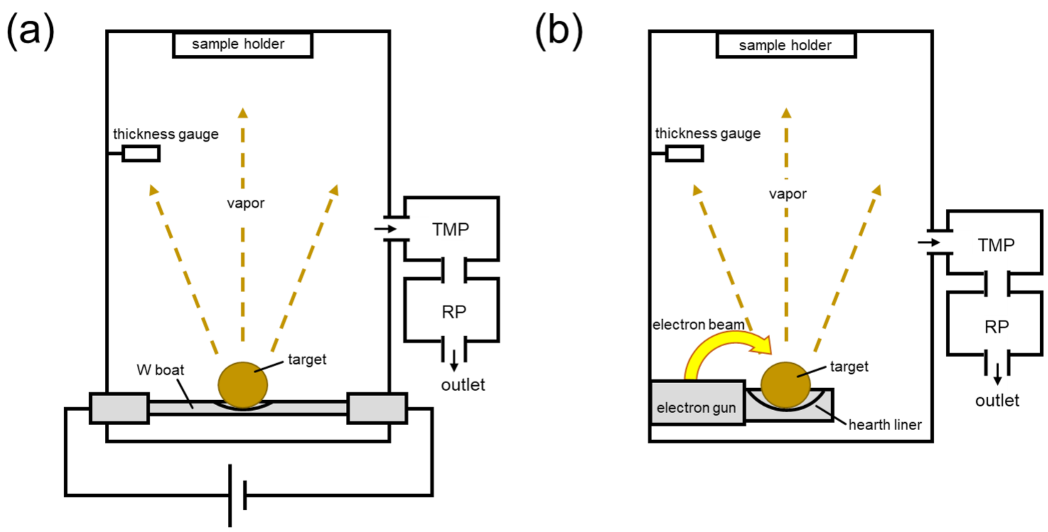

Figure 3.4: Schematic images of two evaporation methods: (a) Joule heating evaporation and (b) Electron-beam evaporation.

3.1.4 Fabrication of nonlocal spin valve structure

Our spin transport device is based on the NLSV structure with a middle wire. This device enables us to obtain the spin Hall angle and the spin diffusion length of the middle wire at the same time. In this subsection, we describe the fabrication procedure of the spin transport device.

Cleaning of SiO_2/Si substrate

In order to fabricate the spin transport device on a thermally-oxidized silicon substrate (i.e., SiO_2/Si substrate), the substrate should be kept clean. In the following, we list the cleaning procedure:

1. A 5×5 mm^2 square SiO_2/Si substrate is dipped in acetone and washed by an ultrasonic bath to remove any contamination on the substrate.

2. It is then transfered to isopropyl-alcohol (IPA) to rinse acetone.

3. The substrate is dried by N_2 gas blower.

4. The substrate is etched by O_2 gas by a power of 5 mA for 30 s.
5. The substrate is dipped in 2-butanone for several seconds.
6. The substrate is dried by N_2 gas blower.

Gold mark

Thin films fabricated by the scotch tape technique are randomly distributed on the substrate. Therefore, we fabricated marks made of gold on the substrate in order to identify the location of the thin films. We fabricated gold marks on a 5 mm square SiO_2/Si substrate. The mark patterns are shown in Fig. 3.5. These mark patterns are made by AutoCAD software. Cross marks are arranged at the interval of 100 μm.

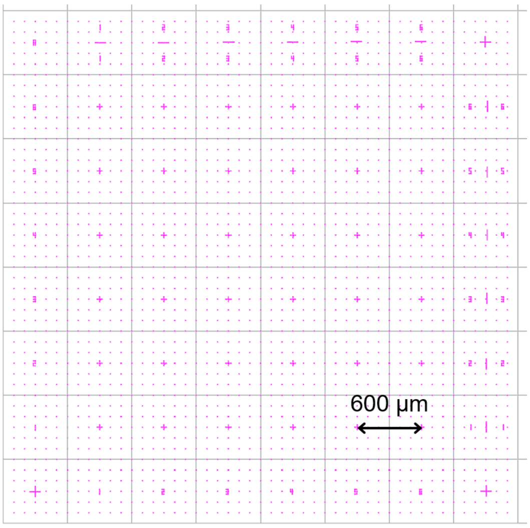

Figure 3.5: AutoCAD drawing of gold marks (pink patterns). The gray square (600×600 μm^2) corresponds to one chip for the EB lithography.

The fabrication procedure of the gold marks is shown below.

1. PMMA 950(A4) resist is coated on the cleaned SiO_2/Si substrate with a speed of 3000 rpm for 60 seconds.
2. The substrate is baked for 10 minutes on a hot plate at 120 °C.

3. The gold mark patterns are drawn by EB lithography with a dose of 800 μC/cm^2 (coarse mode).
4. The patterns are developed with a PMMA developer (IPA: methyl-isobutyl ketone (MIBK) $= 3 : 1$) for 30 seconds and rinsed with IPA for 30 seconds.
5. The substrate is baked for 5 minutes on a hot plate at 100 °C to remove the developer and rinse solution remaining on the substrate.
6. 5 nm thick Ti and 100 nm thick Au are deposited on the substrate by EB evaporation and Joule heating evaporation, respectively.
7. The substrate is dipped in acetone for several hours and the unnecessary metal film is removed by using a dropper.

$CrNb_3S_6$ thin films

1. $CrNb_3S_6$ thin films prepared with the scotch tape technique (see Sec. 3.1.1) are transferred onto the SiO_2/Si substrate with the gold marks.
2. PMMA 950(A4) resist is coated on the substrate with a speed of 5000 rpm for 60 seconds.
3. The substrate is baked for 10 minutes on a hot plate at 120 °C.
4. Slender $CrNb_3S_6$ thin films whose widths are $400 \sim 500$ nm are sought by an optical microscope. For the spin transport device, it is desired to find as many candidates as possible on the same substrate to increase the successful rate.
5. Pictures of the $CrNb_3S_6$ thin films including two gold marks are taken and placed on the AutoCAD sheet by using the two gold marks, in order to identify the location of the thin films on the large surface of the substrate.

Py wires

To inject pure spin current into $CrNb_3S_6$, we used Py ($Ni_{81}Fe_{19}$). When a Py wire is narrow (less than ≈ 500 nm) and thin (several tens nm) enough, it has only single domain. Thus, such a Py wire can be an ideal spin source. In the following, we explain the procedure to prepare the Py nanowire:

1. The Py wire pattern whose width is 100 nm is drawn by the EB lithography with a dose of 840 μC/cm^2 (fine mode).

2. The pattern is developed and baked by the same condition as that for the gold marks.

3. A 30 nm thick Py is deposited by using the EB evaporation.

4. After the substrate is dipped in acetone at 60 °C for 10 minutes, the unnecessary Py film is removed by using a dropper.

100 nm thick Cu bridge and electrodes

Cu has a weak spin-orbit interaction. This enables us to transport pure spin current as far as 1 μm at low temperature. For this purpose, we connected the $CrNb_3S_6$ thin film and the Py wire with a Cu bridge. In the following, we explain the procedure to prepare the Cu nanowire:

1. PMMA 950(A4) resist is coated on the substrate with a speed of 3000 rpm for 60 seconds and then the substrate is baked for 10 minutes on a hot plate at 120 °C.

2. The process is almost the same as that for the Py wire except for the CAD drawing. For example, for a 100 nm wide Cu wire, the width of the Cu bridge has to be designed at 70 nm because of the secondary electrons from the relative thick $CrNb_3S_6$ wire.

3. Before the deposition of Cu, an Ar milling is performed to remove the oxidized layers at surfaces of $CrNb_3S_6$ and Py. The Ar milling is performed under the Ar atmosphere with an Ar flow rate of 0.5 sccm. The parameters of the milling process are Beam voltage = 600 V, Beam current = 12 mA, and Accelerator voltage = 400 V. The milling time is 65 seconds.

4. A 100 nm thick Cu is deposited by using a Joule heating evaporation. During the deposition of Cu, a liquid nitrogen trap is used to reduce the background pressure in the chamber.

5. After the substrate is dipped in acetone for a night, unwanted Cu parts are removed using a dropper at 60 °C.

200 nm thick Cu bridge and electrodes

If the thickness of $CrNb_3S_6$ is thicker than $\approx$ 70 nm, a 100 nm thick Cu is not thick enough to make a bridge. In such a case, we deposited a 200 nm thick Cu film.

1. PMMA 950(A4) resist is coated on the substrate with a speed of 3000 rpm for 60 seconds and the substrate is baked for 10 minutes on a hot plate at 120 °C. To make the PMMA double layer, we repeat the same process twice.
2. The Cu bridge and the electrode patterns are drawn by the EB lithography with a dose of 1200 μC/cm^2.
3. Before the deposition of Cu, an Ar milling is performed to remove the oxidized layers at surfaces of $CrNb_3S_6$ and Py. The Ar milling is performed under the Ar atmosphere with an Ar flow rate of 0.5 sccm. The parameters of the milling process are Beam voltage = 600 V, Beam current = 12 mA, and Accelerator voltage = 400 V. The milling time is 65 seconds.
4. A 200 nm thick Cu is deposited by using a Joule heating evaporation. During the deposition of Cu, a liquid nitrogen trap is used to reduce the background pressure in the chamber.
5. After the substrate is dipped in acetone for a night, unwanted Cu parts are removed using a dropper at 60 °C. When the Cu film cannot be removed completely by the dropper, an ultrasonic bath is applied only for a few seconds with a frequency of 40 kHz not to break the devices.

3.2 Measurement setup

For spin transport measurements at low temperatures, we used a ^{4}He flow cryostat with an electromagnet, as shown in Fig. 3.6. The prepared device is mounted on a chip carrier at the bottom of a dip stick. By pumping the He line with a rotary pump, cold He gas flows in the cryostat and thus the device is cooled down from room temperature to $T = 2.5$ K. The magnetic field can be applied to the device in the range of ± 1.2 T and the electromagnet can rotate around the cryostat. The electrical measurements are performed by the standard lock-in technique, as shown in Fig. 3.7.

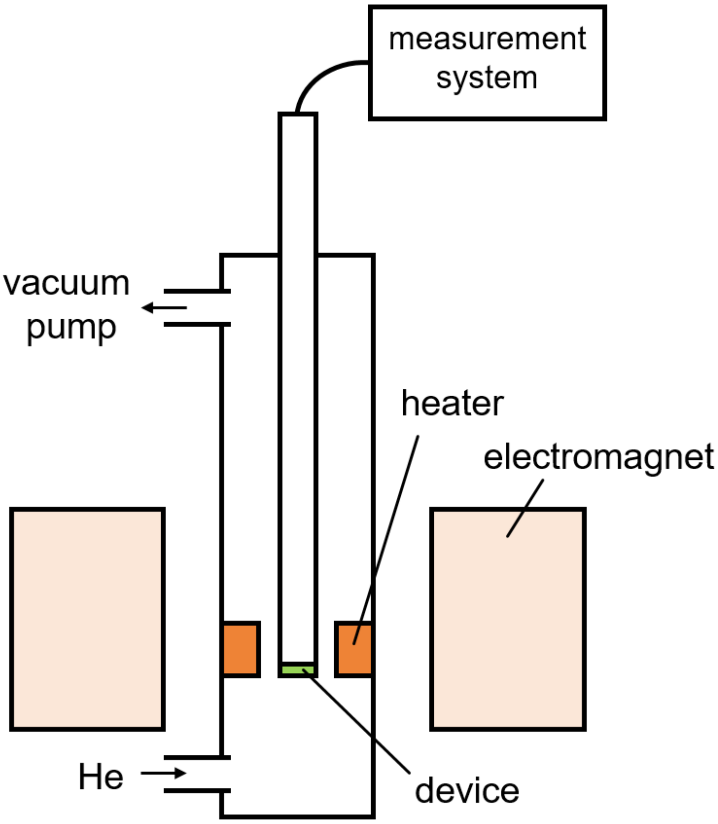

Figure 3.6: Schematic image of our cryostat.

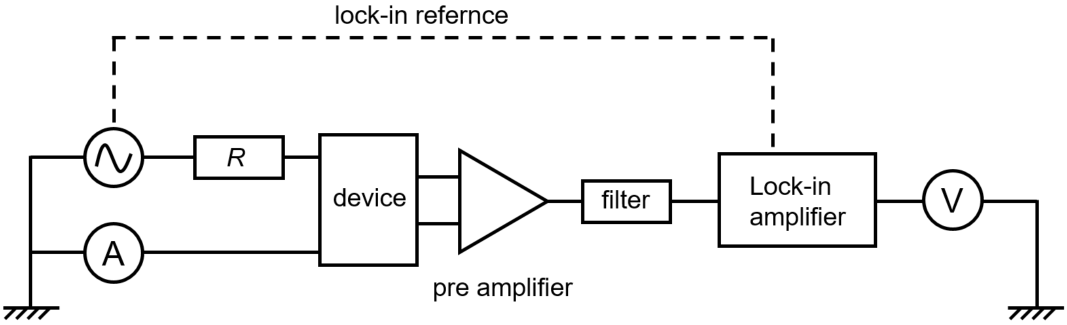

Figure 3.7: The measurement circuit for the standard lock-in method.

Chapter 4

Experimental results

4.1 Electrical properties of $CrNb_3S_6$ thin films

Before conducting spin transport experiments with $CrNb_3S_6$ thin films, we checked some fundamental properties of the films in order to confirm if the thin film devices have as a good quality as bulk crystals.

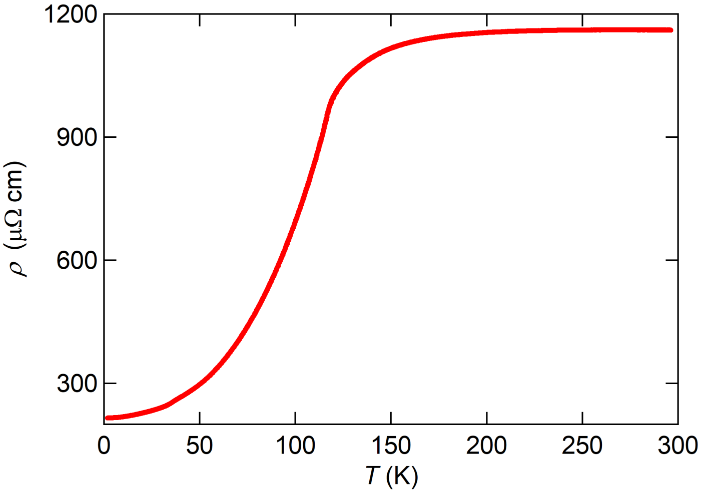

Figure 4.1: The temperature T dependence of ρ of a 80 nm thick $CrNb_3S_6$ film.

Figure 4.1 shows the temperature dependence of the resistivity ρ of a 80 nm thick $CrNb_3S_6$ film fabricated by the scotch tape technique. The resistivity suddenly

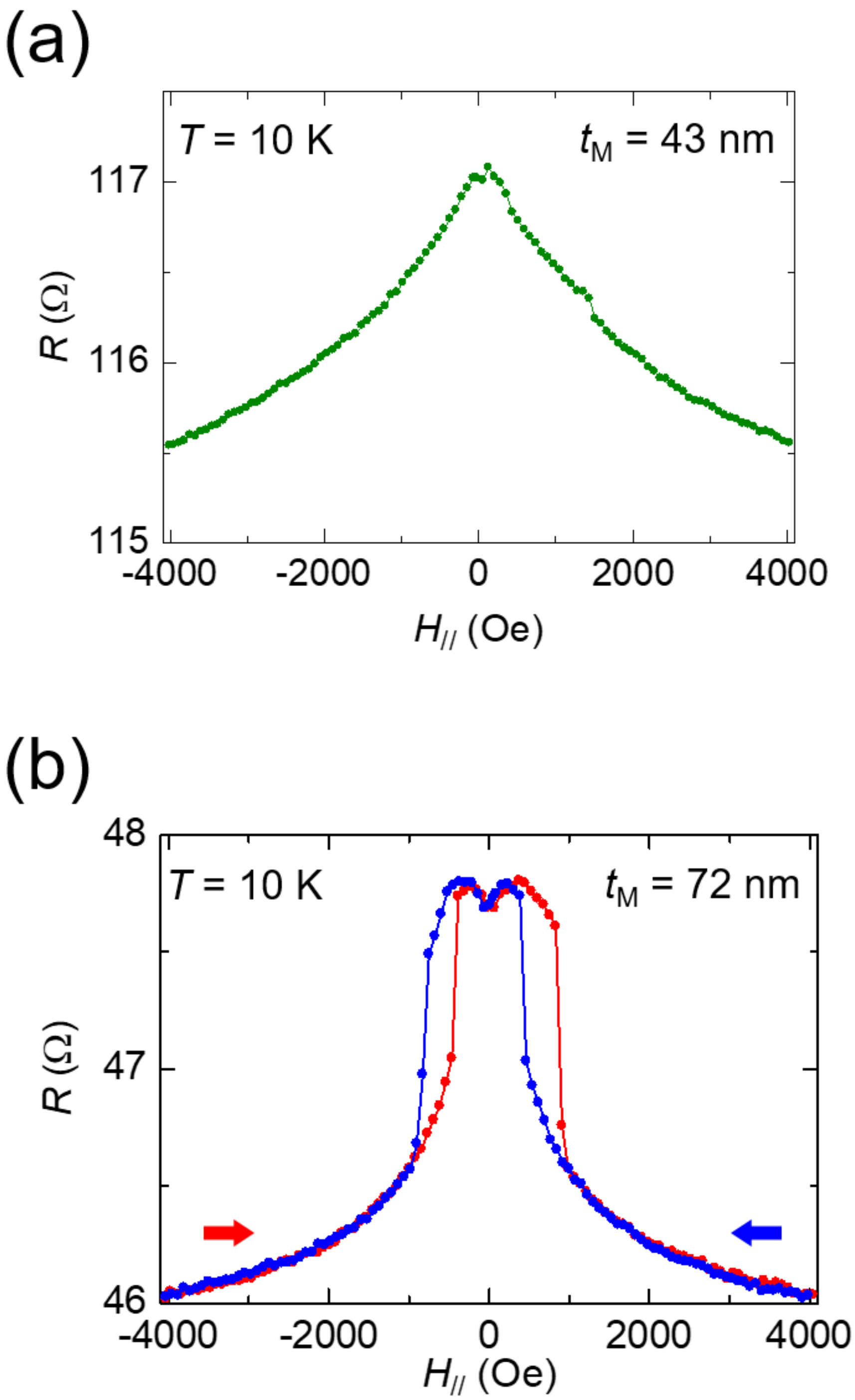

Figure 4.2: Magnetoresistances of (a) 43 nm thick and (b) 72 nm thick $CrNb_3S_6$ films measured at 10 K.

decreases at around $T_\mathrm{C} \approx 130$ K below which CrNb$_3$S$_6$ transitions from a paramagnet to a chiral helimagnet. This behavior is consistent to that of bulk single crystals.

Next, we measured magnetoresistance of the thin film. As mentioned in Chapter 1, the helical axis is perpendicular to the basal plane. Thus, as the magnetic field is applied along the in-plane (i.e., perpendicular to the *c*-axis of CrNb$_3$S$_6$ film), the helix is unwound and the magnetization becomes ferromagnetic above 2000 Oe. When a node of the helix is pushed away from the thin film by applying the magnetic field, a sudden jump is observed in the magnetoresistance. Inversely, when a node of the helix is formed by decreasing the magnetic field, a similar sudden jump shows up but there is a magnetic hysteresis between the two processes. Figures 4.2(a) and 4.2(b) show magnetoresistances of CrNb$_3$S$_6$ films with the thicknesses of 43 nm and 72 nm, respectively. For the 43 nm thick device, the magnetoresistance continuously decreases with increasing the magnetic field. On the other hand, for the 72 nm thick device, a sudden jump and a magnetic hysteresis were observed in the magnetoresistance. The difference originates from the relation between the thickness and one helical pitch. As explained in Chapter 1, one helical pitch at $H = 0$ is $L(0) = 48$ nm. Therefore, the former and latter devices have less than and more than one helical pitch, respectively. We can identify the number of helical pitches included in the film from the magnetoresistance measurement.

4.2 Spin transport measurements in CrNb$_3$S$_6$ thin films

In order to investigate spin transport properties in a chiral magnetic system, we fabricated NLSV devices with a CrNb$_3$S$_6$ thin film. The typical device is shown in Fig. 4.3. The device consists of two ferromagnetic Py wires and a CrNb$_3$S$_6$ film, which are bridged by a Cu wire. Using the NLSV device shown in Fig. 4.3, three different measurements can be performed to investigate spin transport properties of CrNb$_3$S$_6$ thin film. In the following subsection, the three measurements are detailed.

4.2.1 Inverse spin Hall effect in CrNb$_3$S$_6$

First, we show some results on the ISHE in CrNb$_3$S$_6$, obtained with two voltage probes V_ISHE (see Fig. 4.3). A schematic drawing of the ISHE measurement is shown in Fig. 4.4. By flowing an electric current I from the left Py wire to the Cu wire, spin accumulation is generated at the interface between Py and Cu. In the nonmagnetic Cu wire, the spin accumulation diffuses and a pure spin current consequently flows.

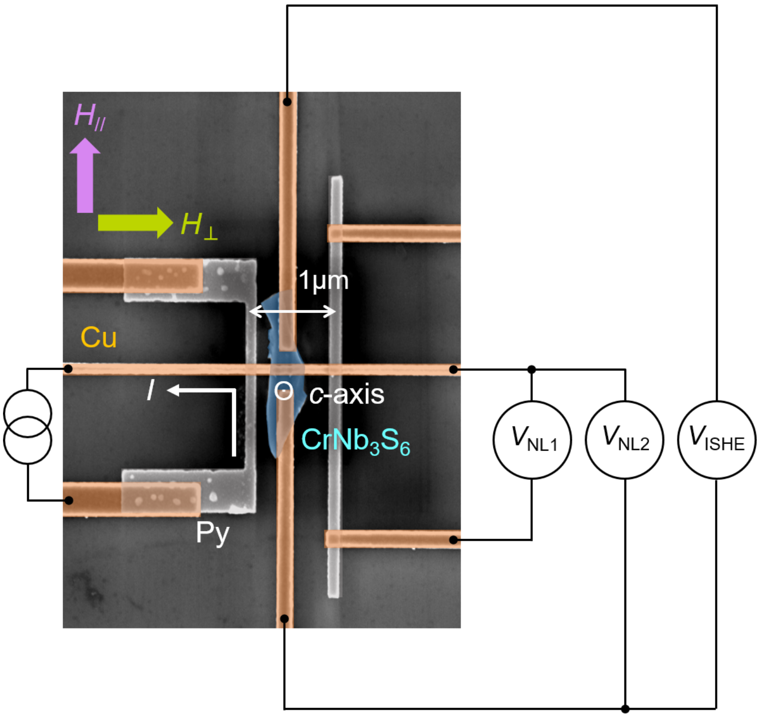

Figure 4.3: Scanning electron micrography (SEM) image of the NLSV device with an insertion of $CrNb_3S_6$ film. Using this device, three different spin transport measurements (i.e., V_{NL1}, V_{NL2} and V_{ISHE}) can be performed.

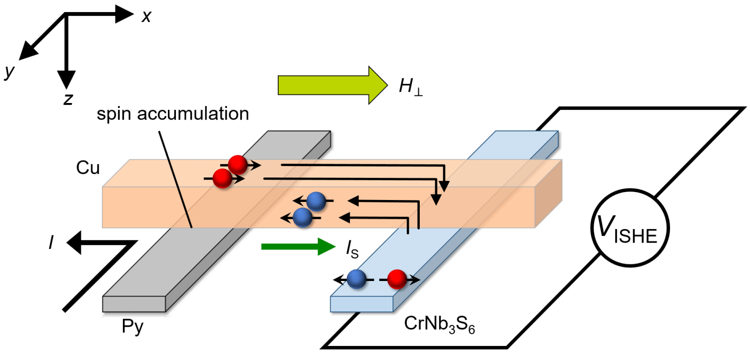

Figure 4.4: Schematic image of the ISHE measurement in $CrNb_3S_6$.

When a strong spin-orbit material (in the present case, CrNb$_3$S$_6$) is placed within the spin diffusion length of Cu ($\sim 1\ \mu$m at low temperatures), a part of the pure spin current is injected into the spin-orbit material. When the magnetization of the Py wire is fully polarized along the Cu wire ($|H_\perp| > 3000$ Oe), a spin-to-charge conversion [see Eq. (2.4)] is generated in the CrNb$_3$S$_6$ thin film.

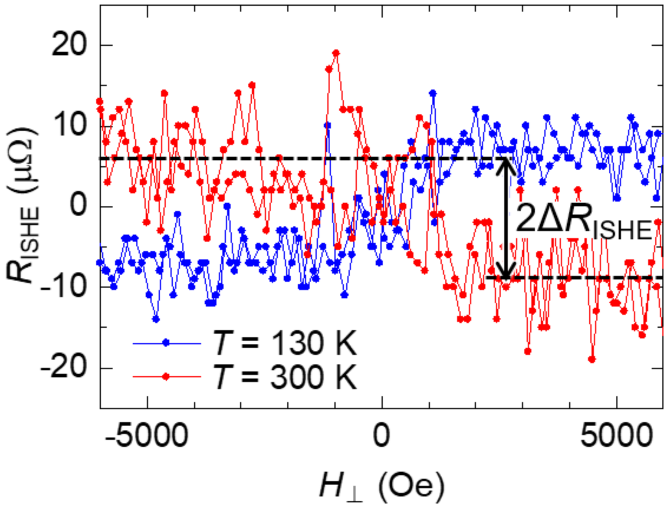

Figure 4.5: R_{ISHE} of 72 nm thick CrNb$_3$S$_6$ device measured at $T = 130$ K and 300 K. ΔR_{ISHE} is defined in the figure.

In Fig 4.5, we show ISHE resistance R_{ISHE} of the 72 nm thick CrNb$_3$S$_6$ device measured at $T = 130$ K and 300 K. R_{ISHE} is defined as a detected voltage drop V_{ISHE} in the CrNb$_3$S$_6$ film divided by the current I injected from the left Py wire to the Cu wire. When $|H_\perp| > 3000$ Oe, R_{ISHE} is saturated because the magnetization of Py wire is fully polarized along the Cu wire. This situation meets the cross product in Eq. (2.4). At room temperature, a clear negative ISHE resistance [$2\Delta R_{\mathrm{ISHE}} \equiv R_{\mathrm{ISHE}}(H_\perp > 3000\ \mathrm{Oe}) - \mathrm{R_{ISHE}(H_\perp} < -3000\ \mathrm{Oe})$] is observed. This is consistent with the ISHE resistance of pure Nb. However, the sign of the ISHE resistance observed at $T_{\mathrm{C}} = 130$ K is opposite to that at room temperature (in other words, positive). We show the temperature dependence of the ISHE resistance ΔR_{ISHE} and also the spin Hall angle $\alpha_{\mathrm{H}}^{\mathrm{ISHE}}$ (see the following discussion) for CrNb$_3$S$_6$ with two different thicknesses in Figs. 4.6(a) and 4.6(b), respectively. For both devices, ΔR_{ISHE} and $\alpha_{\mathrm{H}}^{\mathrm{ISHE}}$ take the maximum at $T_{\mathrm{C}} = 130$ K. The sign of ΔR_{ISHE} and $\alpha_{\mathrm{H}}^{\mathrm{ISHE}}$ of the 43 nm

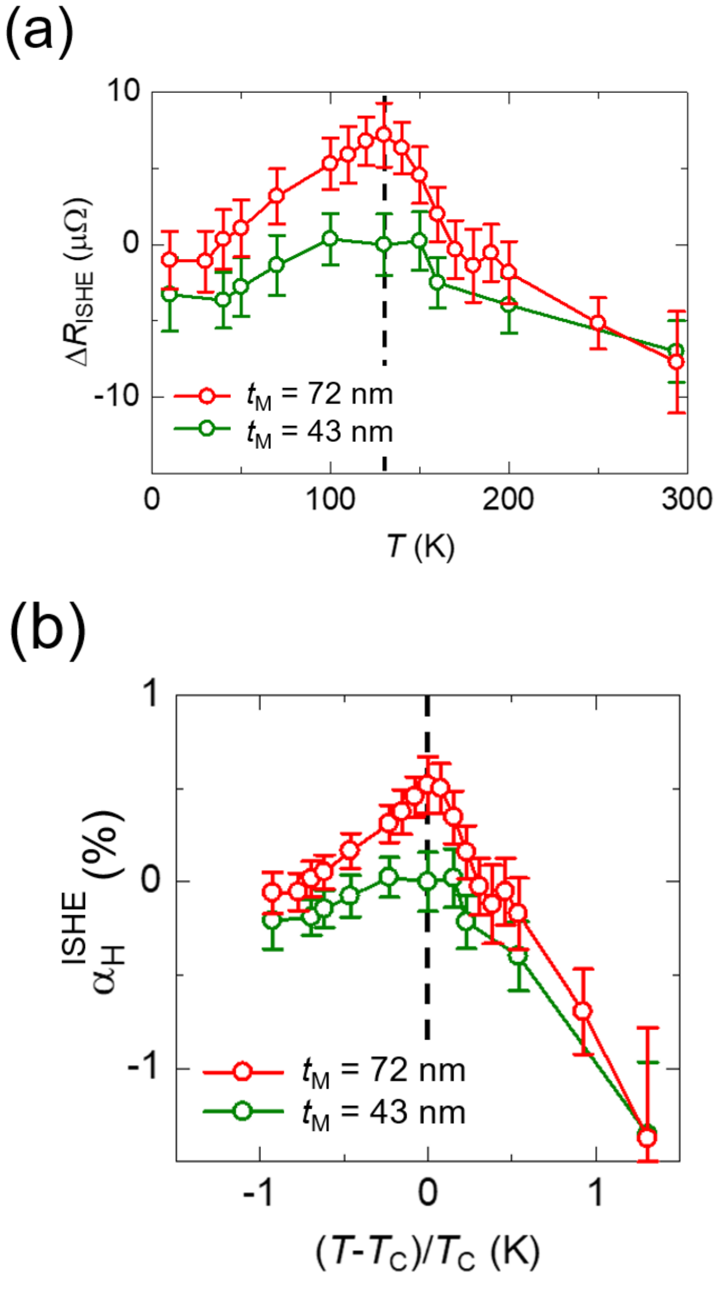

Figure 4.6: (a) Temperature dependence of $\Delta \mathrm{R}_{\mathrm{ISHE}}$ for the t = 43 nm and 72 nm thick devices. For both devices, ΔR_{ISHE} takes the maximum at $T_{\mathrm{C}} = 130$ K. The sign of ΔR_{ISHE} of the 43 nm thick $\mathrm{CrNb_3S_6}$ device is always negative, while ΔR_{ISHE} of the 72 nm thick device changes the sign in the vicinity of T_{C}. (b) The spin Hall angles $\alpha_{\mathrm{H}}^{\mathrm{ISHE}}$ of the 43 nm and 72 nm thick $\mathrm{CrNb_3S_6}$ devices as a function of the reduced temperature $(T - T_{\mathrm{C}})/T_{\mathrm{C}}$.

thick $CrNb_3S_6$ device is always negative, while ΔR_{ISHE} of the 72 nm thick $CrNb_3S_6$ device changes the sign near T_{C}. These results indicate that (1) the ISHE at room temperature is generated due to the spin-orbit interaction of Nb atoms and (2) spin fluctuations are enhanced near T_{C} and the sign of the ISHE consequently reverses for the 72 nm thick $CrNb_3S_6$ device, as in the case of the ISHE in spin glasses.

4.2.2 Nonlocal spin valve measurements in $CrNb_3S_6$

Spin diffusion length of $CrNb_3S_6$

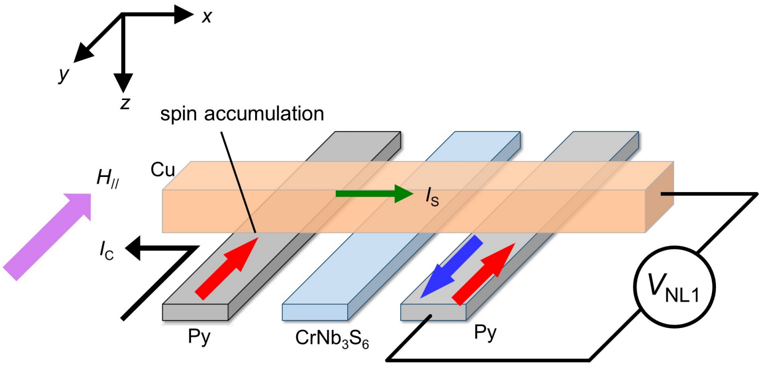

Figure 4.7: Schematic image of NLSV measurement with an insertion of $CrNb_3S_6$ film.

In order to evaluate the spin diffusion length $\lambda_{\mathrm{CrNb_3S_6}}$ of $CrNb_3S_6$, we performed NLSV measurements with and without the $CrNb_3S_6$ thin film. A schematic image of the NLSV measurement is shown in Fig. 4.7. As mentioned above, the lateral spin valve structure is one of the methods to generate pure spin current. By flowing an electric current I from the left Py wires to the Cu wire, the spin accumulation generated at the interface between Py and Cu diffuses and a pure spin current flows in the Cu wire. When another Py wire is placed within the spin diffusion length of Cu, the nonlocal voltage V_{NL1} [see Fig. 4.3] that depends on the relative magnetization direction of the two Py wires (i.e., parallel or antiparallel) can be detected. We used two NLSV devices, i.e., with and without the $CrNb_3S_6$ film.

The typical NLSV signals are shown in Fig. 4.8. Apparently, when the $CrNb_3S_6$ film is inserted in between the two Py wires, the NLSV signal ΔR_{S} is reduced compared to that without the $CrNb_3S_6$ film. This result indicates that a part of the

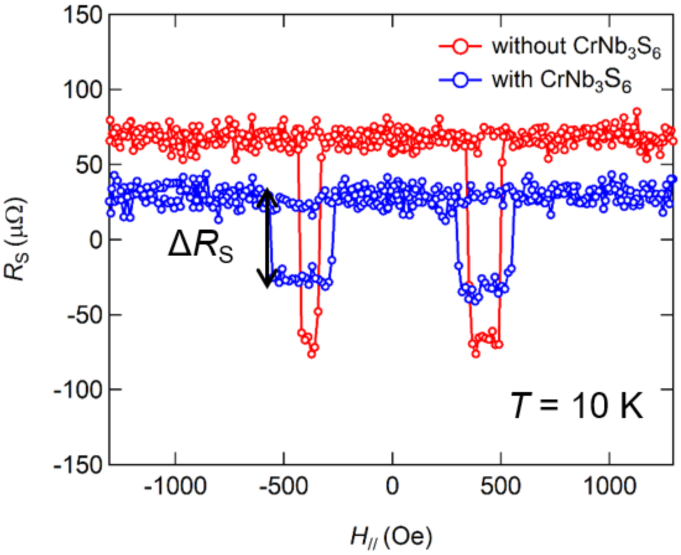

Figure 4.8: NLSV signal R_S with a 30 nm thick $CrNb_3S_6$ film measured at $T = 10$ K. For reference, we also measured R_S without $CrNb_3S_6$ at the same time.

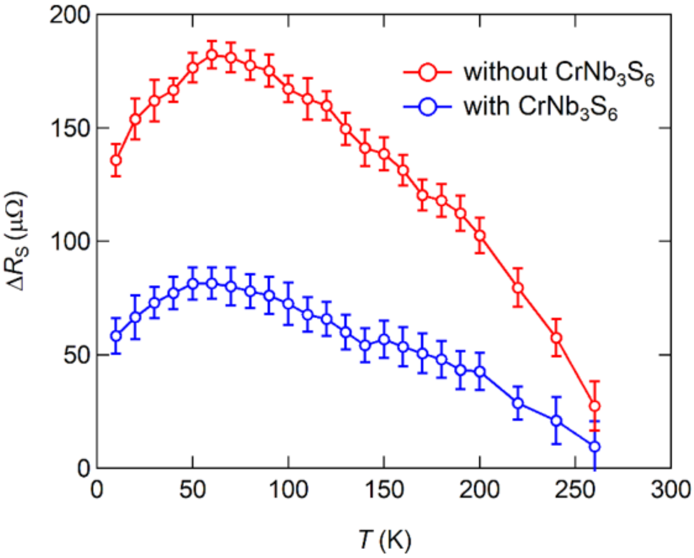

Figure 4.9: ΔR_S with and without $CrNb_3S_6$ as a function of T.

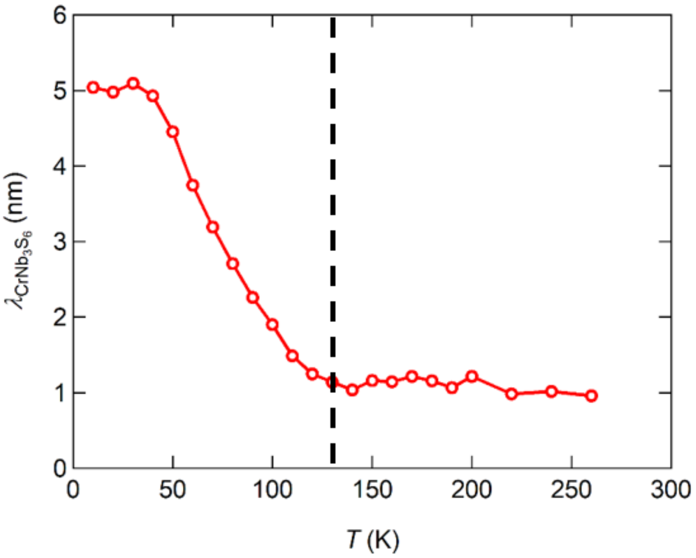

Figure 4.10: The spin diffusion length of $CrNb_3S_6$ as a function of temperature.

pure spin current is absorbed into the $CrNb_3S_6$ film via the Cu wire. We show the temperature dependence of ΔR_S for with and without the $CrNb_3S_6$ film in Fig. 4.9. From the reduction rate $\Delta R_S^{\text{with}}/\Delta R_S^{\text{without}}$, the spin diffusion length $\lambda_{CrNb_3S_6}$ can be obtained using Eq. (2.69). Figure 4.10 shows $\lambda_{CrNb_3S_6}$ as a function of temperature. The spin diffusion length of $CrNb_3S_6$ is about 5 nm at low temperature, which is consistent with that of pure Nb. On the other hand, it suddenly decreases above $T = 50$ K and is saturated at 1 nm above T_C. $\lambda_{CrNb_3S_6}(T)$ is almost inversely proportional to the resistivity $\rho(T)$ shown in Fig. 4.1. These results show that the Elliott-Yafet mechanism is dominant in this material, as mentioned in Sec. 2.6. We also calculated the spin Hall angle α_H^{ISHE} from $\lambda_{CrNb_3S_6}$ using Eqs. (2.73) and (2.74). In order to estimate α_H^{ISHE}, it is necessary to evaluate the shunting factor of the interface between Cu and $CrNb_3S_6$. We implemented three dimensional simulations based on the finite element treatment and estimated the shunting factor x to be about 0.2. The spin Hall angles α_H^{ISHE} of the 43 nm and 72 nm thick $CrNb_3S_6$ films as a function of the reduced temperature $(T - T_C)/T_C$ is shown in Fig. 4.6(b). The general trend is basically the same as the temperature dependence of ΔR_{ISHE}.

Surface magnetization and spin polarization of $CrNb_3S_6$

Below T_C, $CrNb_3S_6$ becomes a chiral helimagnet with a finite magnetization. Therefore, it should work as a magnetic detector (like Py wire) for pure spin current. In order to test this assumption, we performed a NLSV measurement with V_{NL2} in Fig. 4.3. From this measurement, we can evaluate "surface" spin polarization of $CrNb_3S_6$. Since the spin diffusion length of $CrNb_3S_6$, $\lambda_{CrNb_3S_6}$, is about 5 nm, the estimated spin polarization should be different from that of bulk $CrNb_3S_6$ and much more sensitive to the surface spin polarization. Figure 4.11 shows the schematic image of the NLSV measurement with $CrNb_3S_6$. Depending on the surface magnetization of $CrNb_3S_6$, nonlocal voltage V_{NL2} changes the sign, as in the case of the standard nonlocal spin valve measurement using two ferromagnetic wires.

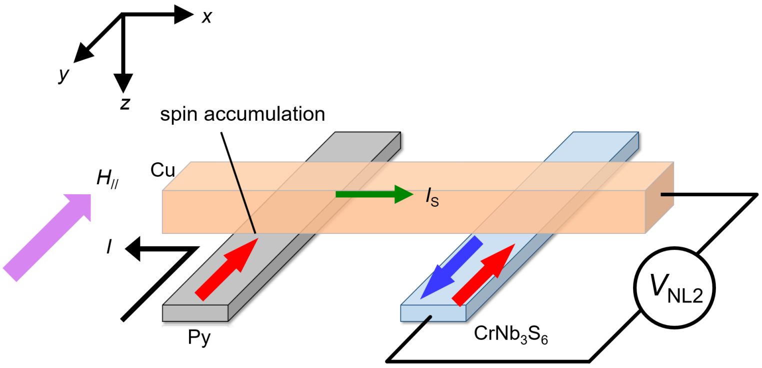

Figure 4.11: Schematic image of the NLSV measurement using $CrNb_3S_6$ as a detector.

Figures 4.12(a) and 4.12(b) show NLSV signals $R_S \equiv V_{NL2}/I$ at $T = 50$ K using 45 nm and 72 nm thick $CrNb_3S_6$ films, respectively. Clear R_S jumps due to the magnetization inversions are observed within the field range of $\approx \pm300$ Oe in both devices. In addition, R_S is saturated above $H_{//} = 2000$ Oe, where $CrNb_3S_6$ becomes a forced ferromagnet. In the 72 nm thick film, additional jumps in R_S were also observed in the field range of $\pm(500 \sim 1000)$ Oe [see the vertical arrows in Fig. 4.12(b)]. These jumps are related to the fact that the node of the helix is pushed away from the film by applying the magnetic field.

In order to focus on the small magnetic field range, we swept the magnetic field within ±400 Oe and measured NLSV signals R_S of the 45 nm and 72 nm thick $CrNb_3S_6$ devices, as shown in Figs. 4.13(a) and 4.13(b). For both cases, R_S jumps

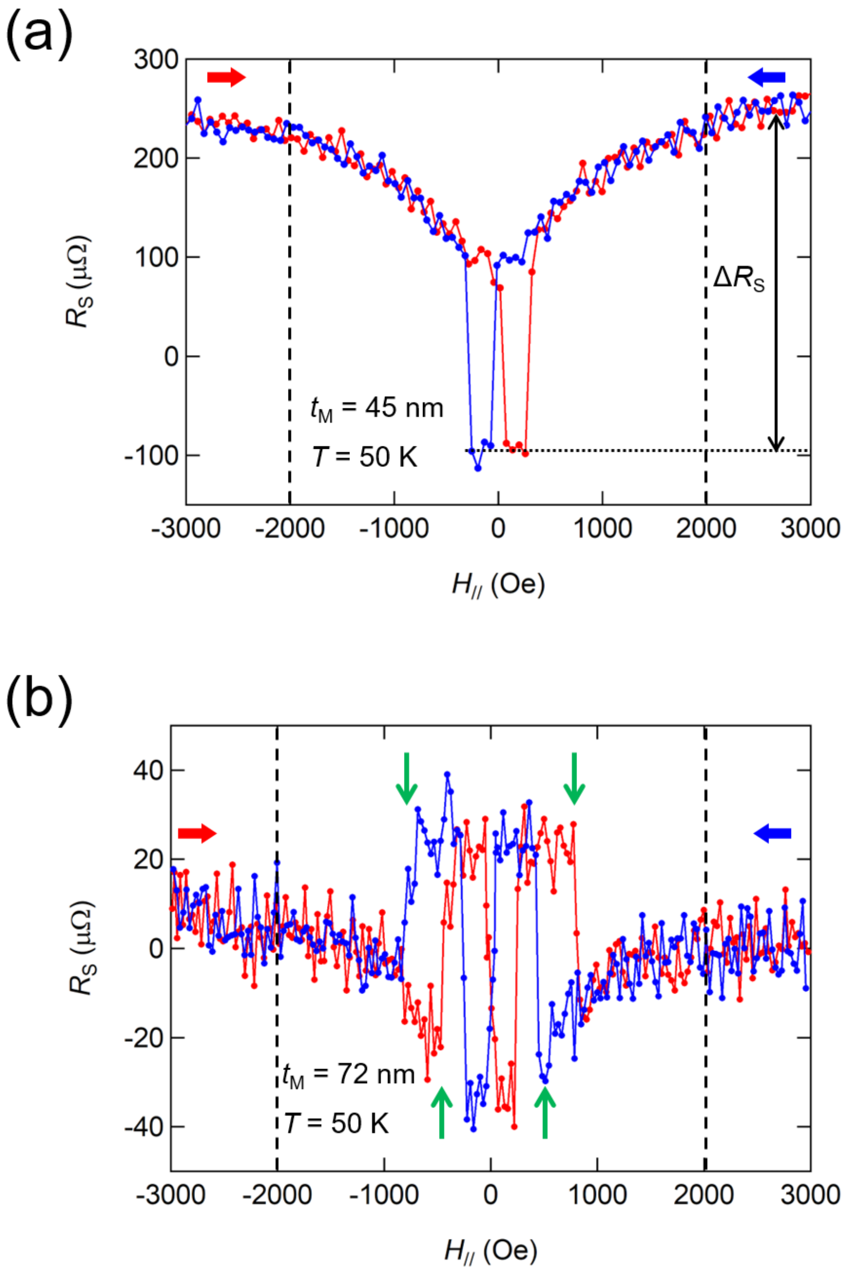

Figure 4.12: (a) NLSV signal R_S at $T = 50$ K using 45 nm thick $CrNb_3S_6$ film. R_S is saturated above $H_{//} = 2000$ Oe, where $CrNb_3S_6$ becomes a forced ferromagnet. (b) NLSV signal R_S at $T = 50$ K using 72 nm thick $CrNb_3S_6$ film. Sudden jumps were observed at around $\pm(500 \sim 1000)$ Oe. This behavior is consistent with Fig. 4.2(b).

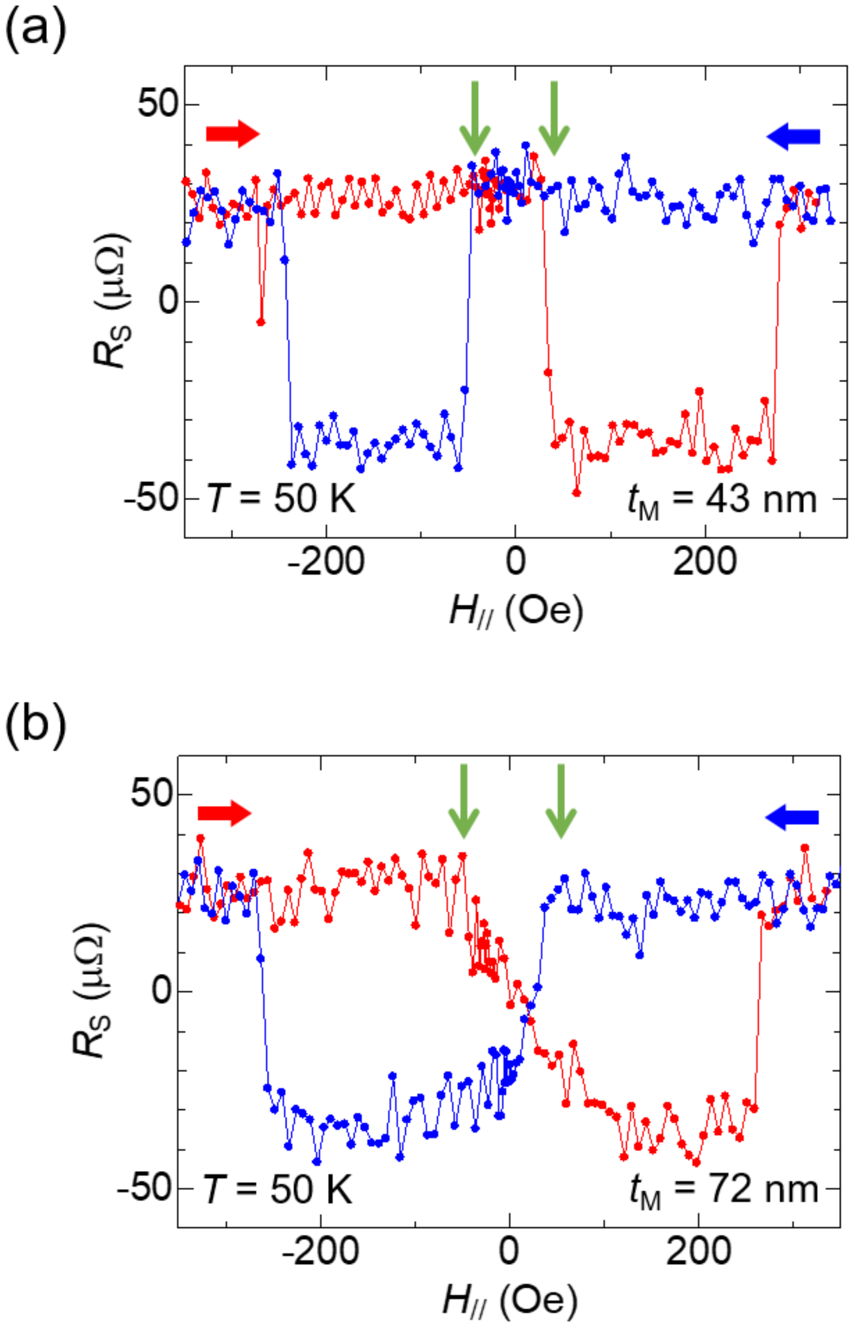

Figure 4.13: NLSV signals R_{S} at T = 50 K with (a) 43 nm and (b) 72 nm thick CrNb$_3$S$_6$ devices, respectively. When t_{M} is smaller than $L(0)$, switching of magnetization of CrNb$_3$S$_6$ takes place at around 50 Oe [see green arrows in (a)]. For $t_{\mathrm{M}} > L(0)$, on the other hand, the magnetization starts to be twisted even in the negative (positive) magnetic field [see green arrows in (b)].

were detected at ±250 Oe. These jumps are related to the magnetization switching of the Py wire [see also Fig. 4.8]. In other words, R_S jumps at ±50 Oe originate from the magnetization change of $CrNb_3S_6$ thin films. When the thickness t_M of $CrNb_3S_6$ is smaller than one chiral pitch $L(0)$, sudden R_S jumps are clearly observed at around ±50 Oe [see Fig. 4.13(a)]. This result clearly indicates that sudden magnetization switching of $CrNb_3S_6$ takes place at a tiny field of 50 Oe. This also suggests that the surface magnetization of $CrNb_3S_6$ is a fixed end when $t_M < L(0)$ [see Fig. 4.14].

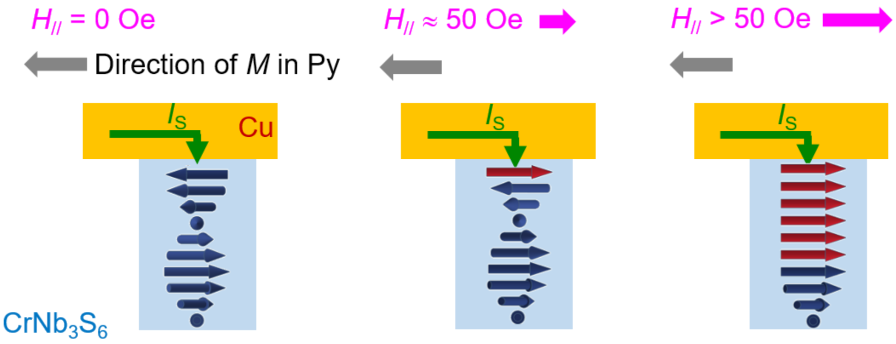

Figure 4.14: Schematic images of surface magnetizations of $CrNb_3S_6$ thinner than $L(0)$ depending on $H_{//}$.

For $t_M > L(0)$, on the other hand, the magnetization starts to be twisted even in the same direction of the magnetic field as shown in the schematic drawing in Fig. 4.15. Such a NLSV signal is typical of the chiral magnetic system where the magnetization has a spiral structure. All these results suggest that the surface magnetization of $CrNb_3S_6$ depends on the length of the magnetic helix.

We then estimated the surface spin polarization of $CrNb_3S_6$ thin films. As mentioned above, when $|H_{//}| > 2000$ Oe, $CrNb_3S_6$ becomes a forced ferromagnet. Therefore, we regarded $CrNb_3S_6$ as a ferromagnetic detector and adopted the 1D spin diffusion model. Using Eq. (2.70), we can estimate the surface spin polarization $p_{CrNb_3S_6}$. When t_M is thinner than $L(0)$, it is natural to define ΔR_S, as shown in Fig. 4.12(a). $p_{CrNb_3S_6}$ of 45 nm thick $CrNb_3S_6$ film at 50 K is estimated to be 1.7%. This value is about 10 times smaller than that of Py (∼ 20%). For $t_M > L(0)$, on the other hand, this definition would not be valid because the spin signal R_S in a small field range (±300 Oe) is larger than that above $H_{//} = 2000$ Oe [see Fig. 4.12(b)] where the magnetization of $CrNb_3S_6$ is fully polarized and the largest spin signal is expected. At the moment, it is not clear whether the spin polarization (∼ 1.7%)

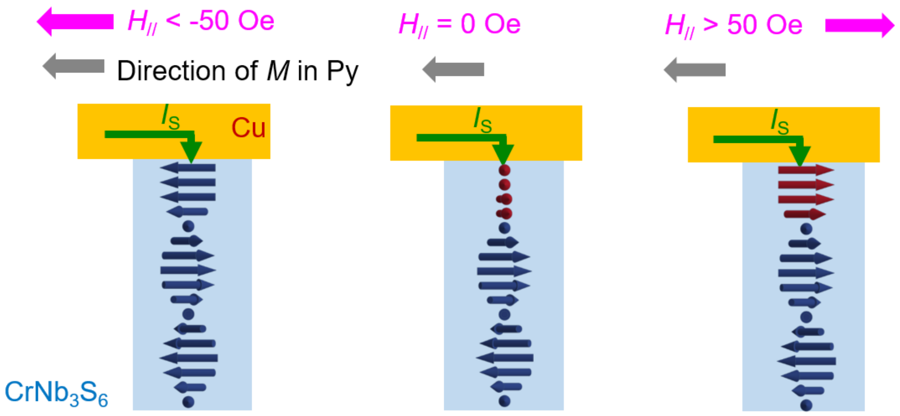

Figure 4.15: Schematic images of surface magnetizations of $CrNb_3S_6$ thicker than $L(0)$ depending on $H_{//}$.

estimated from the above simple model is reasonable. In order to interpret all the spin signals, more detailed theoretical studies are necessary.

4.3 Reproducibility of the results

In order to confirm the reproducibility of the above results, we have performed the same measurements as discussed in Secs. 4.1 and 4.2 using several different devices. Table 4.1 shows all the devices used for the spin transport measurements. The film thicknesses t_{M} in Devices 1-5 were measured by using the AFM. For Devices 6 and 7, the $CrNb_3S_6$ films were too small to measure the thickness by the AFM. Therefore, we estimated t_{M} of Devices 6 and 7 from the electrical resistances (see following discussion). The film widths w_{M} were obtained from the SEM images of the devices. The resistances of the $CrNb_3S_6$ thin films were obtained from the two-terminal measurements because the films were too small to attach four electrodes. The resistivities ρ of the $CrNb_3S_6$ films for Devices 1-5 were estimated by subtracting the resistance of the constantan wire (the measurement line) and by ignoring the resistance of Cu electrodes as well as the contact resistance between Cu and $CrNb_3S_6$. ρ at room temperature (RT) and low temperature (LT, below 10 K) are shown in Table 4.1. These values are similar to the resistivity of the 80 nm thick film measured by the four-terminal measurement as shown in Fig. 4.1. Namely, the resistivity is almost independent of the film thickness. Therefore, we assumed that the $CrNb_3S_6$

films in Devices 6 and 7 have the same resistivities as the 80 nm thick film. Based on this assumption, we estimated the thicknesses of the films in Devices 6 and 7.

device number	t_{M} (nm)	w_{M} (nm)	$\alpha_{\mathrm{H}}^{\mathrm{ISHE}}$ at RT (%)	$\lambda_{\mathrm{CrNb_3S_6}}$ at LT (nm)	ρ at RT ($\mu\Omega$ cm)	ρ at LT ($\mu\Omega$ cm)
1	43	810	-1.4		2200	820
2	45	360	-0.7		1500	380
3	47	510	-0.5		2500	1100
4	72	620	-1.4		1920	420
5	73	630	-1.2		1540	410
6	30	400	-1.9	5		
7	20	400		11		

Table 4.1: The list of all the devices used for the spin transport measurements.

Figure 4.16(a) shows the spin Hall angle $\alpha_{\mathrm{H}}^{\mathrm{ISHE}}$ as a function of the reduced temperature for Devices 1, 2, 3, and 6 where the thickness of the $\mathrm{CrNb_3S_6}$ is less than $L(0)$. Device 1 is the same as shown in Fig. 4.6. All the devices show the same tendency: $\alpha_{\mathrm{H}}^{\mathrm{ISHE}}$ is always negative and has a broad peak at T_{C}.

We have also checked the reproducibility of $\alpha_{\mathrm{H}}^{\mathrm{ISHE}}$ for devices whose thicknesses are thicker than $L(0)$, as shown in Fig. 4.16(b). Device 4 is the same as shown in Fig. 4.6. Device 5 (t_{M} =73 nm) follows the same temperature dependence as Device 4, including the sign change at around T_{C}.

Next, we checked the reproducibility for the NLSV measurement. Device 6 is the 30 nm thick device shown in Figs. 4.8, 4.9, and 4.10. Figure 4.17 shows the temperature dependence of ΔR_{S} of Device 7 (t_{M} = 20 nm). For the reference, we plot ΔR_{S} without $\mathrm{CrNb_3S_6}$ prepared at the same time as Device 7. Overall, ΔR_{S} in Fig. 4.17 is smaller probably due to the less transparent interface between F and N as well as M and N. Nevertheless, the general trend is basically similar to that of Device 6 shown in Fig. 4.9. From the result in Fig. 4.17, the spin diffusion length can be calculated. The temperature dependence of $\lambda_{\mathrm{CrNb_3S_6}}$ for Devices 6 and 7 is shown in Fig. 4.18. The large enhancement of $\lambda_{\mathrm{CrNb_3S_6}}$ below T_{C} and saturation above T_{C} have been well reproduced.

Furthermore, the unique NLSV signals, where $\mathrm{CrNb_3S_6}$ is used as a pure spin current detector, have been reproduced in different devices. Figures 4.19(a) and 4.19(b) show the NLSV signals measured with Device 3 ($t_{\mathrm{M}} < L(0)$) and Device 6 ($t_{\mathrm{M}} > L(0)$), respectively. For both devices, the magnetization switchings of the $\mathrm{CrNb_3S_6}$ thin films occur at almost the same magnetic fields as in Fig. 4.13.

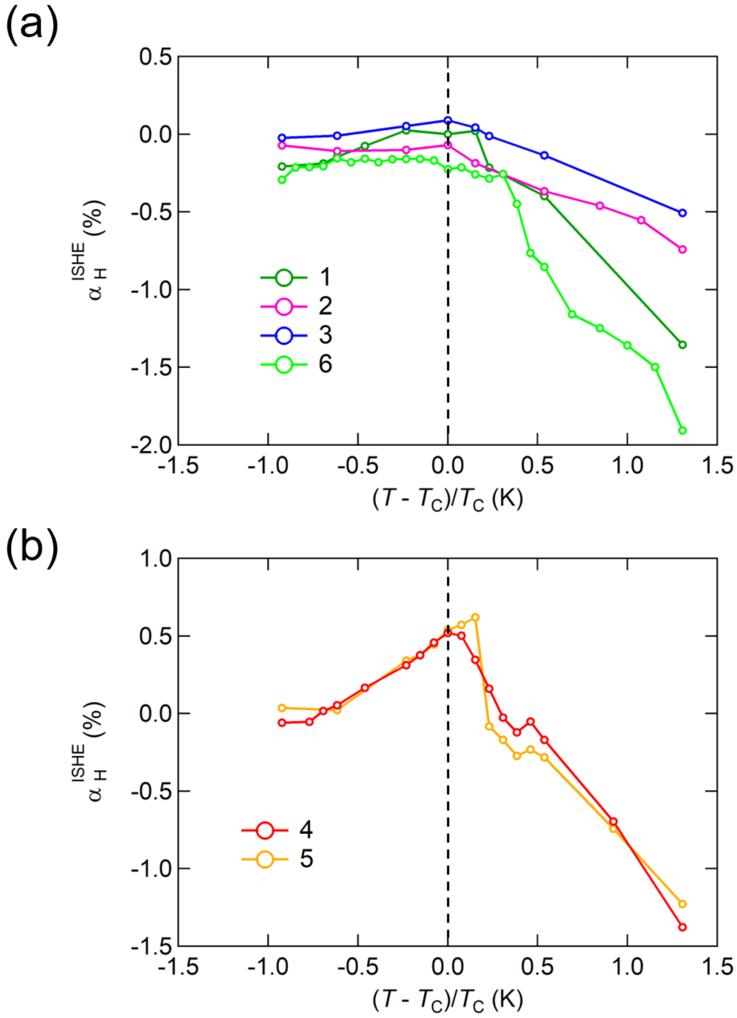

Figure 4.16: The spin Hall angle $\alpha_{\mathrm{H}}^{\mathrm{ISHE}}$ as a function of T for several different devices with thicknesses (a) $t_{\mathrm{M}} < L(0)$ and (b) $t_{\mathrm{M}} > L(0)$.

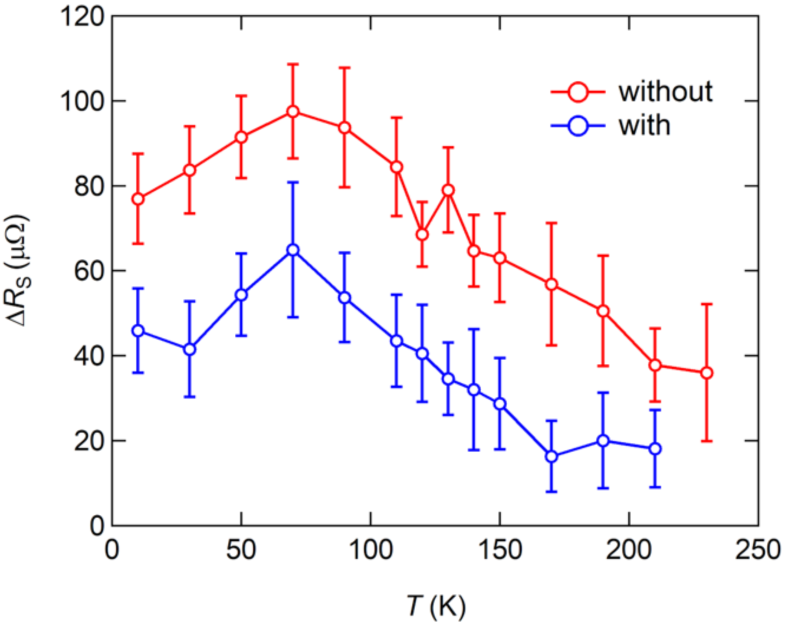

Figure 4.17: ΔR_S with and without $\mathrm{CrNb_3S_6}$ measured with Device 7 as a function of T.

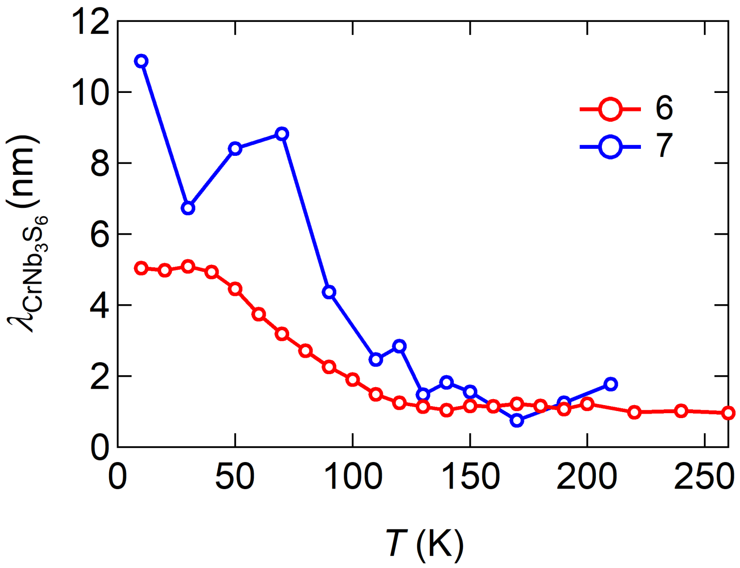

Figure 4.18: The spin diffusion length of $CrNb_3S_6$ obtained with Devices 6 and 7 as a function of T.

In summary we can conclude that spin transport phenomena observed in this thesis are very reproducible and thus peculiar to a chiral helimagnet $CrNb_3S_6$.

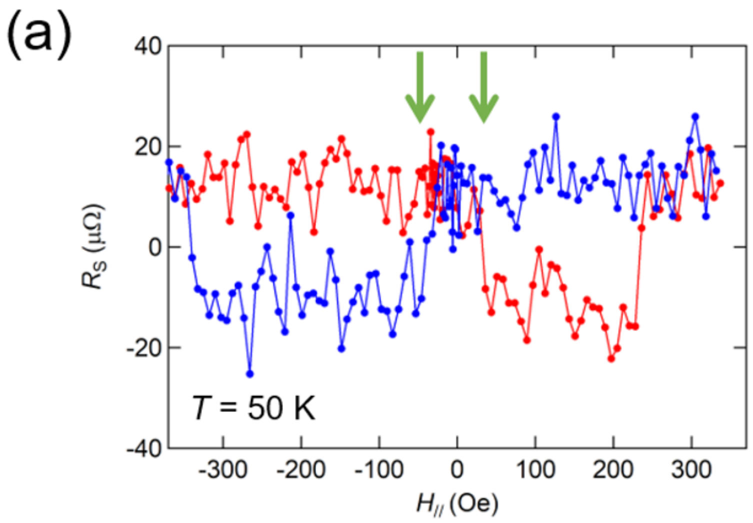

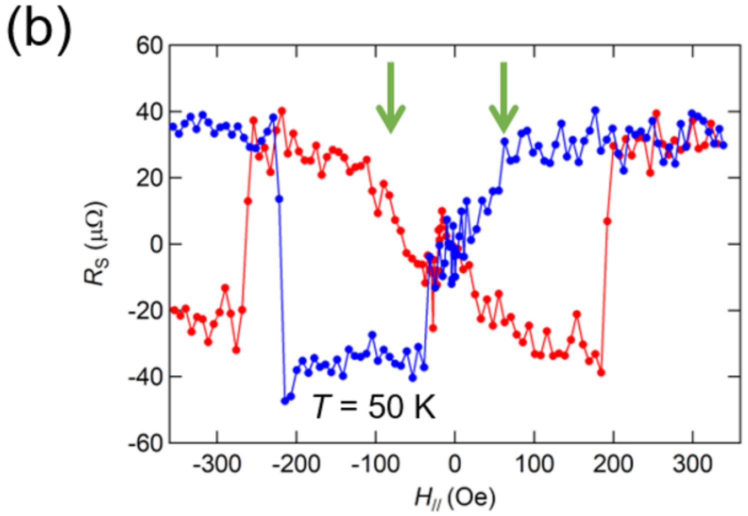

Figure 4.19: R_S at $T = 50$ K using (a) Device 3 with $t_\mathrm{M} = 47$ nm ($< L(0)$) and (b) Device 5 with $t_\mathrm{M} = 73$ nm ($> L(0)$).

Chapter 5

Conclusions and perspectives

In this thesis, we have studied spin transport properties of chiral soliton lattice (CSL). In order to reveal the magnetic dynamics of the CSL, we have performed spin transport measurements in a chiral helimagnet $\mathrm{CrNb_3S_6}$. The following is the summary of the results obtained from the present work.

Firstly, we established the fabrication process of $\mathrm{CrNb_3S_6}$ thin films. This method enables us to include a $\mathrm{CrNb_3S_6}$ thin film into spin transport devices. Thus, $\mathrm{CrNb_3S_6}$ is required to be fabricated into sub-micrometer size. This procedure can also be applied to other layered materials with relatively strong van der Waals interactions. Actually, it has already been applied to a layered triangular antiferromagnet $\mathrm{Ag_2CrO_2}$ where the interlayer interaction would be stronger than $\mathrm{CrNb_3S_6}$ [81, 82]. The establishment of the procedure to obtain atomically-thin single crystals for various materials can contribute to further development of nanoscale physics.

Secondly, we performed three different spin transport measurements in $\mathrm{CrNb_3S_6}$ thin films. For these measurements, we used two types of the $\mathrm{CrNb_3S_6}$ thin films, depending on the relation between the thickness (t_M) and one spiral pitch $L(0)$ under zero magnetic field: i.e., $t_\mathrm{M} < L(0)$ and $t_\mathrm{M} > L(0)$. We first measured the inverse spin Hall effects (ISHEs) for the two types of the $\mathrm{CrNb_3S_6}$ thin films. At room temperature, clear negative ISHE resistances were observed and the estimated spin Hall angle was about -1% for both devices. This value is consistent with that of pure Nb. The result indicates that the ISHE in $\mathrm{CrNb_3S_6}$ at room temperature is generated due to the spin-orbit interaction of Nb. With decreasing temperature, however, the ISHE resistance increases in the positive direction and takes an extremal value at the magnetic phase transition temperature $T_\mathrm{C} = 130$ K for both devices. Especially, for $t_\mathrm{M} > L(0)$, the ISHE changes the sign at a certain temperature. At T_C, the ISHE becomes as large as that at room temperature. As we decrease the temperature further, the ISHE starts to decrease, resulting in a cusp structure with respect to T_C. These results demonstrate that the ISHE not only convert the pure spin current into the charge current but also detect spin fluctuations near the magnetic transitions, as in the case of the ISHEs in weak ferromagnets and spin glasses, although detailed theoretical studies are highly desirable to unveil the relation between the ISHE and magnetic fluctuations.

Thirdly, nonlocal spin valve (NLSV) measurements were conducted using the spin transport devices with and without the $\mathrm{CrNb_3S_6}$ thin film, in order to evaluate the spin diffusion length $\lambda_{\mathrm{CrNb_3S_6}}$, which has been never discussed quantitatively so far. From the ratio of NLSV signals with and without $\mathrm{CrNb_3S_6}$, the spin diffusion length $\lambda_{\mathrm{CrNb_3S_6}}$ can be obtained. The spin diffusion length of $\mathrm{CrNb_3S_6}$ is about 5 nm at low temperature, which is consistent with that of pure Nb. On the other hand, it suddenly decreases above $T = 50$ K and is saturated at 1 nm above T_C. $\lambda_{\mathrm{CrNb_3S_6}}(T)$ is almost inversely proportional to the resistivity $\rho(T)$. This fact indicates that the Elliott-Yafet mechanism is dominant in this material.

Finally, we performed NLSV measurements where the $\mathrm{CrNb_3S_6}$ thin film was used as a ferromagnetic detector. When t_M is smaller than $L(0)$, a sudden jump in NLSV resistance appears at around ±50 Oe. This originates from the magnetization switching of $\mathrm{CrNb_3S_6}$. The result also shows that the CSL in the $\mathrm{CrNb_3S_6}$ thin film has a fixed end at the surface. For $t_\mathrm{M} > L(0)$, on the other hand, the magnetization of $\mathrm{CrNb_3S_6}$ is twisted at the surface under zero magnetic field. These results suggest that the surface magnetization of $\mathrm{CrNb_3S_6}$ strongly depends on the length of the magnetic helix.

To conclude, we have obtained spin transport properties peculiar to the chiral heimagnet $\mathrm{CrNb_3S_6}$, such as the cusp structure in the temperature dependence of the spin Hall angle and the unique nonlocal spin valve signal depending on the number of helical pitch included in the CSL. These results should give new insights not only to the studies of CSL but also into the spintronics.

As for the perspectives, in order to deeply understand the experimentally observed ISHE and NLSV signals in $\mathrm{CrNb_3S_6}$ thin films, theoretical studies on spin transport phenomena in chiral magnets are highly desirable. Especially, the experimental results strongly depends on the number of spiral structure in the $\mathrm{CrNb_3S_6}$ film. In this sense, we still need to perform the spin transport measurements using thicker $\mathrm{CrNb_3S_6}$ films that include more than two helical pitches. In order to achieve these measurements, however, there are some issues that we must overcome. Certainly, we can easily find $\mathrm{CrNb_3S_6}$ films thicker than 100 nm (more than two helical pitches), but those are too wide to be included into spin transport devices (the width should be less than 500 nm). Thus, it is necessary to optimize the exfoliation procedure to obtain thicker and narrower films.

Another direction is the application of unique spin dynamics in $CrNb_3S_6$. As mentioned above, the surface magnetization of $CrNb_3S_6$ thin film can be switched at as low as 50 Oe. This result indicates that the surface magnetization of $CrNb_3S_6$ can be easily controlled by pure spin current. For the first step of the application with $CrNb_3S_6$ thin film, spin torque-induced magnetization switching [83–86] is favorable. This can be achieved by sending a high pure-spin current density to the $CrNb_3S_6$ thin film and by detecting the NLSV signal without the external magnetic field. We have already tried this direction, but the electric current density was high enough to break the ferromagnetic injection wire by Joule heating. To avoid this problem, the device structure has to be optimized (for example, to make the wire wider), and also to use a pulse current with a duration time of a few nanoseconds.

Bibliography

[1] J. Sinova, S. O. Valenzuela, J. Wunderlich, C. H. Back, and T. Jungwirth. Spin Hall effects. *Reviews of Modern Physics*, 87:1213–1260, 2015.

[2] M. I. D'Yakonov and V. I. Perel'. Possibility of Orienting Electron Spins with Current. *Soviet Journal of Experimental and Theoretical Physics Letters*, 13:467, 1971.

[3] J. E. Hirsch. Spin Hall Effect. *Physical Review Letters*, 83:1834, 1999.

[4] Y. K. Kato, R. C. Myers, A. C. Gossard, and D. D. Awschalom. Observation of the Spin Hall Effect in Semiconductors. *Science*, 306(5703):1910–1913, 2004.

[5] D. H. Wei, Y. Niimi, B. Gu, T. Ziman, S. Maekawa, and Y. Otani. The spin Hall effect as a probe of nonlinear spin fluctuations. *Nature Communications*, 3(1):1058, 2012.

[6] P. K. Muduli, T. Higo, T. Nishikawa, D. Qu, H. Isshiki, K. Kondou, D. Nishio-Hamane, S. Nakatsuji, and Y. Otani. Evaluation of spin diffusion length and spin Hall angle of the antiferromagnetic Weyl semimetal m$n_3$sn. *Physical Review B*, 99:184425, 2019.

[7] Y. Niimi, M. Kimata, Y. Omori, B. Gu, T. Ziman, S. Maekawa, A. Fert, and Y. Otani. Strong Suppression of the Spin Hall Effect in the Spin Glass State. *Physical Review Letters*, 115:196602, 2015.

[8] H. Taniguchi, M. Watanabe, T. Ibe, M. Tokuda, T. Arakawa, T. Taniguchi, B. Gu, T. Ziman, S. Maekawa, K. Kobayashi, and Y. Niimi. Spin treacle in a frustrated magnet observed with spin current. *Physical Review B*, 102:094405, 2020.

[9] I.E. Dzialoshinskii. Thermodynamic theory of "weak" ferromagnetism in antiferromagnetic substances. *Soviet physics JETP*, 5(6):1259–1272, 1957.

[10] I. E. Dzyaloshinsky. A thermodynamic theory of “weak” ferromagnetism of antiferromagnetics. *Journal of Physics and Chemistry of Solids*, 4(4):241–255, 1958.

[11] T. Miyadai, K. Kikuchi, H. Kondo, S. Sakka, M. Arai, and Y. Ishikawa. Magnetic Properties of $\mathrm{Cr_{1/3}NbS_2}$. *Journal of the Physical Society of Japan*, 52(4):1394–1401, 1983.

[12] I. Pilz, O. Glatter, and O. Kratky. [11] small-angle x-ray scattering. In *Enzyme Structure Part H*, volume 61 of *Methods in Enzymology*, pages 148–249. Academic Press, 1979.

[13] Y. Togawa, T. Koyama, K. Takayanagi, S. Mori, Y. Kousaka, J. Akimitsu, S. Nishihara, K. Inoue, A. S. Ovchinnikov, and J. Kishine. Chiral Magnetic Soliton Lattice on a Chiral Helimagnet. *Physical Review Letters*, 108:107202, 2012.

[14] A. Yoshimori. A New Type of Antiferromagnetic Structure in the Rutile Type Crystal. *Journal of the Physical Society of Japan*, 14(6):807–821, 1959.

[15] T. A. Kaplan. Classical Spin-Configuration Stability in the Presence of Competing Exchange Forces. *Physical Review*, 116:888–889, 1959.

[16] J. Villain. La structure des substances magnetiques. *Journal of Physics and Chemistry of Solids*, 11(3):303–309, 1959.

[17] I. E. Dzyaloshinskii. Theory of helicoidal structures in antiferromagnets. I. Nonmetals. *Soviet physics JETP*, 19(4):960–971, 1964.

[18] T. H. R. Skyrme. A unified field theory of mesons and baryons. *Nuclear Physics*, 31:556–569, 1962.

[19] S. Mühlbauer, B. Binz, F. Jonietz, C. Pfleiderer, A. Rosch, A. Neubauer, R. Georgii, and P. Böni. Skyrmion Lattice in a Chiral Magnet. *Science*, 323(5916):915–919, 2009.

[20] Y. Togawa, Y. Kousaka, K. Inoue, and J. Kishinr. Symmetry, Structure, and Dynamics of Monoaxial Chiral Magnets. *Journal of the Physical Society of Japan*, 85(11):112001, 2016.

[21] 岸根 順一郎. Through the Looking-Glass：物質科学と Chirality. **日本物理学会誌**, 72(5):294–295, 2016.

[22] L. Kelvin. Baltimore Lectures on Molecular Dynamics and the Wave Theory of Light. *C. J. Clay and Sons, London*, 1904.

[23] L. D. Barron. True and false chirality and parity violation. *Chemical Physics Letters*, 123(5):423–427, 1986.

[24] T. Moriya. Anisotropic Superexchange Interaction and Weak Ferromagnetism. *Physical Review*, 120:91–98, 1960.

[25] T. Moriya. New Mechanism of Anisotropic Superexchange Interaction. *Physical Review Letters*, 4:228–230, 1960.

[26] J. Kishine, K. Inoue, and Y. Yoshida. Synthesis, Structure and Magnetic Properties of Chiral Molecule-Based Magnets. *Progress of Theoretical Physics Supplement*, 159:82–95, 2005.

[27] J. Kishine, I. G. Bostrem, A. S. Ovchinnikov, and Vl. E. Sinitsyn. Topological magnetization jumps in a confined chiral soliton lattice. *Physical Review B*, 89:014419, 2014.

[28] Y. Togawa, T. Koyama, Y. Nishimori, Y. Matsumoto, S. McVitie, D. McGrouther, R. L. Stamps, Y. Kousaka, J. Akimitsu, S. Nishihara, K. Inoue, I. G. Bostrem, Vl. E. Sinitsyn, A. S. Ovchinnikov, and J. Kishine. Magnetic soliton confinement and discretization effects arising from macroscopic coherence in a chiral spin soliton lattice. *Physical Review B*, 92:220412, 2015.

[29] K. Momma and F. Izumi. *VESTA3* for three-dimensional visualization of crystal, volumetric and morphology data. *Journal of Applied Crystallography*, 44(6):1272–1276, 2011.

[30] L. M. Volkova and D. V. Marinin. Role of structural factors in formation of chiral magnetic soliton lattice in $\mathrm{Cr_{1/3}NbS_2}$. *Journal of Applied Physics*, 116(13):133901, 2014.

[31] L. Wang, N. Chepiga, D. K. Ki, L. Li, F. Li, W. Zhu, Y. Kato, O. S. Ovchinnikova, F. Mila, I. Martin, D. Mandrus, and A. F. Morpurgo. Controlling the Topological Sector of Magnetic Solitons in Exfoliated $\mathrm{Cr_{1/3}NbS_2}$ Crystals. *Physical Review Letters*, 118:257203, 2017.

[32] M. N. Baibich, J. M. Broto, A. Fert, F. Nguyen Van Dau, F. Petroff, P. Etienne, G. Creuzet, A. Friederich, and J. Chazelas. Giant Magnetoresistance

of (001)Fe/(001)Cr Magnetic Superlattices. *Physical Review Letters*, 61:2472–2475, 1988.

[33] G. Binasch, P. Grünberg, F. Saurenbach, and W. Zinn. Enhanced magnetoresistance in layered magnetic structures with antiferromagnetic interlayer exchange. *Physical Review B*, 39:4828–4830, 1989.

[34] M. Johnson and R. H. Silsbee. Interfacial charge-spin coupling: Injection and detection of spin magnetization in metals. *Physical Review Letters*, 55:1790–1793, 1985.

[35] F. J. Jedema, A. T. Filip, and B. J. van Wees. Electrical spin injection and accumulation at room temperature in an all-metal mesoscopic spin valve. *Nature*, 410(6826):345–348, 2001.

[36] T. Kimura, J. Hamrle, and Y. Otani. Estimation of spin-diffusion length from the magnitude of spin-current absorption: Multiterminal ferromagnetic/nonferromagnetic hybrid structures. *Physical Review B*, 72:014461, 2005.

[37] T. Kimura, Y. Otani, T. Sato, S. Takahashi, and S. Maekawa. Room-Temperature Reversible Spin Hall Effect. *Physical Review Letters*, 98:156601, 2007.

[38] L. Vila, T. Kimura, and Y. Otani. Evolution of the Spin Hall Effect in Pt Nanowires: Size and temperature Effects. *Physical Review Letters*, 99:226604, 2007.

[39] Y. Niimi and Y. Otani. Reciprocal spin Hall effects in conductors with strong spin–orbit coupling: a review. *Reports on Progress in Physics*, 78(12):124501, 2015.

[40] E. Saitoh, M. Ueda, H. Miyajima, and G. Tatara. Conversion of spin current into charge current at room temperature: Inverse spin-Hall effect. *Applied Physics Letters*, 88(18):182509, 2006.

[41] S. O. Valenzuela and M. Tinkham. Direct electronic measurement of the spin Hall effect. *Nature*, 442(7099):176–179, 2006.

[42] S. Takahashi and S. Maekawa. Spin injection and detection in magnetic nanostructures. *Physical Review B*, 67:052409, 2003.

[43] S. Takahashi and S. Maekawa. Spin current, spin accumulation and spin Hall effect. *Science and Technology of Advanced Materials*, 9(1):014105, 2008. PMID: 27877931.

[44] Y. Niimi, M. Morota, D. H. Wei, C. Deranlot, M. Basletic, A. Hamzic, A. Fert, and Y. Otani. Extrinsic Spin Hall Effect Induced by Iridium Impurities in Copper. *Physical Review Letters*, 106:126601, 2011.

[45] J. Kondo. Anomalous Hall Effect and Magnetoresistance of Ferromagnetic Metals. *Progress of Theoretical Physics*, 27(4):772–792, 1962.

[46] B. Gu, T. Ziman, and S. Maekawa. Theory of the spin Hall effect, and its inverse, in a ferromagnetic metal near the Curie temperature. *Physical Review B*, 86:241303, 2012.

[47] B. F. Miao, S. Y. Huang, D. Qu, and C. L. Chien. Inverse Spin Hall Effect in a Ferromagnetic Metal. *Physical Review Letters*, 111:066602, 2013.

[48] K. Uchida, S. Takahashi, K. Harii, J. Ieda, W. Koshibae, K. Ando, S. Maekawa, and E. Saitoh. Observation of the spin Seebeck effect. *Nature*, 455(7214):778–781, 2008.

[49] S. M. Wu, J. Hoffman, J. E. Pearson, and A. Bhattacharya. Unambiguous separation of the inverse spin Hall and anomalous Nernst effects within a ferromagnetic metal using the spin Seebeck effect. *Applied Physics Letters*, 105(9):092409, 2014.

[50] D. Tian, Y. Li, D. Qu, S. Y. Huang, X. Jin, and C. L. Chien. Manipulation of pure spin current in ferromagnetic metals independent of magnetization. *Physical Review B*, 94:020403, 2016.

[51] J. D. Gibbons, D. MacNeill, R. A. Buhrman, and D. C. Ralph. Reorientable Spin Direction for Spin Current Produced by the Anomalous Hall Effect. *Physical Review Applied*, 9:064033, 2018.

[52] M. Kimata, H. Chen, K. Kondou, S. Sugimoto, P. K. Muduli, M. Ikhlas, Y. Omori, T. Tomita, A. H. MacDonald, S. Nakatsuji, and Y. Otani. Magnetic and magnetic inverse spin Hall effects in a non-collinear antiferromagnet. *Nature*, 565(7741):627–630, 2019.

[53] V. Cannella and J. A. Mydosh. Magnetic Ordering in Gold-Iron Alloys. *Physical Review B*, 6:4220–4237, 1972.

[54] T. Taniguchi, H. Matsuyama, S. Chikazawa, and Y. Miyako. Linear and Non-Linear Susceptibilities in Canonical Spin Glass AuFe (1.5 at.%Fe). *Journal of the Physical Society of Japan*, 52(12):4323–4330, 1983.

[55] G. G. Kenning, J. M. Slaughter, and J. A. Cowen. Finite-Size Effects in a CuMn Spin-Glass. *Physical Review Letters*, 59:2596–2599, 1987.

[56] G. G. Kenning, J. Bass, W. P. Pratt, D. Leslie-Pelecky, L. Hoines, W. Leach, M. L. Wilson, R. Stubi, and J. A. Cowen. Finite-size effects in Cu-Mn spin glasses. *Physical Review B*, 42:2393–2415, 1990.

[57] R. J. Elliott. Theory of the Effect of Spin-Orbit Coupling on Magnetic Resonance in Some Semiconductors. *Physical Review*, 96:266–279, 1954.

[58] I. Žutić, J. Fabian, and S. Das Sarma. Spintronics: Fundamentals and applications. *Reviews of Modern Physics*, 76:323–410, 2004.

[59] J. Fabian and S. D. Sarma. Spin relaxation of conduction electrons. *Journal of Vacuum Science & Technology B: Microelectronics and Nanometer Structures Processing, Measurement, and Phenomena*, 17(4):1708–1715, 1999.

[60] K. S. Novoselov, A. K. Geim, S. V. Morozov, D. Jiang, Y. Zhang, S. V. Dubonos, I. V. Grigorieva, and A. A. Firsov. Electric Field Effect in Atomically Thin Carbon Films. *Science*, 306(5696):666, 2004.

[61] K. S. Novoselov, V. I. Fal'ko, L. Colombo, P. R. Gellert, M. G. Schwab, and K. Kim. A roadmap for graphene. *Nature*, 490(7419):192–200, 2012.

[62] A. K. Geim and I. V. Grigorieva. Van der Waals heterostructures. *Nature*, 499(7459):419–425, 2013.

[63] J. T. Ye, Y. J. Zhang, R. Akashi, M. S. Bahramy, and Y. Arita, R. and Iwasa. Superconducting Dome in a Gate-Tuned Band Insulator. *Science*, 338(6111):1193, 2012.

[64] B. Radisavljevic, A. Radenovic, J. Brivio, V. Giacometti, and A. Kis. Single-layer MoS_2 transistors. *Nature Nanotechnology*, 6(3):147–150, 2011.

[65] M. Yoshida, J. Ye, T. Nishizaki, N. Kobayashi, and Y. Iwasa. Electrostatic and electrochemical tuning of superconductivity in two-dimensional $NbSe_2$ crystals. *Applied Physics Letters*, 108(20):202602, 2016.

[66] X. Xi, L. Zhao, Z. Wang, H. Berger, L. Forró, J. Shan, and K. F. Mak. Strongly enhanced charge-density-wave order in monolayer $NbSe_2$. *Nature Nanotechnology*, 10(9):765–769, 2015.

[67] X. Xi, Z. Wang, W. Zhao, J. Park, K. T. Law, H. Berger, L. Forró, J. Shan, and K. F. Mak. Ising pairing in superconducting $NbSe_2$ atomic layers. *Nature Physics*, 12(2):139–143, 2016.

[68] M. Yokoi, S. Fujiwara, T. Kawamura, T. Arakawa, K. Aoyama, H. Fukuyama, K. Kobayashi, and Y. Niimi. Negative resistance state in superconducting $NbSe_2$ induced by surface acoustic waves. *Science Advances*, 6(34):eaba1377, 2020.

[69] M. Yankowitz, J. Xue, D. Cormode, J. D. Sanchez-Yamagishi, K. Watanabe, T. Taniguchi, P. Jarillo-Herrero, P. Jacquod, and B. J. LeRoy. Emergence of superlattice Dirac points in graphene on hexagonal boron nitride. *Nature Physics*, 8(5):382–386, 2012.

[70] L. A. Ponomarenko, R. V. Gorbachev, G. L. Yu, D. C. Elias, R. Jalil, A. A. Patel, A. Mishchenko, A. S. Mayorov, C. R. Woods, J. R. Wallbank, M. Mucha-Kruczynski, B. A. Piot, M. Potemski, I. V. Grigorieva, K. S. Novoselov, F. Guinea, V. I. Fal'ko, and A. K. Geim. Cloning of Dirac fermions in graphene superlattices. *Nature*, 497(7451):594–597, 2013.

[71] C. R. Dean, L. Wang, P. Maher, C. Forsythe, F. Ghahari, Y. Gao, J. Katoch, M. Ishigami, P. Moon, M. Koshino, T. Taniguchi, K. Watanabe, K. L. Shepard, J. Hone, and P. Kim. Hofstadter's butterfly and the fractal quantum Hall effect in moiré superlattices. *Nature*, 497(7451):598–602, 2013.

[72] T. Iwasaki, K. Endo, E. Watanabe, D. Tsuya, Y. Morita, S. Nakaharai, Y. Noguchi, Y. Wakayama, K. Watanabe, T. Taniguchi, and S. Moriyama. Bubble-Free Transfer Technique for High-Quality Graphene/Hexagonal Boron Nitride van der Waals Heterostructures. *ACS Applied Materials & Interfaces*, 12(7):8533–8538, 2020. PMID: 32027115.

[73] K. S. Novoselov, D. Jiang, F. Schedin, T. J. Booth, V. V. Khotkevich, S. V. Morozov, and A. K. Geim. Two-dimensional atomic crystals. *Proceedings of the National Academy of Sciences*, 102(30):10451–10453, 2005.

[74] X. Wang, L. X. You, D. K. Liu, C. T. Lin, X. M. Xie, and M. H. Jiang. Thin-film-like BSCCO single crystals made by mechanical exfoliation. *Physica C: Superconductivity*, 474:13–17, 2012.

[75] S Suzuki, H Taniguchi, T Kawakami, M Cosset-Cheneau, T. Arakawa, S Miyasaka, S Tajima, Y. Niimi, and K Kobayashi. Electrical contacts to thin layers of $Bi_2Sr_2CaCu_2O_{8+\delta}$. *Applied Physics Express*, 11(5):053201, 2018.

[76] S. Y. F. Zhao, N. Poccia, M. G. Panetta, C. Yu, J. W. Johnson, H. Yoo, R. Zhong, G. D. Gu, K. Watanabe, T. Taniguchi, S. V. Postolova, V. M. Vinokur, and P. Kim. Sign-Reversing Hall Effect in Atomically Thin High-Temperature $Bi_{2.1}Sr_{1.9}CaCu_{2.0}O_{8+\delta}$ Superconductors. *Physical Review Letters*, 122:247001, 2019.

[77] C. Gong, L. Li, Z. Li, H. Ji, A. Stern, Y. Xia, T. Cao, W. Bao, C. Wang, Y. Wang, Z. Q. Qiu, R. J. Cava, Steven G. Louie, J. Xia, and X. Zhang. Discovery of intrinsic ferromagnetism in two-dimensional van der Waals crystals. *Nature*, 546(7657):265–269, 2017.

[78] B. Huang, G. Clark, E. Navarro-Moratalla, D. R. Klein, R. Cheng, K. L. Seyler, D. Zhong, E. Schmidgall, M. A. McGuire, D. H. Cobden, W. Yao, D. Xiao, P. Jarillo-Herrero, and X. Xu. Layer-dependent ferromagnetism in a van der Waals crystal down to the monolayer limit. *Nature*, 546(7657):270–273, 2017.

[79] Y. Deng, Y. Yu, Y. Song, J. Zhang, N. Z. Wang, Z. Sun, Y. Yi, Y. Z. Wu, S. Wu, J. Zhu, J. Wang, X. H. Chen, and Y. Zhang. Gate-tunable room-temperature ferromagnetism in two-dimensional Fe_3GeTe_2. *Nature*, 563(7729):94–99, 2018.

[80] T. Ohta, K Sakai, H. Taniguchi, B. Driesen, Y. Okada, K. Kobayashi, and Y. Niimi. Enhancement of coercive field in atomically-thin quenched Fe_5GeTe_2. *Applied Physics Express*, 13(4):043005, 2020.

[81] H. Taniguchi, S. Suzuki, T. Arakawa, H. Yoshida, Y. Niimi, and K. Kobayashi. Fabrication of thin films of two-dimensional triangular antiferromagnet Ag_2CrO_2 and their transport properties. *AIP Advances*, 8(2):025010, 2018.

[82] H. Taniguchi, M. Watanabe, M. Tokuda, S. Suzuki, E. Imada, T. Ibe, T. Arakawa, H. Yoshida, H. Ishizuka, K. Kobayashi, and Y. Niimi. Butterfly-shaped magnetoresistance in triangular-lattice antiferromagnet Ag_2CrO_2. *Scientific Reports*, 10(1):2525, 2020.

[83] L. Berger. Emission of spin waves by a magnetic multilayer traversed by a current. *Physical Review B*, 54:9353–9358, 1996.

[84] J. C. Slonczewski. Current-driven excitation of magnetic multilayers. *Journal of Magnetism and Magnetic Materials*, 159(1):L1–L7, 1996.

[85] T. Kimura, Y. Otani, and J. Hamrle. Switching Magnetization of a Nanoscale Ferromagnetic Particle Using Nonlocal Spin Injection. *Physical Review Letters*, 96:037201, 2006.

[86] R. Fujimura, R. Yoshimi, M. Mogi, A. Tsukazaki, M. Kawamura, K.S. Takahashi, M. Kawasaki, and Y. Tokura. Current-induced magnetization switching at charge-transferred interface between topological insulator $(Bi,Sb)_2Te_3$ and van der Waals ferromagnet Fe_3GeTe_2. *Applied Physics Letters*, 119(3):032402, 2021.

Acknowledgements

本研究を遂行するにあたり、大変多くの方々に支えて頂きました。ここに御礼申し上げます。

指導教官である新見康洋教授には、博士前期課程から研究テーマを与えて頂き、学会発表、論文作成、進路選択など、あらゆる面で助けていただきました。私の研究が思うように進まない中でも、辛抱強くご指導いただいて、感謝の念に堪えません。上手くいかないことの方が多い研究ですが、新見教授の前向きなご助言のおかげで続けることができたと感じています。また、研究においてコミュニケーションを重視する姿勢は、今後の私の人生でも参考になる点が多いと思います。

東京大学の小林研介教授には、博士前期課程から後期課程2年まで、大阪大学の小林研究室でお世話になりました。研究に関して的確な指摘を多数頂き、視野が広がりました。また、進路についてアドバイスをいただき、学振の申請や就活で大変お世話になりました。人に伝えるための論理的の文章を書く能力を向上させることができたと感じています。

大阪府立大学の戸川欣彦教授には、$CrNb_3S_6$ の結晶を頂いた他、パルスジェネレータをお貸しくださいました。いつも素早く対応してくださり、滞りなく実験を進めることができました。また、議論を通して $CrNb_3S_6$ やらせん磁性についてご教授していただき、大変勉強になりました。戸川教授のご助力がなければ、私の研究は成り立ちませんでした。

大阪大学基礎工学研究科の寻田博一教授、浜屋宏平教授には電子線描画装置の使用、および維持管理においてお世話になりました。研究で欠かすことのできない工程をスムーズにこなすことができました。

産総研の荒川智紀博士には、旧小林研究室の助教時代に、主に実験技術でご指導を賜りました。電気測定に関する豊富な知識には、何度も助けられました。また、阪大を離れられてからも、新見教授を通じて電気測定に関する助言を頂き、大変助かりました。

佐々木潤子さん、高尾明子さんには事務の仕事でお世話になりました。快適に研究生活を送ることができました。

新見研究室（旧小林研究室）の皆様にも、様々なご支援を賜りました。

共同研究者の佐々木壱晟君には、らせん磁性の先輩として、実験技術などで多くのことを学ばせて頂きました。なかなか力になれず、申し訳なさが募っていましたが、何とか$CrNb_3S_6$のスピン拡散長を出せたときはほっとしました。

谷口裕紀さんには、スピントロニクス班の先輩として試料作製や測定の技術を伝授して下さいました。また、卒業されてからも度々スピンバルブの作製方法や就活などで助言を頂きました。お忙しいのにいつもすぐに返信をくださり有難さと申し訳なさでいっぱいでした。

横井雅彦さんには、原子層物質の先輩として多くの助言を頂き、その圧倒的な知識や思慮深さに触れ、研究についての視野を広げることができました。

岩切秀一さん、Lee Sanghyun さんとは、直接研究で関わることは少なかったですが、研究相談などで多くの助言を頂き、研究の質を向上させることができました。

徳田将志君には、自ら進んで研究していく姿勢に感銘を受けました。好奇心を持って研究に取り組む姿は、研究室全体のモチベーションの向上に寄与していたのではないかと感じています。

太田智陽君は、ストイックに研究に取り組む姿勢や、コミュニケーション能力など、学ぶべき点が多いと感じています。私は結局スタンプ装置を活かすことができなかったので、中村君とともに接合系の研究を開拓していってくれていて、大変有難いです。

渡邉杜君には、英語関連でお世話になることが多かったです。この博士論文においても、英文の添削をしていただきました。生きた英語に触れることができたことは、今後の人生で大いに役立つことと思います。

川原遼馬君には、$CrNb_3S_6$の研究をスタートしていただきました。川原君が基礎を築いてくれたからこそ、研究を進展させることができたと思います。

藤原浩司君には、主にスピン注入磁化反転の測定でお世話になりました。高周波を使った測定技術を伝授していただきました。

浅野拓也君、井邊昂志君、坂井康介君、花田尚輝君、藤原聖士君、中尾舞さん、大星和毅君、黒川開斗君勝村亮太君、中村暸弥君、浅間遼太郎君、前田将輝君には、先輩として力になれたことは少なかったと思いますが、熱心に研究をする姿をみて、大いに励みになりました。

最後に、長期間にわたった私の学生生活を支えて下さった家族に感謝いたします。